ANNUAL REPORT ON

APPLICATION OF MODEL-BASED SIGNAL PROCESSING AND GENETIC ALGORITHMS FOR SHIPBOARD ANTENNA DESIGN, PLACEMENT AND OPTIMIZATION

Office of Naval Research
Research Grant N00014-01-1-0224

For the period December 1, 2000 through November 30, 2001

Submitted by

Professor Hao Ling

Department of Electrical and Computer Engineering
The University of Texas at Austin
Austin, TX 78712-1084

January 31, 2002

Reproduced From
Best Available Copy

DISTRIBUTION STATEMENT A
Approved for Public Release
Distribution Unlimited

20020308 083

REPORT DOCUMENTATION PAGE

Form Approved
OMB No. 0704-0188

Public reporting burden for this collection of information is estimated to average 1 hour per response, including the time for reviewing instructions, searching existing data sources, gathering and maintaining the data needed, and completing and reviewing the collection of information. Send comments regarding this burden estimate or any other aspect of this collection of information, including suggestions for reducing this burden to Washington Headquarters Services, Directorate for Information Operations and Reports, 1215 Jefferson Davis Highway, Suite 1204, Arlington, VA 22202-4302, and to the Office of Management and Budget, Paperwork Reduction Project (0704-0188), Washington, DC 20503.

1. AGENCY USE ONLY *(Leave blank)*	2. REPORT DATE	3. REPORT TYPE AND DATES COVERED
	Jan. 31, 2002	Annual Report 1 Dec. 00-30 Nov. 01

4. TITLE AND SUBTITLE
Annual Report on Application of Model-Based Signal Processing and Genetic Algorithms for Shipboard Antenna Design

5. FUNDING NUMBERS
Research Grant
ONR
N00014-01-0-0224

6. AUTHOR(S)
Hao Ling

7. PERFORMING ORGANIZATION NAMES(S) AND ADDRESS(ES)
The University of Texas at Austin
Department of Electrical and Computer Engineering
Austin, TX 78712-1084

8. PERFORMING ORGANIZATION REPORT NUMBER
No. 4

9. SPONSORING / MONITORING AGENCY NAMES(S) AND ADDRESS(ES)
Office of Naval Research
Ballston Centre Tower One
800 North Quincy Street
Arlington, VA 22217-5660

Program Officer
Wen Masters
ONR 311

10. SPONSORING / MONITORING AGENCY REPORT NUMBER

11. SUPPLEMENTARY NOTES

a. DISTRIBUTION / AVAILABILITY STATEMENT
Approved for Public Release
Distribution Unlimited

12. DISTRIBUTION CODE

13. ABSTRACT *(Maximum 200 words)*

This report summarizes the scientific progress on the research grant "Application of Model-Based Signal Processing and Genetic Algorithms for Shipboard Antenna Design, Placement and Optimization" during the period 1 December 2000 - 30 November 2001. Progress on using genetic algorithms in conjunction with computational electromagnetics for microstrip antenna design, array beamforming, microwave absorber shaping and electrically small wire antenna design is described.

14. SUBJECT TERMS
Genetic algorithms, computational electromagnetics

15. NUMBER OF PAGES
159

16. PRICE CODE

17. SECURITY CLASSIFICATION OF REPORT	18. SECURITY CLASSIFICATION OF THIS PAGE	19. SECURITY CLASSIFICATION OF ABSTRACT	20. LIMITATION OF ABSTRACT

Standard Form 298 (Rev. 2-89)
Prescribed by ANISE Sad Z39-18
298-102

ANNUAL REPORT ON

APPLICATION OF MODEL-BASED SIGNAL PROCESSING AND GENETIC ALGORITHMS FOR SHIPBOARD ANTENNA DESIGN, PLACEMENT AND OPTIMIZATION

Office of Naval Research
Research Grant N00014-01-1-0224

For the period December 1, 2000 through November 30, 2001

Submitted by

Professor Hao Ling

Department of Electrical and Computer Engineering
The University of Texas at Austin
Austin, TX 78712-1084

January 31, 2002

APPLICATION OF MODEL-BASED SIGNAL PROCESSING AND GENETIC ALGORITHMS FOR SHIPBOARD ANTENNA DESIGN, PLACEMENT AND OPTIMIZATION

Project Starting Date: Dec. 1, 2000

Reporting Period: Dec. 1, 2000 – Nov. 30, 2001

Principal Investigator: Professor Hao Ling
(512) 471-1710
ling@ece.utexas.edu

Graduate Students: Tao Su, Hosung Choo, Adrian Hutani, Aaron Kerkhoff

A. SCIENTIFIC OBJECTIVES: The objective of this research program is to explore new design methodologies and establish performance bounds in shipboard antenna problems. Our approach is to combine genetic algorithms (GA) and model-based signal processing with computational electromagnetic simulators to investigate antenna design, placement and optimization. The specific problems to be investigated include microstrip antenna design, array synthesis and placement in the presence of platform effects, electrically small wire antenna design and microwave absorber design. Our goals are to map out fundamental performance bounds in complex design problems and to devise actual design implementations that can approach these performance bounds.

B. SUMMARY OF RESULTS AND SIGNIFICANT ACCOMPLISHMENTS: During the current year, we have made significant progress on four topics: (i) shape optimization of broadband and multi-band microstrip antenna elements, (ii) antenna array beamforming and placement in the presence of platform effects, (iii) shape optimization of light-weight microwave absorbers, and (iv) design of electrically small wire antennas.

In the first topic, we have applied GA and a fast computational electromagnetic solver to design novel microstrip antenna shapes for broadband operations, multi-band operations and circular polarization. For the broadband design, we reported a four-fold improvement in bandwidth compared to a regular-shaped microstrip. For dual-band applications, we achieved arbitrary frequency spacing between the two frequency bands

ranging from 1.1 to 2. Tri-band and quad-band operations were also realized. All designs were fabricated and verified by measurements.

In the second topic, we have applied GA for array beamforming in the presence of platform and mutual coupling effects. In our optimization process, the active element patterns of the antenna elements were either computed using an electromagnetic solver or obtained through in-situ measurements. The element excitations were then optimized by GA for each prescribed beam. Both simulation results and field measurement data (using a 7-element smart antenna testbed) were collected. It was demonstrated that the GA-synthesized beams could be used to overcome the blockage effect due the mounting tower. Direction finding experiments were also carried out and showed that the GA results can be successfully used to locate emitters.

In the third topic, we have applied GA to the design of corrugated microwave absorbers. By combining GA with a full-wave computational electromagnetic solver, we obtained absorber performance that is superior to previously investigated geometrical shapes. Physical interpretation of the GA-optimize shapes was formulated to explain the behavior of the absorber as a function of polarization and incident angle. Furthermore, we investigated the optimal absorber performance as a function of absorber thickness (or weight) by means of the Pareto GA technique. The performance limit of the absorber as a function of thickness was efficiently mapped out using this approach.

In the fourth topic, we have carried out research into the design of electrically small wire antennas. The well-known theoretical limit for antenna bandwidth as a function of its electrical size was derived by L. J Chu in 1948. Our objective was to apply GA optimization to design wire antennas that can approach the Chu limit. In our initial design, we used GA together with a wire antenna code to study the performance of a single-arm wire with a number of bent segments. It was found that the achievable performance was below the Chu limit. Folded wire configurations and multiple arm designs are under investigation.

Below we shall describe the four topics in more detail.

Microstrip Antenna Design and Optimization. Due to its low profile and ease of fabrication, microstrip antenna is a very popular choice in many commercial and military

applications. However, a well-known drawback of the microstrip is that it is intrinsically a narrow-band device. We have applied GA and a fast computational electromagnetics solver to design novel microstrip antenna shapes for broadband and multi-band operations [14,22,24,26]. Research in the application of GA for antenna design has been ongoing since the early 1990s [1,2]. In contrast to a local optimization algorithm, GA allows the design space to be more fully explored (at the expense of computational cost). In our GA implementation, the geometry of the patch is discretized into a two-dimensional binary map and GA is used to search for the optimal patch shape that maximizes bandwidth. Several schemes are utilized to accelerate the convergence of the GA including 2-point crossover and geometrical filtering through the use of a median filter. Shapes in the population are ranked according to a computed cost function and a new generation of children shapes is produced through the rules of heredity and mutation. This process is repeated until a satisfactory shape is found that best meets the design criteria.

Fig. 1(a) shows the GA-designed broadband microstrip shape [14]. This optimized shape has a four-fold improvement in bandwidth when compared to a standard square microstrip antenna. This design has been verified by laboratory measurement on FR-4 substrate. Fig. 1(b) shows the excellent agreement between the simulation and measured

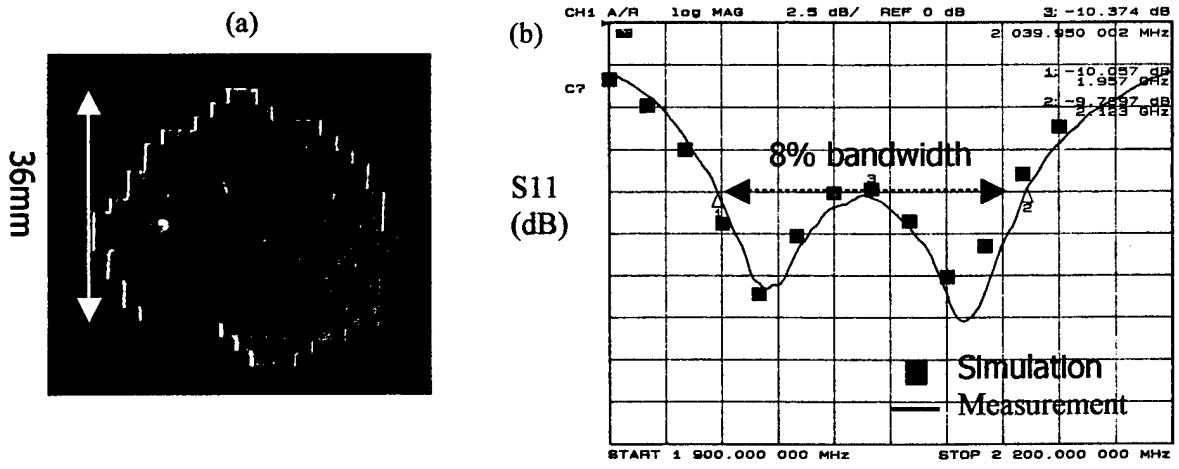

Fig. 1. A broadband microstrip antenna designed using the genetic algorithm and built on FR-4 material. The right figure shows the return loss (dB) of the antenna from simulation (□) and measurement (–). The antenna has an operating frequency of 2 GHz and an 8% bandwidth, which is 4 times broader than a conventional square microstrip.

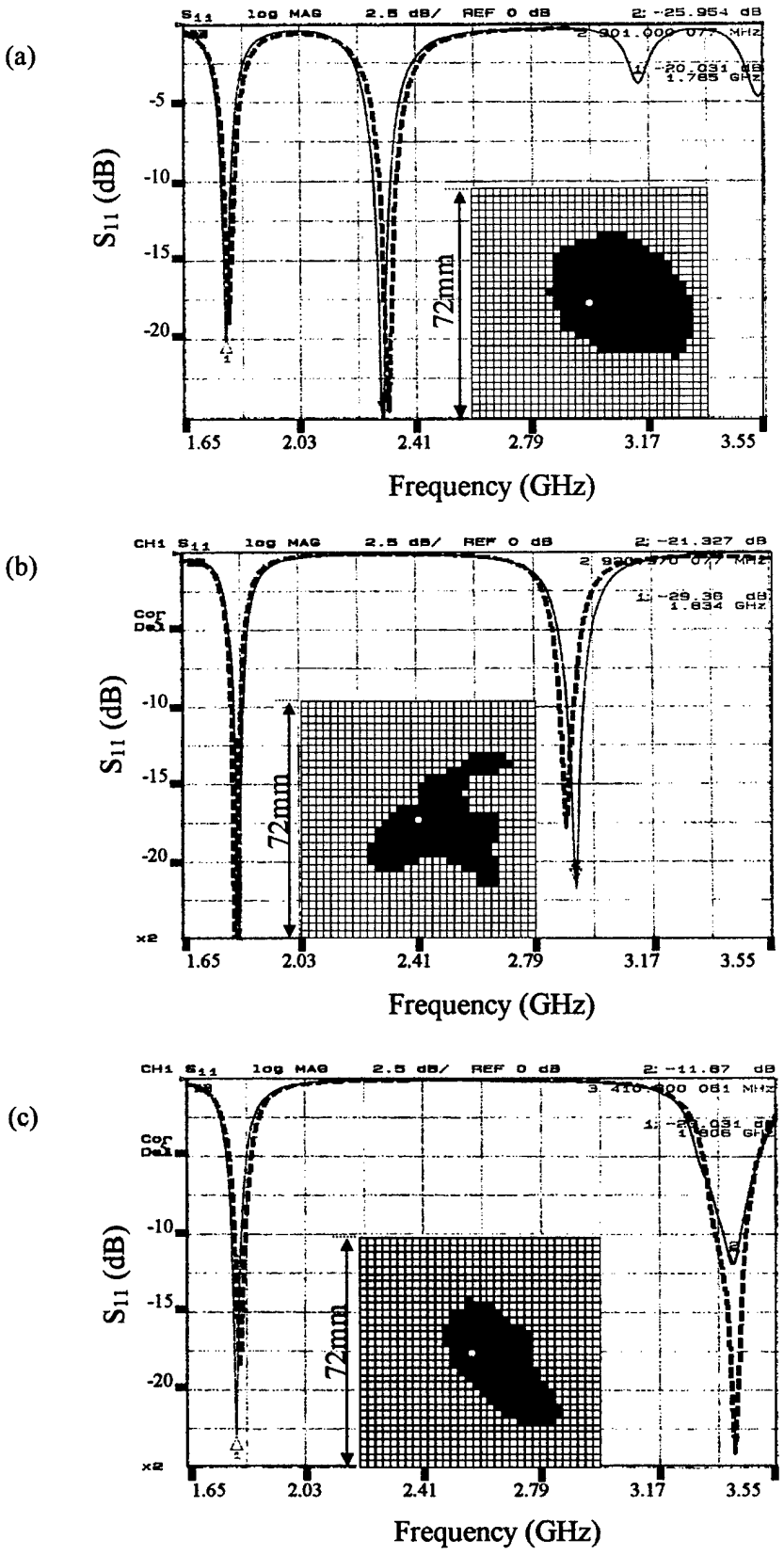

Fig. 2. Shapes of three GA-optimized dual-band microstrip antennas, and the resulting return loss from simulation (------) and measurement (——). (a) Frequency ratio of 1:1.3 (1.8GHz and 2.34GHz). (b) Frequency ratio 1:1.6 (1.8GHz and 2.9GHz). (c) Frequency ratio of 1:1.9 (1.8GHz and 3.42GHz).

results. The basic operating principle of the optimized shape has also been interpreted in terms of a combination of dual-mode operation and ragged edge shape. We have also extended this methodology to design multi-band microstrip antennas [22,26]. We have designed a collection of microstrip shapes that can achieve two frequency bands of operation with arbitrary frequency spacing between the two bands ranging from 1:1.1 to 1:2.0. Figs. 2(a) to 2(c) show three of our designed shapes with frequency ratios of 1.3, 1.6 and 1.9, respectively. Again these results have been verified by measurements and showed precise dual-band operation with good bandwidth. We have also numerically verified that these shapes could be scaled in size to any specific operating frequency of interest, or for different substrate materials. Tri-band and quad-band microstrips designed using the same GA methodology have also been demonstrated recently [24].

Array Antenna Placement and Beamforming. It is well known in antenna design that the mounting platform can have a significant impact on antenna performance. For example, in the deployment of antenna arrays it is not always possible to mount the array on top of a tower. When the array is mounted at the mid-tower level, the pattern behavior of the array could be significantly degraded due to the presence of the tower. In this work, we address how GA can be utilized to achieving array placement and beamforming to overcome platform effects. This work is leveraged upon our previous studies on array mutual coupling and platform interactions [15,18,19,25].

In our GA-based beamforming procedure, the active element patterns of the antenna elements are either computed using an electromagnetic solver or obtained through in-situ measurements. The element excitations are then optimized by the GA for each prescribed beam. For each beam pattern, a cost is assessed if the radiated field is below a desired level in the main beam or above the sidelobe level in the sidelobe range. Unlike conventional array synthesis [3] in which the transition between the main beam and sidelobe is unconstrained, this region is also constrained here due to the strong tower effect.

The algorithm has been tested using simulation data from the Numerical Electromagnetics Code (NEC) for a seven-element circular dipole array of one wavelength diameter. The array is mounted next to a metal tower, as shown in Fig. 3(a).

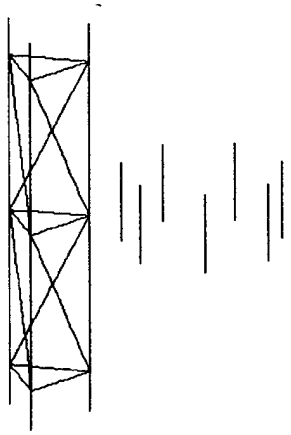

(a) NEC simulation
7-element circular array
next to a tower structure

(b) Beam with no platform

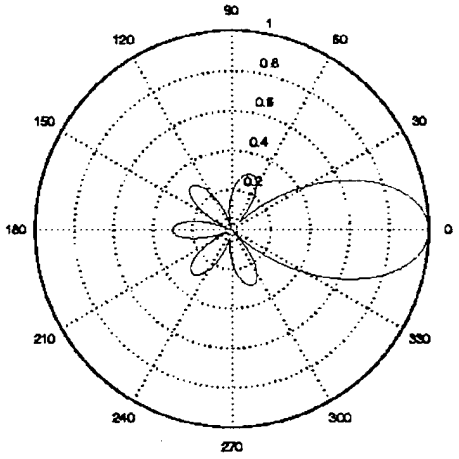

(c) Degraded beam with platform

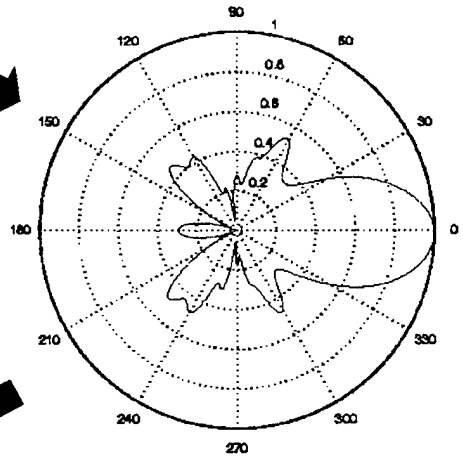

(d) GA-optimized beam

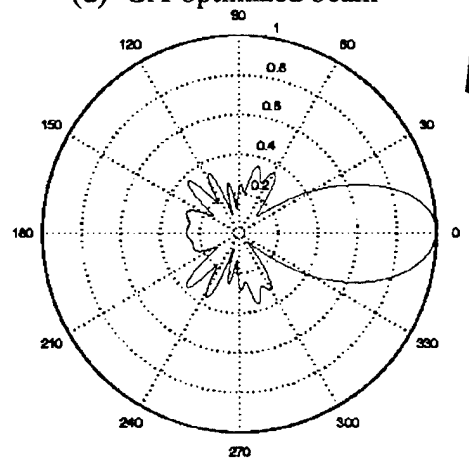

Fig. 3. GA-based beamforming by using NEC-generated active element patterns. (a) Geometry of the array with tower. (b) Beam pattern of a free-standing array using cophasal excitation. (c) Beam pattern of the array next to the tower using cophasal excitation. (d) Beam pattern of the array next to the tower using GA-optimized excitation.

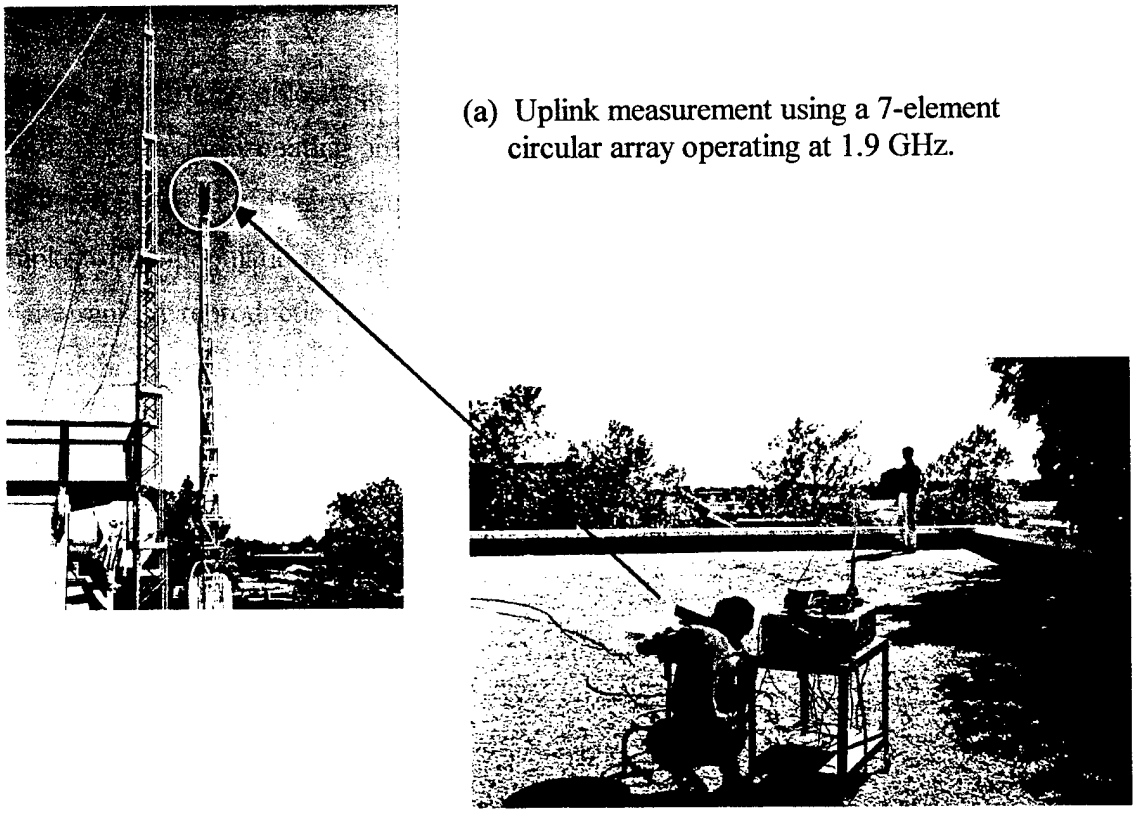

(a) Uplink measurement using a 7-element circular array operating at 1.9 GHz.

(b) Beam resulting from cophasal excitation

(c) Beam formed using GA-optimized weights

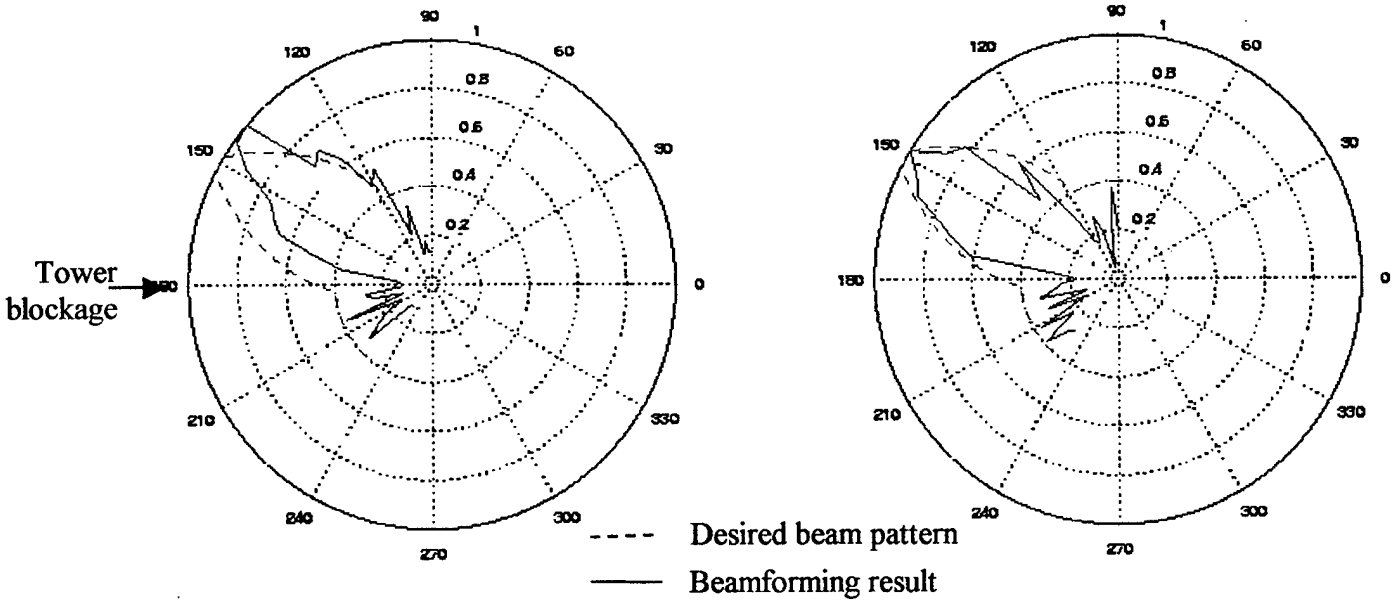

Fig. 3. GA-based beamforming by using measured active element patterns of a 7-element smart antenna array. (a) Measurement setup of the array with tower. (b) Beam pattern of the array at 150° using cophasal excitation. (d) Beam pattern of the array using GA-optimized excitation.

The tower has a triangular cross section with 3 wavelengths on each side. If the array is located in free space, a beam can be trivially synthesized in any direction based on the cophasal excitation. A sample beam is shown in Fig. 3(b). However, when the tower is present, the beam pattern degrades if the same cophasal excitation for the free-standing array is used. This is shown in Fig. 3(c), in which we observe a degraded beam with higher sidelobes. Finally, when GA is used to synthesize the beam, the beam can be nearly restored to the original free-space beam pattern, as shown in Fig. 3(d).

The algorithm has also been tested using the measured active element patterns of an existing 7-element smart antenna array at the University of Texas at Austin. The measurement setup is shown in Fig. 4(a), where the array is placed close to a metal tower. Fig. 4(b) shows the beam pattern resulting from using the standard cophasal excitation. It shows the effect of the tower when the beam is steered close to the direction of the tower. In particular, we see that the beam is squinted away from the desired 150° direction. After GA is performed to generate the optimal excitations, the resulting beam pattern in Fig. 4(c) is very close to the prescribed beam pattern. Thus the tower effect can be largely compensated by using the GA-synthesized excitation. Direction finding experiments have also carried out and showed that the GA results could be successfully used to locate emitters in direction finding applications.

Light-Weight Microwave Absorber Design. We have applied GA to the design of corrugated microwave absorbers for oblique incidence [27] (see Fig. 5). Previously, GA had been applied to the design of multi-layered planar and cylindrical absorber structures [4]. Corrugated coatings with non-planar shape profile offer an additional degree of design freedom and have been analyzed in [5]. We employ a full-wave electromagnetic solver based on this formulation to predict the performance of each shape. In general, it is more difficult to design an effective absorber for the horizontal polarization under oblique incidence than for the vertical polarization. Here the horizontal polarization is considered using the standard MAGRAM coating material backed by a conducting surface. We compare the GA-optimized shape to the conventional planar and triangular shaped coatings. Fig. 6 shows the corresponding reflection coefficients over a frequency range of interest for the three different shaped coatings. The planar shaped coating shows

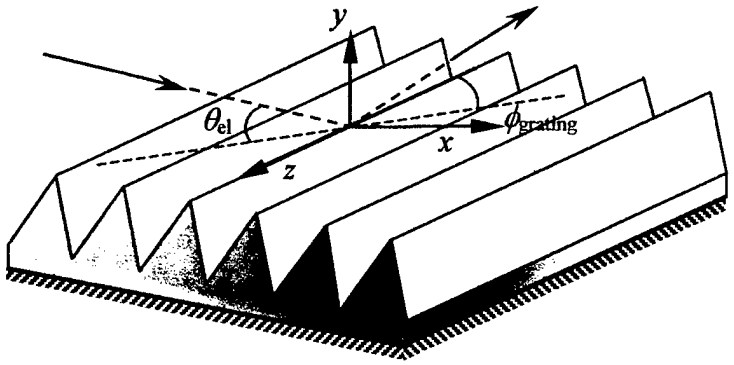

Fig. 5. Geometry of the corrugated absorber under oblique incidence.

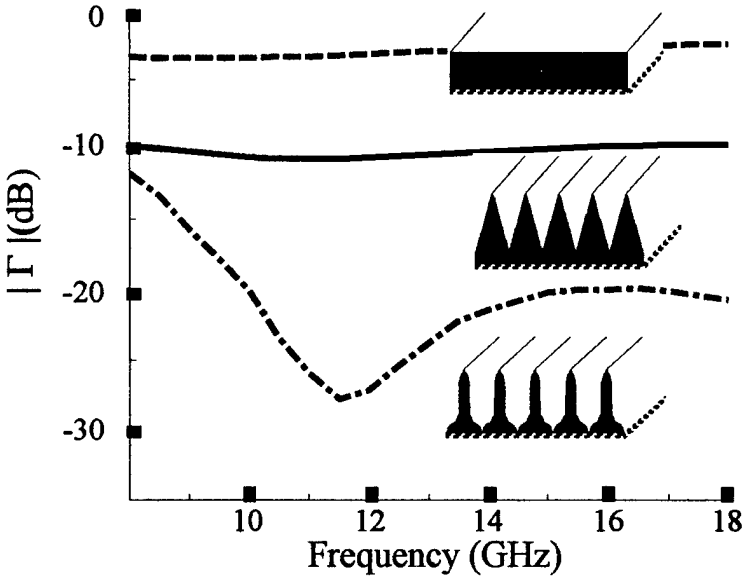

Fig. 6. Planar coated absorber (------). Conventional triangular shaped corrugated absorber (——). GA-optimized absorber for the horizontal polarization (-·-·-·-).

the largest reflection (about –5 dB) within the frequency band. By using the triangular shaped profile the reflection coefficient can be reduced to –10dB. The GA-optimized coating shows an even better absorbing performance than the triangular design. The reflection coefficient is less than –15 dB over nearly the entire frequency range. It is also noted that the GA-optimized shape resembles a rectangular profile. One possible interpretation is that a horizontally polarized wave becomes nearly vertically polarized on the vertical sidewalls of the rectangular shaped groove, and thus is easier to get absorbed by the coating.

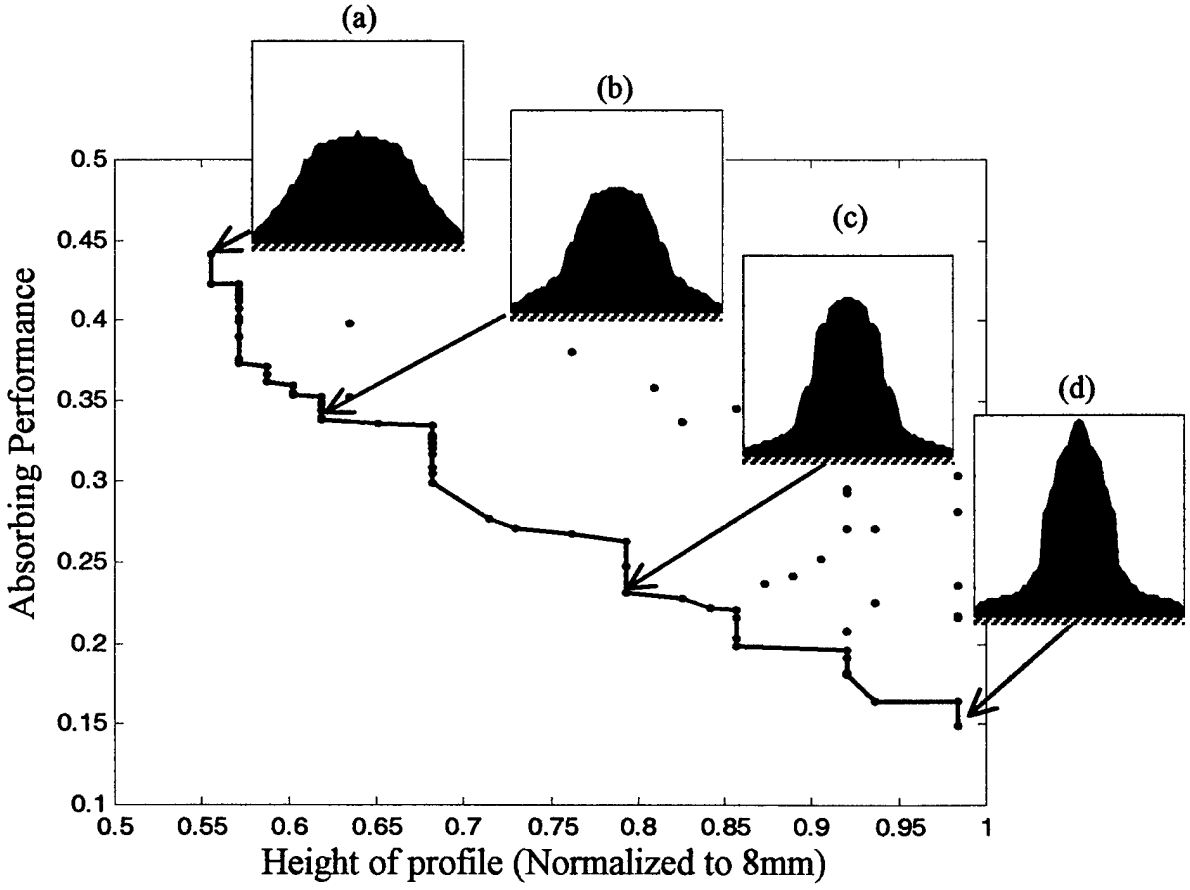

Fig. 7. Pareto front showing absorbing performance vs. height of the coating profile.

Two important objectives in the design of an absorber are good absorbing performance and low coating profile (which translates into light weight). Next, we utilize the Pareto GA [6] to carry out this multi-objective optimization efficiently. All the samples of the population are ranked using the non-dominated sorting method [7]. Based on the rank, a reproduction process is performed to refine the population into the next generation. In order to avoid the solutions from converging to a single point, we perform a sharing scheme described in [8] to generate a well-dispersed population.

We have applied the Pareto GA to corrugated coating design. In Fig. 7, the Pareto front is plotted in terms of the absorbing performance versus the height of the profile. Also shown in the insets are four optimized coating shapes that have different heights. Inset shape (a) shows the lowest profile among the four samples, but has the highest reflection. Inset shape (d) has the highest profile and the lowest reflection among the four samples. This result forms a useful design chart for signature control engineers in trading off absorber performance against coating height.

Electrically Small Wire Antenna Design. The design of electrically small antennas is currently of great interest for both HF communications (where antennas are on the order of tens of meters) and wireless handheld devices. However, miniaturization impacts both antenna efficiency and bandwidth, two critical parameters in high data rate, low power consumption systems. Fig. 8 plots the well-known theoretical bandwidth limit for miniaturized antennas derived by L. J. Chu in 1948 [9,10]. It shows that as the electrical size of the antenna (measured in terms of kr where r is the radius of the smallest sphere enclosing the antenna and $k=2\pi/(wavelength)$) is decreased, the bandwidth of the antenna is also reduced. A similar trend is also expected for the efficiency of the antenna, as the volume over which the current on the antenna can flow is decreased. Altshuler first reported on the use of GA for designing electrically small wire antennas [11]. We have applied GA in conjunction with the Numerical Electromagnetics Code to design electrically small, shaped wire antennas having maximum bandwidth and efficiency. Our objective is to devise design methodologies that can approach the fundamental limit in miniaturization. In our initial design, we used a single-arm wire with a number of bent segments. Fig. 8 shows the resulting bandwidth performance from our design method

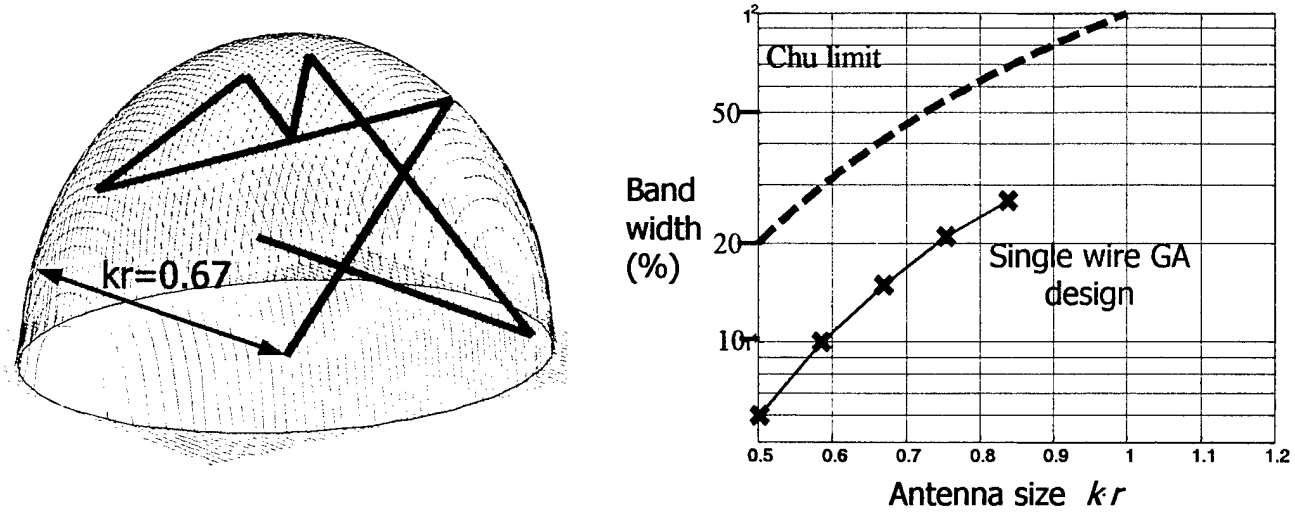

Fig. 8. Single-wire GA designs versus the Chu limit. The picture on the left shows the genetically designed antenna with 7 segments at the size of kr=0.67. The standard monopole antenna has kr=1.6.

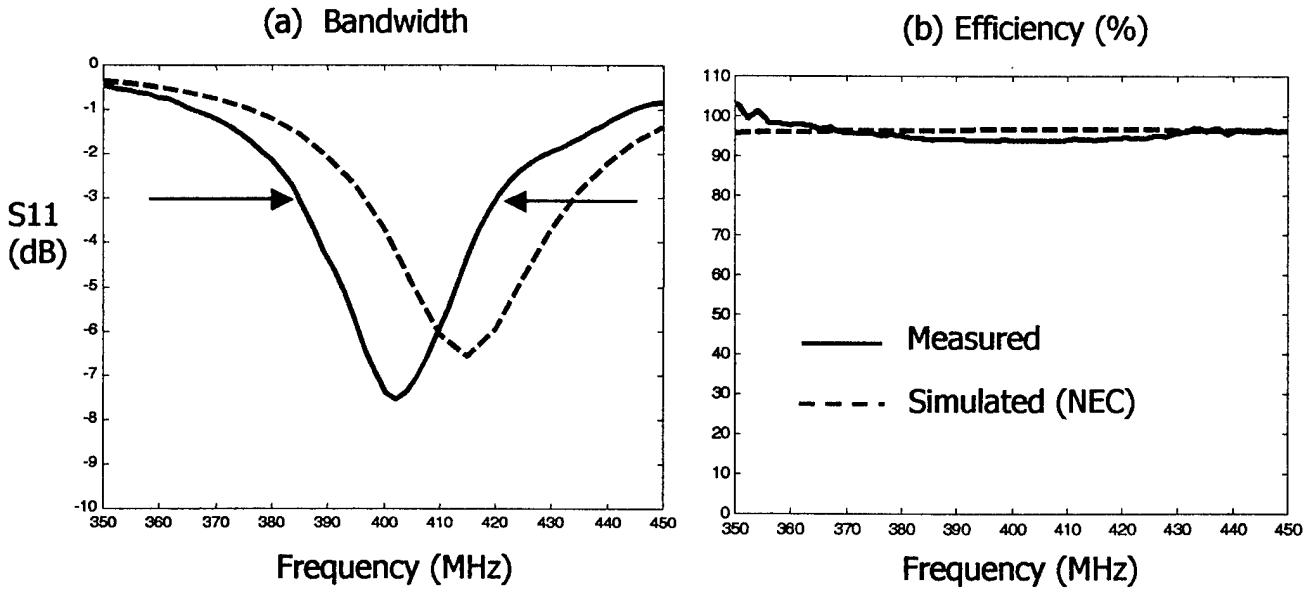

Fig. 9. Bandwidth and efficiency of the kr=0.5 GA antenna. The measured half-power bandwidth is 8.8% and the measured efficiency (using the Wheeler cap method) is 94% at the operating frequency of 400 MHz.

versus the Chu limit. Fig. 9 shows the bandwidth and efficiency comparison between the designed and measured results of a particular single-arm GA design (kr=0.5). While these initial design results are encouraging, they are still significantly below the Chu limit. We believe additional innovations can be devised to better approach the Chu limit. Furthermore, the efficiency of the antenna must also be considered in the miniaturization, and the Pareto GA scheme, which we have utilized effectively in the corrugated absorber problem, should be well suited to explore this multi-objective problem.

C. FOLLOW-UP STATEMENT:

We have obtained very encouraging results in a number of research topics. In the coming year, we will continue our research along the topics outlined above. In particular, we will: (i) extend our work in microstrip antennas to investigate antenna miniaturization using patch shapes and shorting pins, (ii) investigate the effect of mutual coupling in microstrip arrays and find ways to mitigate coupling via patch shapes to improve scan performance, (iii) further improve the design methodology of electrically small wire antennas to approach the Chu limit and map out performance bounds, (iv) investigate platform effects in small antenna design, (v) apply Pareto GA to more fully explore multi-objective antenna optimization problems, (vi) explore the design of planar, ultra-wideband antennas.

While GA is an efficient global optimizer ideally suited for exploring very complex design problems such as those outlined above, it typically requires a very large number of cost function evaluations. We will leverage against our previous research to minimize the number of CEM calculations needed for cost function computation. Particular attention will be paid to the close coupling between GA and the CEM simulator to establish a framework in which the design process can be streamlined. The potential impact of the proposed research is that novel design concepts will be uncovered that can significantly outperform conventional designs for shipboard antenna problems.

D. REFERENCES:

1. Y. Rahmat-Samii and E. Michielssen, *Electromagnetic Optimization by Genetic Algorithms*, John Wiley & Sons: New York, 1999.

2. J. M. Johnson and Y. Rahmat-Samii, "Genetic algorithms and method of moments(GA/MOM) for the design of integrated antennas," *IEEE Trans. Antennas Propagat.*, vol. 47, pp. 1606-1614, Oct. 1999.

3. R. L. Haupt, "Thinned arrays using genetic algorithms," *IEEE Trans. Antennas Propagat.*, vol. 42, pp. 993-999, 1994.

4. D. Weile, E. Michielssen and D. E. Goldberg, "Genetic algorithm design of pareto optimal broadband microwave absorbers," *IEEE Trans. Electromagnetic Compatibility*, vol. 38, pp.518-525, Aug. 1996.

5. J. Moore, H. Ling, and C. S. Liang, "The scattering and absorption characteristics of material-coated periodic grating under oblique incidence," *IEEE Trans. Antennas Propagat.*, vol. 41, pp. 1281-1288, Sept. 1996.

6. D. Goldberg, *Genetic Algorithms in Search, Optimization and Machine Learning*, Addison Wesley, Reading, MA, 1989.

7. N. Srinivas and K. Deb, "Multiobjective optimization using nondominated sorting in genetic algorithm," *J. Evolutionary Computation*, vol. 2, pp. 221-248, 1995.

8. J. Horn, N. Nafpliotis and D. E. Goldberg, "A niched pareto genetic algorithm for multiobjective optimization," *Proc. First IEEE Conf. Evolutionary Computation*, vol.1, pp. 82-87, 1994.

9. L. J. Chu, "Physical limitations of omnidirectional antennas," *J. Appl. Phys.*, vol. 19, pp. 1163-1175, Dec. 1948.

10. J. S. McLean, "A re-examination of the fundamental limits on the radiation Q of electrically small antennas," *IEEE Trans. Antennas Propagat.*, vol. 44, pp. 672-676, May 1996.

11. E. E. Altshuler, "Very small genetic antennas," *2001 USNC/URSI Nation Radio Science Meeting*, pp. 226, Salt Lake City, UT, July 2000.

E. PUBLICATIONS:

I. LIST OF JOURNAL ARTICLES (ONR supported in whole or in part)

12. B. Jiang, T. Su and H. Ling, "Frequency interpolation of electromagnetic scattering data using a hybrid model," *Microwave Optical Tech. Lett.*, vol. 27, pp. 307-312, December 2000.

13. H. Deng and H. Ling, "Wavelet-based preconditioner for three-dimensional electromagnetic integral equations," *Elect. Lett.*, vol. 36, pp. 2063-2065, December 2000.

14. H. Choo, A. Hutani, L. C. Trintinalia and H. Ling, "Shape optimization of broadband microstrip antennas using genetic algorithm," *Elect. Lett.*, vol. 36, pp. 2057-2058, December 2000.

15. T. Su and H. Ling, "On modeling mutual coupling in antenna arrays using the coupling matrix," *Microwave Optical Tech. Lett.*, vol. 28, pp. 231-237, February 2001.

16. T. Su, Y. Wang and H. Ling, "A frequency extrapolation technique for computing antenna-platform radiation problems," *J. Electromag. Waves Applications*, vol. 15, pp. 865-883, July 2001.

17. L. C. Trintinalia and H. Ling, "First order triangular patch basis functions for electromagnetic scattering analysis," *J. Electromag. Waves Applications*, vol. 15, pp. 1521-1537, November 2001.

18. T. Su and H. Ling, "On the simultaneous modeling of array mutual coupling and array-platform interactions," to appear in *Microwave Optical Tech. Lett.*, May 2002.

19. K. R. Dandekar, H. Ling and G. Xu, "Experimental study of mutual coupling compensation in smart antenna applications," to appear in *IEEE J. Selected Areas in Communications*, 2002.

20. H. Deng and H. Ling, "An efficient preconditioner for electromagnetic integral equations using pre-defined wavelet packet basis," to appear in *IEEE Trans. Antennas Propagat.*, September 2002.

21. Y. Wang and H. Ling, "Efficient radar signature prediction using a frequency-aspect interpolation technique based on adaptive feature extraction," to appear in *IEEE Trans. Antennas Propagat.*, January 2002.

22. H. Choo and H. Ling, "Design of broadband and dual-band microstrip antennas on FR-4 substrate using the genetic algorithm," submitted for publication in *IEE Proc. – Microwaves Antennas Propagat.*, September 2001.

23. H. Deng and H. Ling, "An efficient wavelet preconditioner for iterative solution of three-dimensional electromagnetic integral equations," submitted for publication in *IEEE Trans. Antennas Propagat.*, November 2001.

24. H. Choo and H. Ling, "Design of multi-band microstrip antennas using a genetic algorithm," submitted for publication in *IEEE Microwave Wireless Components Lett.*, December 2001.

II. LIST OF CONFERENCE PROCEEDINGS (ONR supported in whole or in part)

25. K. Dandekar, H. Ling and G. Xu, "Smart antenna calibration procedure including amplitude and phase mismatch and mutual coupling effects," 2000 IEEE International Conference of Personal Wireless Communications, vol. 1, pp. 293-297, Hyberadad, India, December 2000.

26. H. Choo and H. Ling, "Design of dual-band microstrip antennas using the genetic algorithm," 17th Annual Review of Progress in Applied Computational Electromagnetics, pp. 80-88, Monterey, CA, March 2001.

27. H. Choo, H. Ling and C. S. Liang, "Design of corrugated absorbers for oblique incidence using genetic algorithm," International IEEE AP-S Symposium, pp. 708-711, Boston, MA, July 2001.

28. A. Kerkhoff, R. Rogers and H. Ling, "The use of the genetic algorithm approach in the design of ultra-wideband antennas," IEEE Radio and Wireless Conference (RAWCON), pp. 93-96, Boston, MA, August 2001.

III. LIST OF RELATED PRESENTATIONS

29. H. Ling, "Joint time-frequency processing of NATO radar data," kickoff meeting of the Naval International Cooperative Opportunities in Science and Technology (NICOP) program on Time-Frequency ISAR, London, England, March 29, 2001.

30. H. Ling, "Computational electromagnetics research at the University of Texas," kickoff meeting of the National Radar Signature Center, SAIC-DEMACO, Champaign, Illinois, May 8, 2001.

31. T. Su, H. Ling and H. Foltz, "Direction-of-arrival statistics of urban propagation channel at 1.9 GHz based on measurement and ray tracing," URSI National Radio Science Meeting, p. 232, Boston, MA, July 2001.

32. T. Su, K. Dandekar and H. Ling, "Array pattern synthesis in the presence of a mounting tower using the genetic algorithm," URSI National Radio Science Meeting, p. 84, Boston, MA, July 2001.

33. H. Choo, A. Hutani and H. Ling, "Shape optimization of microstrip antennas using genetic algorithm," URSI National Radio Science Meeting, p. 144, Boston, MA, July 2001.

34. Y. Zhou and H. Ling, "Shape reconstruction of metallic objects with strong multiple scattering using genetic algorithm," URSI National Radio Science Meeting, p. 287, Boston, MA, July 2001.

35. H. Ling, "Joint time-frequency processing of NATO radar data," invited talk, NATO Task Group 22 Meeting on Generation of Synthetic Data Bases for Non-Cooperative Air Target Identification, Dayton, Ohio, October 16, 2001.

IV. LIST OF THESES AND DISSERTATIONS

Ph.D.

T. Su, "Characterization of antenna radiation and receiving properties in complex environments based on physical models," May 2001.

K. Dandekar, "Space division multiple access systems: computational electro-magnetic studies of the physical and network layers," May 2001

M.S.

A. Kerkhoff, "The use of the genetic algorithm approach in the design of ultra-wideband antennas," August 2001.

V. CONTRACTS AND GRANTS

H. Ling, "Application of model-based signal processing and genetic algorithms for shipboard antenna design, placement and optimization," Office of Naval Research, December 1, 2000 - November 30, 2002.

H. Ling, "MURI center for computational electromagnetics research," Air Force Office of Scientific Research (via Univ. of Illinois), December 15, 1995 – May 31, 2001.

H. Ling, "Radar image enhancement, feature extraction and motion compensation using joint time-frequency techniques," Office of Naval Research, April 15, 1998 – September 30, 2001.

H. Ling, "Agilent microwave network analyzer," Equipment donation, Motorola-Austin, September 2001.

D. T. Jaffe and H. Ling, "High index grisms for mid-infrared spectroscopy," NASA, June 1, 1999 – May 31, 2001.

G. Xu, H. Ling and H. D. Foltz, "Development of wideband vector channel models and testbed for 3rd generation wireless mobile systems," Texas Advanced Technology Program, January 1, 2000 - August 31, 2002.

F. INTERACTIONS/COLLABORATIONS WITH NAVY SCIENTISTS:

We presented a paper at the "H-infinity for Antennas" session of the 2001 Applied Computational Electromagnetics Society meeting held at the Naval Postgraduate School. We continue to interact closely with Dr. Victor Chen of Naval Research Lab and Dr. Brett Borden of Naval Air Warfare Center on a separate ONR program in applying joint time-frequency processing to inverse synthetic aperture radar imagery. We expect to generate cross-fertilization of ideas with the H-infinity program since a good physical understanding of electromagnetic radiation and scattering phenomena is the basis of our work in both programs. We also continue to participate in the Electromagnetics Code Consortium (EMCC), in which Navy scientists including Dr. John Asvestas (NAVAIR), Dr. William Pala (Naval Research Lab) and Dr. Helen Wang (Naval Air Warfare Center) play very active roles.

G. NEW DISCOVERIES, INVENTIONS, OR PATENT DISCLOSURES:

H. Choo and H. Ling, "Microstrip antennas and methods of designing same," provisional patent application, docket no. 5119-09201, submitted December 14, 2001.

H. HONORS AND AWARDS:

None.

APPENDIX

Publications Supported by ONR Grant

FREQUENCY INTERPOLATION OF ELECTROMAGNETIC SCATTERING DATA USING A HYBRID MODEL

Bin Jiang,[1] Tao Su,[1] and Hao Ling[1]
[1] Department of Electrical and Computer Engineering
University of Texas at Austin
Austin, Texas 78712-1084

Received 19 June 2000

ABSTRACT: *A frequency-interpolation algorithm for electromagnetic scattering data from large, complex targets is proposed. It is based on the hybridization of the existing multiple-arrival model and the rational-function model. At each point on the target, the induced current is parameterized using both models separately. The model that best matches the scattering physics at that location is chosen based on the resulting interpolation error. As a result, those regions on the target that are best described by ray-optical phenomena are interpolated by the multiple-arrival model, while those regions that exhibit resonance phenomena are interpolated by the rational-function model. Numerical results show that the hybrid scheme is superior to either the multiple-arrival model or the rational-function model for a target containing complex features.* © 2000 John Wiley & Sons, Inc. Microwave Opt Technol Lett 27: 307–312, 2000.

Key words: *frequency interpolation; method of moments; multiple-arrival model; rational-function model*

1. INTRODUCTION

The electromagnetic scattering data from a complex target are often of interest over a broad band of frequencies. To simulate multiple-frequency data using a frequency-domain computational electromagnetics solver is an exhaustive procedure as the computation must be carried out one frequency at a time. The problem is further compounded by the fact that the required sampling density in frequency is approximately proportional to the size of the target. For large complex targets, it is therefore desirable to develop algorithms to generate a dense set of frequency data from a very sparse set of computed frequency points to save computation time. This frequency-interpolation problem was recently addressed in [1] using a model-based approach based on a high-frequency model. The current at each point on the target is modeled by a collection of time-of-arrival mecha-

Contract grant sponsor: Office of Naval Research
Contract grant number: N00014-98-1-0178
Contract grant sponsor: Air Force MURI Center for Computational Electromagnetics
Contract grant number: AFOSR F49620-96-1-0025

nisms arising from multiple scattering (see Fig. 1). The time of arrival and the strength of the different mechanisms are extracted from the available frequency data using the adaptive feature extraction (AFE) algorithm [2]. It was shown that good interpolation results can be obtained even for very sparsely sampled data in frequency.

In this paper, we set out to improve the accuracy of the above interpolation algorithm for complex targets by incorporating additional scattering physics in the model. The multiple-arrival model is well matched to the ray-optical description of fields and currents. However, more general targets contain not only large-scale features, but also small resonant features. Although these resonant contributions are, in general, weaker than the returns from large-scale features, they do impact the accuracy of the interpolation if not properly taken into account. The multiple-arrival model, however, is not a good model for resonance phenomena as many time-of-arrival terms are required to adequately describe resonance. A much better model is the rational-function model, which has been widely used in frequency-interpolation problems in the resonant region [3–8]. It can be shown that the multiple-arrival model and the rational-function model are, in fact, complementary models. The former is a sum of exponentials in frequency, while the latter is a sum of exponentials in time. To take advantage of the strength of each model, we propose here a hybrid interpolation scheme that uses the most appropriate model over different portions of the target. At each point on the target, we parameterize the induced current using both models separately. Next, by using the resulting parameterization error as the selection criterion, we choose the model that best matches the scattering physics at that location. The total scattered field is then constructed from the interpolated currents. Section 2 describes our formulation. The two models and the methods for parameterization are first summarized. They are followed by the hybrid procedure. Our test results in Section 3 show that the hybrid scheme is superior to either the multiple-arrival or the rational-function model alone for a target containing complex features.

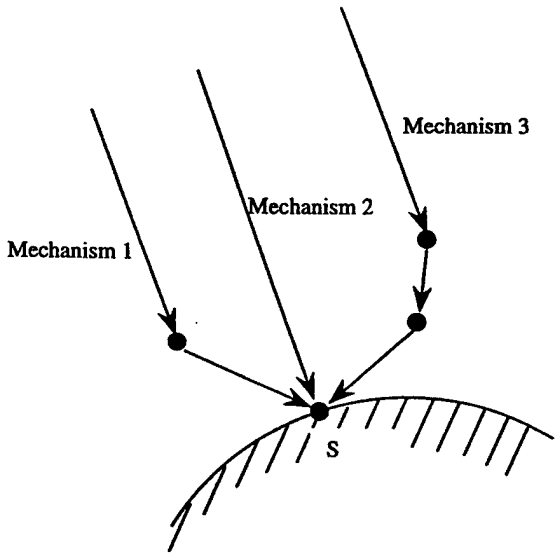

Figure 1 Multiple-arrival model for the induced current

2. FORMULATION

2.1. Multiple-Arrival Model and AFE Interpolation Algorithm. In the multiple-arrival model, we assume that the induced current at a point on the target can be written as a summation of multiple-scattering mechanisms from M different incident paths (see Fig. 1):

$$J(f) = \sum_{i=1}^{M} A_i \exp(-j2\pi f t_i) \frac{f^{\alpha_i}}{\sqrt{\sum_p |f_p^{\alpha_i}|^2}} \tag{1}$$

where f is the frequency, t_i is the time of arrival for mechanism i, and A_i is the corresponding excitation amplitude. This time-of-arrival model is based on high-frequency ray-optical phenomena, and has been well utilized in the electromagnetics community [9–11]. The last term in this model incorporates an additional frequency-dependent factor α_i, which was not used in [1]. It is consistent with high-frequency diffraction theory [10, 12, 13], and improves the accuracy of the model. Lastly, the extra factor in the denominator is included for normalization.

To determine the unknowns in the model based on the available frequency samples of the current, we use the adaptive feature extraction algorithm [2]. The parameterization is carried out in an iterative manner starting from the strongest mechanism. The sampled frequency response is first projected onto the complex conjugate of the model bases for all possible values of t_j and α_j. We then select the basis that gives the maximum projection value. This is described as follows:

$$A_i = \max \left\langle J_i(f), \exp(j2\pi f t_j) \frac{f^{\alpha_j}}{\sqrt{\sum_p |f_p^{\alpha_j}|^2}} \right\rangle \tag{2}$$

where the inner product in the above formula is defined as

$$\langle a(f), b(f) \rangle = \frac{1}{N} \sum_{p=1}^{N} a(f_p) b(f_p). \tag{3}$$

After the strongest feature with (A_i, t_i, α_i) is captured, that feature is subtracted from the signal to generate a remainder signal:

$$J_{i+1}(f) = J_i(f) - A_i \exp(-j2\pi f t_i) \frac{f^{\alpha_i}}{\sqrt{\sum_p |f_p^{\alpha_i}|^2}}. \tag{4}$$

The above procedure is iterated to extract the parameters for each scattering mechanism until the remaining signal reaches a sufficiently small level.

A key concept in AFE is to use random frequency sampling during the original data generation to avoid the ambiguity in selecting the strongest feature [1]. Therefore, the frequencies at which the electromagnetic computations are carried out should not be evenly spaced. In addition, since the strongest feature contains interference from the weaker features, the amplitude of each feature is not extracted perfectly using AFE. We have found that, by performing a linear least square optimization for the amplitude parameter

after the whole iteration procedure, the AFE performance is significantly improved.

2.2. Rational Function Model and Cauchy Method. The multiple-arrival model and AFE can be used to effectively carry out frequency interpolation for targets containing ray-optical phenomena. For target resonance, however, it is more appropriate to use a rational-function model to describe the frequency resonance mechanism. The rational-function model is introduced below, and the Cauchy method for determining the model parameters is summarized. The reader is referred to [5, 6] for a detailed description of the method.

Consider the frequency response of a system $H(s)$. From circuit theory, it is customary to describe $H(s)$ by the ratio of two polynomials $A(s)$ and $B(s)$ as follows:

$$H(s) = \frac{A(s)}{B(s)} = \frac{\sum_{k=0}^{P} a_k s^k}{\sum_{k=0}^{Q} b_k s^k}. \tag{5}$$

For $Q > P$, this is a pole model, and thus can be used to describe the strong resonance behavior of the current in the frequency domain by the proper choice of the pole locations.

Given the value of $H(s)$ and its frequency derivatives at some frequency points s_n, the Cauchy problem is stated as

$$\text{given } H^j(s_n), \quad \text{for } j = 0,\ldots,J,\ n = 1,\ldots,N$$
$$\text{find } P \text{ and } Q, \quad \{a_k,\ k = 0,\ldots,P\} \text{ and } \{b_k,\ k = 0,\ldots,Q\}.$$

where $H^j(s_n)$ represents the jth frequency derivative of H at s_n. Equation (5) can be rearranged into a matrix form as follows:

$$[A \quad -B]\begin{bmatrix} a \\ b \end{bmatrix} = 0 \tag{6}$$

where

$$A(n,k) = \frac{k!}{(k-j)!} s_n^{(k-j)} u(k-j) \tag{7}$$

and

$$B(n,k) = \sum_{i=0}^{j} C_{j,i} H^{(j-i)}(s_n) \frac{k!}{(k-i)!} s_n^{(k-j)} u(k-i). \tag{8}$$

Here, $u(k)$ is 0 for $k < 0$ and 1 otherwise, $C_{j,i} = (j!/(i!(j-i)!))$, $a = [a_1 a_2 a_3 \cdots a_P]^T$, and $b = [b_1 b_2 b_3 \cdots b_Q]^T$. To solve for the polynomial coefficients a_k and b_k from the matrix equation (5), singular value decomposition is utilized. The model orders P and Q can be estimated from the number of significant singular values. The singular vector corresponding to the smallest singular value is chosen to be the solution of (6).

Several comments are in order. First, the quantity to be interpolated in our problem is the frequency response of the current. Thus, $H(s) = J(f)$ where $s = j2\pi f$. Second, we only use frequency points, and not frequency derivatives as the input to the Cauchy algorithm. This is for ease of hybridization with the AFE algorithm. Furthermore, for an iterative solution to electromagnetic integral equations, the computational complexity to generate the frequency derivative of the current is as high as that for a new frequency point. Third, instead of estimating the orders of the polynomial functions, we choose $Q = P + 1$ and $P + Q + 1 = N$ in our implementation. We find that our results are not very sensitive to the order estimation. Lastly, we note that the frequency points need not be equally spaced in carrying out the Cauchy method. This gives us the possibility to use the same set of sampled data for both the Cauchy and AFE interpolation schemes.

2.3. Hybrid AFE–Cauchy Algorithm. We are now armed with two interpolation algorithms. The AFE algorithm works well for low-order multiple-scattering mechanisms that resemble high-frequency ray optics, while the Cauchy algorithm is better suited for describing resonance phenomena. The essential idea of the hybrid algorithm is to choose the most appropriate model for the current at each point on the target. Our approach is as follows. At each point on the target, we first parameterize the induced current using both the AFE and Cauchy algorithms separately, with the same set of sampled frequency responses. The model that best matches the scattering physics at that location is then chosen. In the actual implementation, the selection is made by comparing the interpolated data from the two models against the brute-force computation at several new frequency points. The model with the smaller interpolation error is chosen for that location. As a result, the surface of the target can be divided into two regions—the AFE region and the Cauchy region. Over the AFE region, the currents exhibit high-frequency scattering phenomenology. Over the Cauchy region, the currents exhibit strong resonance. Once the parameterization and model determination have been made, the interpolated currents on the target over the frequency band of interest can be generated. Therefore, the scattered far field can be obtained by integrating the induced current over the target at any frequency of interest.

It has been pointed out that the AFE algorithm requires as its input the currents computed at a set of nonuniformly sampled frequencies. In fact, the more random the sampling, the better the performance of the AFE. It has also been noted that, in the Cauchy algorithm, the frequency points need not be uniformly sampled. However, equally spaced frequency points increase the chance for the Cauchy method to accurately capture the poles in the frequency domain. Consequently, we find contradictory requirements for the optimal sampling in frequency between the AFE and Cauchy algorithms. AFE requires random sampling, while Cauchy prefers uniform sampling. Here, we choose a compromise solution, i.e., semirandom sampling. To choose the N frequency points needed for interpolation, we first equally divide the whole frequency band into N uniformly spaced subbands. The sampling point within each subband is chosen randomly based on a uniform probability distribution. The sampled data can then be used in both algorithms.

3. NUMERICAL EXAMPLE

We consider a 2-D conducting target as shown in Figure 2. Although this plate-like target looks simple, its scattering characteristics involve a variety of scattering mechanisms [14]. An E-polarized plane wave is incident at an angle of 60° from the right. The reference backscattering data versus frequency are first computed using the method of moments (MoM) at 100 frequency points from 0.1 to 10 GHz in 0.1 GHz steps. The frequency response of the backscattered field is plotted

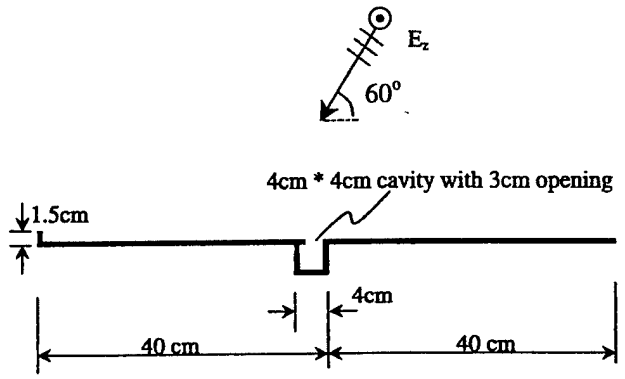

Figure 2 Geometry of the conducting plate with cavity and fin

as the solid line in Figure 3. By inverse Fourier transforming the frequency data, the range profile of the target can be generated. It is plotted in Figure 4 as the solid curve (a Hamming window has been applied to reduce range sidelobes). We recognize four large peaks in the range profile, which correspond, respectively, to the scattering from the right edge of the plate, the aperture of the partially open cavity, the interior of the cavity, and the small fin at the left edge. The resonant behavior of the cavity interior can clearly

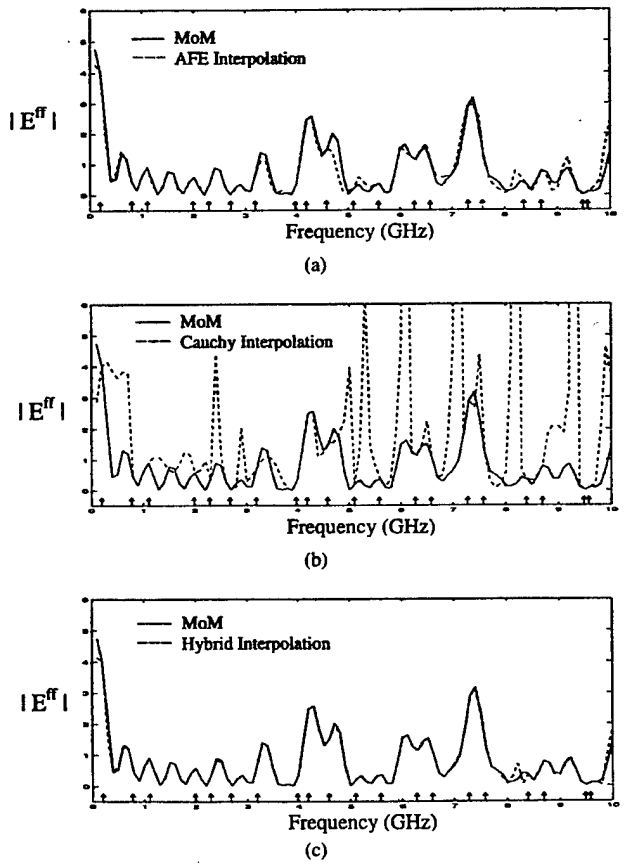

Figure 3 (a) Comparison of the backscattered field versus frequency between the brute-force MoM and the AFE interpolation results based on 20 points. (b) Comparison of the backscattered field versus frequency between the brute-force MoM and the Cauchy interpolation results based on 20 points. (c) Comparison of the backscattered field versus frequency between the brute-force MoM and the hybrid interpolation results based on 20 points

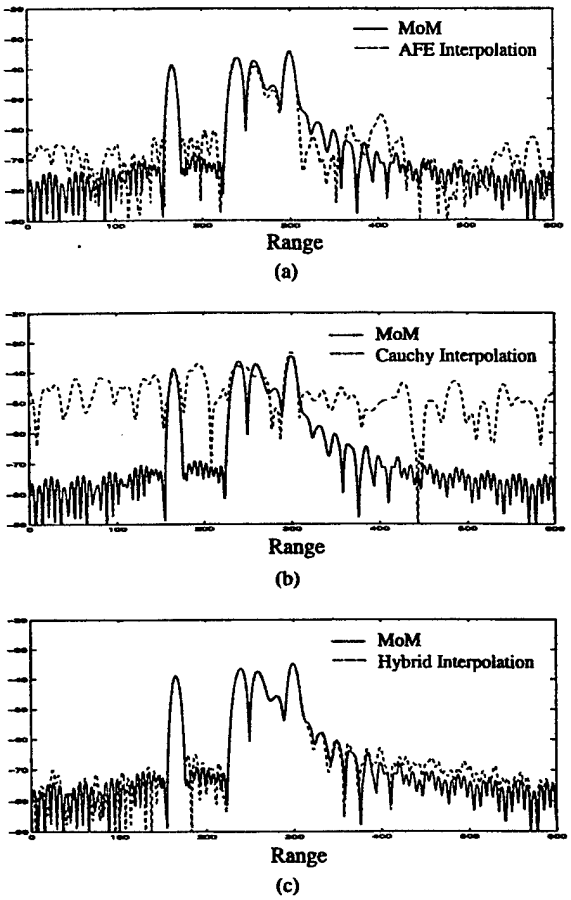

Figure 4 (a) Comparison of the range profiles generated from the brute-force MoM and the AFE-interpolated data. (b) Comparison of the range profiles generated from the brute-force MoM and the Cauchy-interpolated data. (c) Comparison of the range profiles generated from the brute-force MoM and the hybrid-interpolated data

be seen as dispersive ringing occurs after the third peak and overlaps with the fourth peak. We should note that the frequency response is marginally sampled at a step size of 0.1 GHz. Further undersampling will result in a loss of features in the frequency domain or aliasing in the time/range domain.

We next carry out the frequency interpolation using only 20 frequency points. The locations of the 20 frequency points are chosen semirandomly, as discussed in the last section, and are indicated as small arrows along the frequency axis in Figure 3. First, the target current is interpolated using the AFE algorithm based on the multiple-arrival model over the whole target surface. The interpolated result is plotted as the dashed line in Figure 3(a). Compared to the reference result from the brute-force MoM, AFE gives rather good performance, and can capture most of the features in the scattered field. The largest error in the AFE result occurs at frequencies around 4.5 and 9 GHz, which are close to the first two resonant frequencies of the small cavity. This observation is further corroborated in the corresponding range profile from the AFE-interpolated data, shown as the dashed curve in Figure 4(a). The AFE algorithm performs well in predicting the three strong peaks due to the exterior features on the target. However, it has trouble predicting the resonant cavity return, which is rather dispersive in range.

Next, the Cauchy method is used to interpolate the current over the entire target surface. The frequency response and the range profile results are shown, respectively, in Figures 3(b) and 4(b) as dashed lines. Since the rational function is a pole model, we find that the Cauchy algorithm tries hard to capture the poles of the system. However, since the current is sparsely sampled in frequency, an incorrect pole location and pole strength are generated. This is particularly true for low-order multiple-scattering events that have a large delay spread in the times of arrival. The long delay spread in time translates into rapid oscillations in the frequency response, and a very high model order is needed to adequately model the response using poles. From the range profile in Figure 4(b), we see that the Cauchy algorithm gives extremely poor results. Thus, the Cauchy algorithm cannot be used by itself to carry out the frequency interpolation of large targets that are dominated by ray-optical phenomena.

Finally, we apply the hybrid interpolation algorithm. The selection between the Cauchy-interpolated and the AFE-interpolated currents at each point on the target surface is made by comparing them against the reference current at three extra test frequencies. The chosen interpolated currents are then used to generate the backscattered field, as shown in Figure 3(c). When compared to Figure 3(a) and (b), the hybrid result shows an obvious improvement in its agreement with the reference result. Note that the error near the cavity resonant frequencies in Figure 3(a) is greatly reduced in Figure 3(c). The range profile in Figure 4(c) further substantiates this claim as both the scattering centers and the resonance of the cavity are well predicted.

Figure 5 shows how the whole target is automatically divided into two regions during the hybrid procedure, depending on the local scattering physics. The Cauchy region is shown within the open lines, while the AFE region is shown within the solid lines. The right half of the plate fits the multiple-arrival model very well, and thus is chosen as the AFE region. The cavity in the middle exhibits strong resonance, and can be well parameterized by the Cauchy method. As for the left half of the plate, we expect it to be an AFE region with the same scattering mechanisms as the right-half part. However, since the delay spread in the times of arrival between the direct incident wave and the scattered wave from the fin at the left edge is small, the Cauchy method has a sufficient model order to parameterize the scattering behavior. In fact, we find that either the Cauchy or the AFE model may be chosen in this region with equally good results.

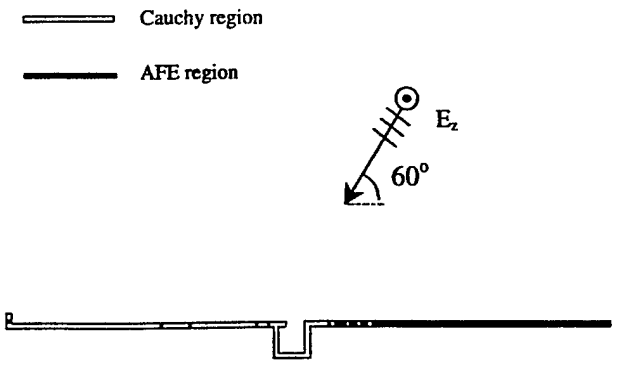

Figure 5 Illustration of how different portions of the target are parameterized in the hybrid approach. The Cauchy region is shown within the open lines, and the AFE region is shown within the solid lines

4. SUMMARY

In this paper, we have proposed a frequency-interpolation algorithm for electromagnetic scattering data from large, complex targets. It is based on the hybridization of the existing multiple-arrival model and the rational-function model. The adaptive feature extraction algorithm is used to extract the parameters in the multiple-arrival model, while the parameters in the rational-function model are obtained using the Cauchy method. At each point on the target, we first parameterize the induced current using both the AFE and Cauchy algorithms separately. The model that best matches the scattering physics at that location is automatically chosen based on the resulting interpolation error. Consequently, those regions on the target that are best described by ray-optical phenomena are interpolated by the multiple-arrival model, while those regions that exhibit resonance phenomena are interpolated by the rational-function model. Numerical results for a target containing complex features have demonstrated that the hybrid model results in more accurate interpolation than either of the two models alone. The hybrid interpolation scheme is quite robust, and can lead to significant computational savings since broadband signature data can be generated from a very sparse set of computed frequency points. Extension of this algorithm to 3-D, nonconducting targets is currently being investigated.

REFERENCES

1. Y. Wang and H. Ling, Efficient radar signature prediction using a frequency-aspect interpolation technique based on adaptive feature extraction, IEEE Trans Antennas Propagat (submitted, June 1999).
2. Y. Wang and H. Ling, Adaptive ISAR construction from non-uniformly undersampled data, IEEE Trans Antennas Propagat, 48 (2000), 329–331.
3. E.K. Miller, Model-based parameter estimation in electromagnetics: Part I. Background and theoretical development, Appl Comput Electromag Newsletter 10 (1995).
4. G.J. Burke, E.K. Miller, S. Chakrabarti, and K. Demarest, Using model-based parameter estimation to increase the efficiency of the computing electromagnetic transfer functions, IEEE Trans Magn, 25 (1989), 2807–2809.
5. R.S. Adve, T.K. Sarkar, D.M. Rao, E.K. Miller, and D.R. Pflug, Application of the Cauchy method for extrapolating/interpolating narrow band system responses, IEEE Trans Microwave Theory Tech, 45 (1997), 837–845.
6. K. Kottapalli, T.K. Sarkar, Y. Hua, E.K. Miller, and G.J. Burke, Accurate computation of wide-band response of electromagnetic systems utilizing narrow-band information, IEEE Trans Microwave Theory Tech, 39 (1991), 682–687.
7. C.J. Reddy, M.D. Deshpande, C.R. Cockrell, and F.B. Beck, Fast RCS computation over a frequency band using method of moments in conjunction with asymptotic waveform evaluation technique, IEEE Trans Antennas Propagat, 46 (1998), 1229–1233.
8. F. Ling, D. Jiao, and J.M. Jin, Efficient electromagnetic modeling of microstrip structures in multilayer media, IEEE Trans Microwave Theory Tech, 47 (1999), 1810–1818.
9. M. Hurst and R. Mittra, Scattering center analysis via Prony's method, IEEE Trans Antennas Propagat, AP-35 (1987), 986–988.
10. L.C. Potter, D.M. Chiang, R. Carriere, and M.J. Gerry, A GTD-based parametric model for radar scattering, IEEE Trans Antennas Propagat, 43 (1995), 1058–1067.
11. Y. Wang and H. Ling, Radar signature prediction using moment

method codes via a frequency extrapolation technique, IEEE Trans Antennas Propagat, 47 (1999), 1008–1015.
12. A. Moghaddar, Y. Ogawa, and E.K. Walton, Estimating the time-delay and frequency delay parameter of scattering components using a modified MUSIC algorithm, IEEE Trans Antennas Propagat, 42 (1994), 1412–1418.
13. T. Su, Y. Wang, and H. Ling, A frequency extrapolation technique for computing antenna-platform radiation problem, IEEE Trans Antennas Propagat (submitted, Sept. 1999).
14. J. Moore and H. Ling, Super-resolved time-frequency analysis of wideband backscattered data, IEEE Trans Antennas Propagat, 43 (1995), 623–626.

© 2000 John Wiley & Sons, Inc.

Wavelet-based preconditioner for three-dimensional electromagnetic integral equations

H. Deng and H. Ling

A wavelet-based method is proposed to effectively precondition 3D electromagnetic integral equations. The approximate-inverse preconditioner is constructed in the wavelet domain where both the moment matrix and its inverse exhibit sparse, multilevel finger structures. The inversion is carried out as a Frobenius-norm minimisation problem. Numerical results on a 3D cavity show that the iteration numbers are significantly reduced with the preconditioned system. The computational cost of the preconditioner is kept under $O(M \log N)$.

Introduction: There is growing interest in the computational electromagnetics community on the use of the fast multipole method (FMM) [1] for solving large-scale electromagnetic integral equations. With the multilevel implementation of the FMM, the computational complexity and storage requirement can be reduced to $O(M \log N)$ for the (moment matrix)-(vector) product. To take advantage of this reduced complexity, iterative solvers must be

used. However, the convergence rate of the iterative solution process is strongly problem-dependent. For scattering geometries involving multiple interactions such as partially open cavities, the moment matrices are severely ill-conditioned and preconditioning is need to accelerate the convergence rate [2]. Some well-documented preconditioning methods such as incomplete LU-factorisation (ILU) [3] may be effective, but usually require well-above $O(N\log N)$ complexity to implement. In this Letter, we propose a new wavelet-based method to construct an effective preconditioner for 3D moment equations. The algorithm is based on determining an approximate inverse for the moment matrix in the wavelet transform domain. The computational cost of the preconditioner is kept under $O(N\log N)$, making it compatible with the FMM.

Problem formulation: Consider a 3D moment equation in the space domain:

$$[\mathbf{Z}]\mathbf{J} = \mathbf{E} \tag{1}$$

where [Z], J and E are, respectively, the moment matrix, the induced current vector and the excitation vector. If eqn. 1 is left-preconditioned by a preconditioner [P], we obtain

$$[\mathbf{P}][\mathbf{Z}]\mathbf{J} = [\mathbf{P}]\mathbf{E} \tag{2}$$

Our approach is to try to construct a [P] that is the approximate inverse of [Z] using the wavelet transform. The moment equation in eqn. 1 can be represented using wavelet basis as

$$[\tilde{\mathbf{Z}}]\tilde{\mathbf{J}} = \tilde{\mathbf{E}} \tag{3}$$

where

$$[\tilde{\mathbf{Z}}] = [\mathbf{M}]^T[\mathbf{Z}][\mathbf{M}] \qquad [\tilde{\mathbf{J}}] = [\mathbf{M}]^T\mathbf{J} \qquad [\tilde{\mathbf{E}}] = [\mathbf{M}]^T\mathbf{E} \tag{4}$$

and [M] is the unitary wavelet transform matrix. Note that in 3D problems [Z] is strongly diagonal-dominant. Consequently, $[\tilde{\mathbf{Z}}]$ can be effectively approximated by a sparse matrix with the multi-level 'finger' pattern discussed in [4]. Furthermore, we observe from eqn. 4 that

$$[\tilde{\mathbf{Z}}]^{-1} = [\mathbf{M}]^T[\mathbf{Z}]^{-1}[\mathbf{M}] = [\mathbf{Z}]^{\tilde{-}1} \tag{5}$$

Since the smooth parts in $[\mathbf{Z}]^{-1}$ are converted into small wavelet coefficients through the transform, $[\tilde{\mathbf{Z}}]^{-1}$ can again be approximated by a sparse matrix with the same finger pattern as $[\tilde{\mathbf{Z}}]$. With the chosen sparsity pattern for both [Z] and $[\tilde{\mathbf{Z}}]^{-1}$, the approximate-inverse preconditioner for $[\tilde{\mathbf{Z}}]$ can now be solved efficiently by casting it as a Frobenius norm minimisation problem [5]:

$$\min_{[\tilde{\mathbf{P}}]} \left\| [\tilde{\mathbf{P}}][\tilde{\mathbf{Z}}] - \mathbf{I} \right\|_F \tag{6}$$

where I is the identity matrix. Since

$$\left\| [\tilde{\mathbf{P}}][\tilde{\mathbf{Z}}] - \mathbf{I} \right\|_F = \sum_{j=1}^{N} \left\| \tilde{\mathbf{P}}_j[\tilde{\mathbf{Z}}] - \mathbf{e}_j \right\|^2 \tag{7}$$

where $\tilde{\mathbf{P}}_j$ and $\mathbf{e}_j$ are, respectively, the jth rows of $[\tilde{\mathbf{P}}]$ and I, the solution of eqn. 6 becomes the following N independent least squares problems

$$\min_{\mathbf{P}_j} \left\| \tilde{\mathbf{P}}_j[\tilde{\mathbf{Z}}] - \mathbf{e}_j \right\|^2 \qquad j = 1, 2, \ldots, N \tag{8}$$

Once $[\tilde{\mathbf{P}}]$ is solved for in the wavelet domain, the approximate-inverse preconditioner [P] can be obtained by the inverse wavelet transform:

$$[\mathbf{P}] = [\mathbf{M}][\tilde{\mathbf{P}}][\mathbf{M}]^T \simeq [\mathbf{Z}]^{-1} \tag{9}$$

Combining eqns. 2 and 9 we have the following preconditioned moment equation:

$$[\mathbf{M}][\tilde{\mathbf{P}}][\mathbf{M}]^T[\mathbf{Z}]\mathbf{J} = [\mathbf{M}][\tilde{\mathbf{P}}][\mathbf{M}]^T\mathbf{E} \tag{10}$$

To summarise, the wavelet preconditioner $[\tilde{\mathbf{P}}]$ is generated by first finding the approximate wavelet transform of the moment matrix $[\tilde{\mathbf{Z}}]$ using eqn. 4, and then solving the Frobenius-norm minimisation problem in eqn. 8. Once $[\tilde{\mathbf{P}}]$ is obtained, the preconditioning operation is carried out by a series of matrix-vector multiplication operations in eqn. 10. We now consider the computational cost of constructing $[\tilde{\mathbf{P}}]$ and that for the preconditioning operation. To construct $[\tilde{\mathbf{P}}]$, we must obtain an approximate $[\tilde{\mathbf{Z}}]$. Owing to the strong source singularity in 3D problems, [Z] can be made approximately sparse with $O(N)$ nonzero elements by ignoring the far-field interactions. Therefore, the computation of $[\tilde{\mathbf{Z}}]$ can be implemented with fast two-channel filterbank filtering with about $O(N)$ operations. Once $[\tilde{\mathbf{Z}}]$ is obtained, the complexity to solve eqn. 8 can be made proportional to the problem size N, provided that we carefully control the sparsity patterns of $[\tilde{\mathbf{Z}}]$ and its inverse. Next we consider the complexity to carry out the preconditioning operation on the left-hand side of eqn. 10. Since there are only $O(N\log N)$ nonzero elements in the wavelet transform matrix [M], the product of [M] with any vector requires $O(N\log N)$ operations. Note also that $[\tilde{\mathbf{P}}]$ is a sparse matrix with $O(N)$ nonzero elements. Therefore, if the preconditioning operation is carried out as a series of matrix-vector products on [Z]J or E, the total computation cost is limited to $O(N\log N)$ per iteration.

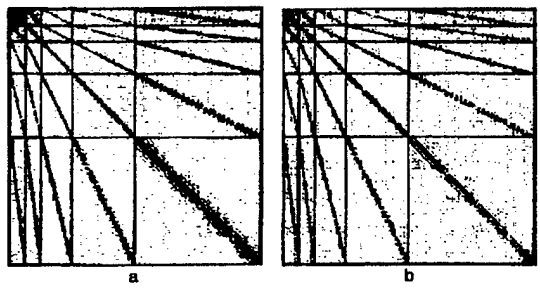

490/1

Fig. 1 *Wavelet transformed moment matrix* $[\tilde{\mathbf{Z}}]$ *and its inverse* $[\mathbf{Z}]^{-1}$ *for rectangular cavity*

Logarithmic scale with $L = 4$ ($N = 1024$)
a Wavelet transformed moment matrix
b Inverse of transformed matrix

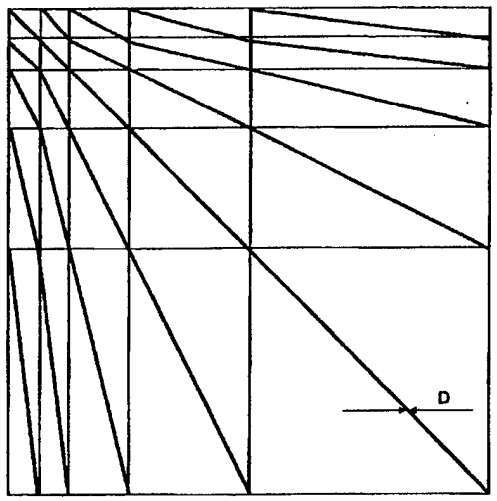

490/2

Fig. 2 *Non-zero pattern used to solve Frobenius-norm minimisation problem*

Numerical results: The algorithm is tested using a 3D conducting rectangular cavity with an open end. The (width) × (height) × (depth) dimensions of the cavity are $R \times R \times 1.5R$ where R is a size parameter. The incident plane wave is horizontally polarised with a frequency of 5.9GHz and makes an angle of 45° from the cavity opening in the elevation plane. The problem is formulated in terms of an electric-field integral equation. The Rao-Wilton-Glisson basis functions are used to form the original space-domain moment equation with a discretisation size of about $\lambda_0/10$ (or 0.2"). The greyscale magnitude plots of the wavelet-based moment matrix $[\tilde{\mathbf{Z}}]$ and its inverse $[\tilde{\mathbf{Z}}]^{-1}$ are shown, respectively, in Figs. 1*a* and *b* with a problem size of $N = 1024$ ($R \simeq 2.1$"). The wavelet filter used in the transform is the Daubechies filter of

order 6, and the maximum wavelet transform level is $L = 4$. As expected, both matrices exhibit the multilevel 'finger' structure. Accordingly we propose to use a fixed sparse matrix pattern shown in Fig. 2 with finger width D for both $[\bar{Z}]$ and $[\bar{Z}]^{-1}$ in solving the Frobenius-norm minimisation problem. If the parameters D and L are kept constant, the complexity to solve eqn. 10 is proportional to the problem size N. To investigate the performance of the preconditioner, we proportionally increase the physical size of the cavity with the parameter R changing from 1.2" to 5.1" so that N increases from 256 to 8192, while the discretisation interval and the frequency remain unchanged. The resulting iteration numbers in solving the moment equations as a function of the problem size are shown in Fig. 3. The iterative solver is BICG-STAB and a relative residual error of 0.001 is used as the stopping criterion. The maximum wavelet transform level is $L = 5$ and the finger width D of the sparsity pattern is 16 for $N < 1024$ and 32 for $N \geq 1024$. We observe that with preconditioning, the iteration numbers are very small and grow at a very slow rate with respect to the problem size. The results demonstrate the effectiveness of the new wavelet-based preconditioner for 3D moment equations.

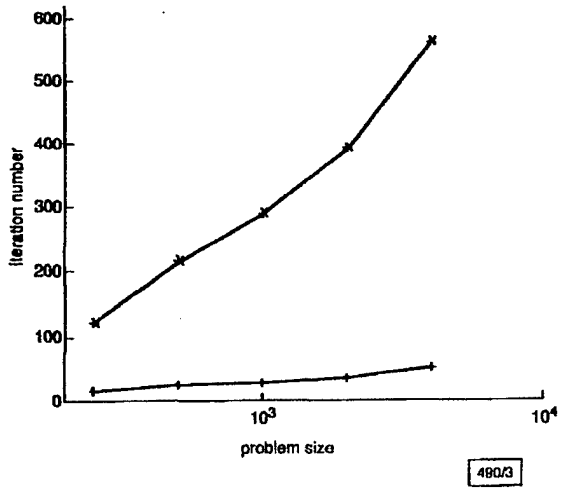

Fig. 3 *Iteration number against problem size for cavity problem*

—*— without preconditioning
—+— with wavelet preconditioner

Conclusions: We have proposed a wavelet-based preconditioner for 3D electromagnetic integral equations in this work. Numerical results showed the preconditioner is very effective for ill-conditioned cavity structures. The total computational cost for the preconditioning can be kept under $O(N\log N)$. The new algorithm is compatible with fast boundary-integral algorithms such as the multilevel FMM.

Acknowledgment: This work is supported by the Air Force MURI Center for Computational Electromagnetics under Contract No. AFOSR F49620-96-1-0025, and in part by the Office of Naval Research under Contract No. N00014-98-1-0178.

© IEE 2000
31 July 2000
Electronics Letters Online No: 20001481
DOI: 10.1049/el:20001481

H. Deng and H. Ling (*Department of Electrical and Computer Engineering, The University of Texas at Austin, Austin, TX 78712-1024, USA*)

References

1 COIFMAN, R., ROKHLIN, V., and WANDZURA, S.: 'The fast multipole method for the wave equation: a pedestrian prescription', *IEEE Antennas Propag. Mag.*, 1993, **35**, (3), pp. 7–12

2 AHN., C.H., CHEW, W.C., ZHAO, J.C., and MICHIELSSEN, E.: 'Approximate inverse preconditioner for near resonant scattering problems'. Research Report, University of Illinois, April 1998

3 BRUASET, A.M.: 'A survey of preconditioned iterative methods' (John Wiley & Sons, Inc., New York, 1995)

4 BEYLKIN, G., COIFMAN, R., and ROKHLIN, V.: 'Fast wavelet transforms and numerical algorithms I', *Com. Pure Appl. Math.*, 1991, **44**, pp. 141–183

5 GROTE, M.J., and HUCKLE, T.: 'Parallel preconditioning with sparse approximate inverse', *SIAM J. Sci. Comput.*, 1997, **19**, (3), pp. 838–853

Shape optimisation of broadband microstrip antennas using genetic algorithm

H. Choo, A. Hutani, L.C. Trintinalia and H. Ling

The genetic algorithm (GA) is used to design patch shapes for microstrip antennas on FR-4 substrate for broadband applications. Measurement results of the GA-optimised designs show good agreement with numerical prediction. The optimised patch design achieves a fourfold improvement in bandwidth when contrasted with a standard square microstrip antenna.

Introduction: It is well known that standard microstrip patch antennas exhibit very narrow bandwidth. Various broadbanding methods have been proposed to date. For instance, adding parasitic patches, using thick air substrate, stacking patches and using shorting post for reactive loading are well known techniques for extending microstrip bandwidth [1]. Recently, Johnson and Rahmat-Samii reported on the use of the genetic algorithm (GA) to search for novel patch shapes for broadband operations [2]. The attractiveness of GA shape optimisation is that improved bandwidth performance can be achieved without increasing overall volume or manufacturing cost. They used thick air substrate, and explored metallic patch sizes up to half a wavelength.

In this Letter, we also examine the use of GA for broadband applications. In contrast to the work of Johnson and Rahmat-Samii, we employ FR-4 as the substrate material, since it is the most commonly used material in wireless devices. In addition, fewer geometrical constraints are used in the GA in hope of obtaining better global optimum. We report a fourfold bandwidth improvement from our GA-optimised microstrip shape compared to that of a standard square microstrip antenna.

GA optimisation: GA is implemented to optimise the microstrip patch shape to achieve broad bandwidth. In our GA, we use a two-dimensional (2D) chromosome to encode each patch shape into a binary map [3]. The metallic sub-patches are represented by ones and the no-metal areas are represented by zeros. Since it is more desirable to obtain optimised patch shapes that are well-connected from the manufacturing point of view, a 2D median filter is applied to the chromosomes to create a more realisable population at each generation of the GA.

To evaluate the performance of each patch shape, a full-wave electromagnetic patch code is used to predict its bandwidth performance [4]. The formulation of the code is similar to that described in [5] and is based on the solution to the electric field integral equation with the periodic, layered medium Green's function as its kernel. Roof-top basis functions are used to expand the unknown current on the metal patch and fast Fourier transform is used to accelerate the computation of the matrix elements. Because of the assumed periodicity of the patches in this code, we use a large enough period to simulate a single patch.

The design goal is to broaden the bandwidth of a microstrip antenna with a centre frequency of 2GHz by changing the patch shape. To achieve the design goal, the cost function is defined as the average of those S_{11} values that exceed –10dB (i.e. VSWR = 2:1) within the frequency band of interest. The target frequency range is between 1.9 and 2.1GHz.

Based on the cost function, the next generation is created by a reproduction process that involves crossover, mutation and 2D median filtering. A two-point crossover scheme using three chromosomes is devised. The process selects three chromosomes as parents, and divides each chromosome into three parts. Intermingling the three parent chromosomes then makes three child chromosomes. This crossover scheme exhibits a more disruptive characteristic for regeneration than the conventional one-point or two-point crossover. It serves to counteract the median filtering effect and is found to result in better convergence rate. The reproduction process is iterated until the cost function converges to a minimum value.

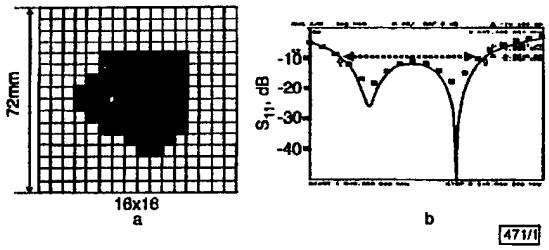

Fig. 1 *Schematic diagram and return loss of GA-optimised microstrip antenna*

a GA-optimised microstrip antenna using 16 × 16 resolution within 72 × 72mm area
Grey pixels are metal and white dot shows position of probe feed
b Return loss of antenna
— simulation
□ measurement

Results: Fig. 1*a* shows the shape of the GA-optimised microstrip. A 72 × 72mm square design area in which the metallic patch can reside is discretised into a 16 × 16 grid for the chromosome definition. The thickness of the FR-4 substrate (dielectric constant of 4.3) is 1.6mm. In the GA-optimised shape, the grey pixels are metal and the white pixels have no metal. The white dot shows the position of the probe feed. To experimentally verify the GA design, we have built and measured such a microstrip patch. Fig. 1*b* shows the return loss comparison between the measurement and simulation results. The solid line is the measurement result taken from an HP8753C network analyser. The square dots represent the simulation result. Good agreement can be observed between the measurement and simulation. The graph shows a bandwidth of 6.16% by simulation and 6.18% by measurement. This is about three times that of a square microstrip antenna (36 × 36mm), which has a bandwidth of 1.98%. Further improvements in the bandwidth can be obtained from the GA by increasing the grid resolution from 16 × 16 to 32 × 32. Figs. 2*a* and *b* show, respectively, the GA-optimised patch shape and the bandwidth performance in the higher resolution design. The bandwidth is found to be 8.04% by simulation and 8.10% by measurement. This is about four times that of a square microstrip antenna.

Finally, the operating principle of the GA-optimised shape is interpreted. It is clear from the two frequency dips in Fig. 2*b* that the antenna contains two operating modes that are very closely spaced in frequency. We have verified the two modes by examining the current distributions on the patch at 1.99 and 2.07GHz. In addition to the dualmode principle, another important bandwidth enhancement effect is achieved through the ragged edge shape. We have found that when the patch is restricted to singlemode operation (by imposing symmetry constraints), the introduction of ragged edges in the GA-optimised shape can enhance the bandwidth by ~30%. Therefore, the GA-optimised design combines both the dualmode operation and ragged edge shape to achieve the broadest bandwidth.

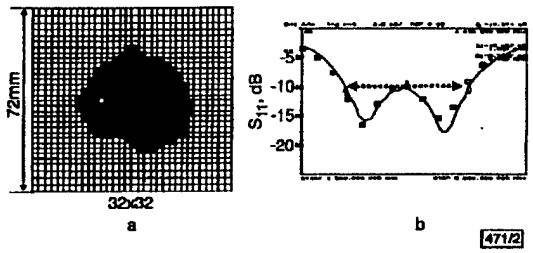

Fig. 2 *Schematic diagram and return loss of GA-optimised microstrip antenna*

a GA-optimised microstrip antenna using 32 × 32 resolution within 72 × 72mm area
Grey pixels are metal and white dot shows position of probe feed
b Return loss of antenna
— simulation
□ measurement

Conclusions: Optimised patch shapes for microstrip antennas on thin FR-4 substrate have been investigated using the genetic algorithm. The optimised shape shows a fourfold improvement in bandwidth when contrasted with a standard square microstrip antenna. This result has been verified by laboratory measurement. The basic operating principle of the optimised shape can be explained in terms of a combination of dualmode operation and ragged edge shape.

Acknowledgments: This work is supported by the Office of Naval Research under Contract No. N00014-98-1-0178, the Air Force MURI Center for Computational Electromagnetics under Contract No. AFOSR F49620-96-1-0025, and the Texas Higher Education Coordinating Board under the Texas Advanced Technology Program.

© IEE 2000
25 September 2000
Electronics Letters Online No: 20001452
DOI: 10.1049/el:20001452

H. Choo, A. Hutani and H. Ling (*Department of Electrical and Computer Engineering, The University of Texas at Austin, Austin, TX 78712-1024, USA*)

E-mail: ling@ece.utexas.edu

L.C. Trintinalia (*Department of Telecommunications and Control Engineering, Escola Politécnica da Universidade de São Paulo, São Paulo, Brazil*)

References

1 JAMES, J.R., and HALL, P.S.: 'Handbook of microstrip antennas' (Peter Peregrinus, London, 1989), Vol. 1
2 JOHNSON, J.M., and RAHMAT-SAMII, Y.: 'Genetic algorithms and method of moments (GA/MOM) for the design of integrated antennas', *IEEE Trans. Antennas Propag.*, 1999, **47**, pp. 1606–1614
3 VILLEGAS, M., and PICON, O.: 'Creation of new shapes for resonant microstrip structures by means of genetic algorithms', *Electron. Lett.*, 1997, **33**, pp. 1509–1510
4 TRINTINALIA, L.C.: 'Electromagnetic scattering from frequency selective surfaces'. MSc Thesis, Escola Politécnica da Univ. de São Paulo, Brazil, 1992
5 CWIK, T., and MITTRA, R.: 'Scattering from a periodic array of free-standing arbitrarily shaped perfectly conducting or resistive patches', *IEEE Trans. Antennas Propag.*, 1987, **35**, pp. 1226–1234

Paper [15]

ON MODELING MUTUAL COUPLING IN ANTENNA ARRAYS USING THE COUPLING MATRIX

Tao Su[1] and Hao Ling[1]
[1] Department of Electrical and Computer Engineering
University of Texas at Austin
Austin, Texas 78712-1084

Received 28 August 2000

ABSTRACT: *The coupling matrix is a standard way to represent the mutual-coupling effect between elements in an antenna array. In this paper, two commonly used approaches to determine the coupling matrix are examined, and their limitations are discussed. The coupling matrix obtained from the minimum mean-square error matching of the active and stand-alone element patterns is shown to be more effective than the mutual-impedance approach. The coupling-matrix model is also extended for more complex antenna arrays, and an example is provided to illustrate the effectiveness of the extended model.* © 2001 John Wiley & Sons, Inc. Microwave Opt Technol Lett 28: 231–237, 2001.

Key words: *array mutual coupling; coupling matrix; active element patterns*

I. INTRODUCTION

It is well known that the radiation/receiving pattern of an antenna element situated in an array environment can be quite different from its stand-alone pattern due to mutual-coupling effects. The antenna element pattern in the array environment is called the active element pattern in the antenna community [1]. In applications such as direction finding, the active element patterns of the array elements are needed to carry out direction-of-arrival estimation. If the stand-alone element patterns are used instead of the active element patterns, significant degradation can result in array performance [2].

To properly account for the mutual-coupling effect and for simplicity, it is customary to express the active element patterns as the product of a coupling matrix and the stand-alone element patterns. Although the coupling-matrix concept is widely utilized for array signal processing, two very different approaches have been adopted in the literature to interpret and determine the coupling matrix. The first approach comes out of the antenna community. Gupta and Ksienski [3] first derived the coupling matrix from a microwave network point of view. The array is viewed as a multiport network, and it is shown that the coupling matrix can be simply related to the generalized impedance matrix of the multiport network. Since the generalized impedance matrix is an intrinsic property of the antenna structure, such a derivation of the coupling matrix is quite attractive from the fundamental electromagnetics point of view. This approach has been utilized and extended in a number of antenna mutual-coupling studies [4–6].

The second approach originated from the array signal-processing community. Friedlander and Weiss [7] first proposed a method for direction finding based on the coupling-matrix model. In their view, the coupling matrix is simply an averaged effect of the angular-dependent relationship between the active element patterns and the stand-alone element patterns. Based on this assumption, various array calibration procedures have been developed in which the coupling matrix is determined by minimum mean-square error (MMSE) matching of the two sets of patterns at a few known incident angles [8, 9].

While both of these approaches have been used with success on arrays consisting of simple dipole elements, the assumptions used in their derivation and the limitations of each approach have not been examined in detail in the literature. In this paper, we set out to compare the two different approaches for determining the coupling matrix. We first review the two approaches, and discuss the limitations of each approach in Section II. In Section III, numerical results are generated using the standard numerical electromagnetic solver NEC [9] to verify our observations. In Section IV, we show that the coupling-matrix model can be further extended for more complex antenna arrays, and an example is provided to illustrate the effectiveness of the extended model.

II. MUTUAL-COUPLING MODELS

Assume that an array with N elements is located in the xy-plane, and receives a plane wave incident from angle ϕ in the azimuth plane. Let us consider a matrix relationship between the active element patterns and the stand-alone element patterns as

$$\mathbf{A}_{true}(\phi) = \mathbf{M}\mathbf{A}_{theo}(\phi) \tag{1}$$

where $\mathbf{A}_{true}$ and $\mathbf{A}_{theo}$ are the active and stand-alone element patterns, respectively, and $\mathbf{M}$ is the mutual coupling matrix. $\mathbf{A}_{theo}$ has N rows, with each row containing the stand-alone element pattern for a particular element in the array. For the ith row, it can be represented as

$$a_i(\phi) = f_i(\phi)e^{jk(x_i\cos\phi + y_i\sin\phi)} \tag{2}$$

where $f_i(\phi)$ is the stand-alone element response as a function of ϕ, and the exponential term is the explicit position-dependent phase delay for the ith element located at (x_i, y_i). The stand-alone pattern matrix of the array is then defined as

$$\mathbf{A}_{theo}(\phi) = [a_1(\phi)\ a_2(\phi)\ \cdots\ a_N(\phi)]^T. \tag{3}$$

The active pattern matrix $\mathbf{A}_{true}$ has the same structure as $\mathbf{A}_{theo}$, except that $a_i(\phi)$ is replaced by the active element pattern of the ith element. The two different approaches in determining the mutual coupling matrix $\mathbf{M}$ are discussed below.

Contract grant sponsor: Office of Naval Research
Contract grant number: N00014-98-1-0178
Contract grant sponsor: Texas Higher Education Coordinating Board under the Texas Advanced Technology Program

A. The Z Approach. In the first approach, the antenna array with N elements is viewed as an N-port microwave network [3]. The relationship between the antenna terminal voltages and currents on reception under a plane-wave excitation can be written as

$$\begin{aligned} V_1 &= Z_{11}I_1 + \cdots + Z_{1i}I_i + \cdots + Z_{1N}I_N + V_{1,oc} \\ &\vdots \quad \vdots \qquad \vdots \qquad \vdots \quad \vdots \\ V_i &= Z_{i1}I_1 + \cdots + Z_{ii}I_i + \cdots + Z_{iN}I_N + V_{i,oc} \\ &\vdots \quad \vdots \qquad \vdots \qquad \vdots \quad \vdots \\ V_N &= Z_{N1}I_1 + \cdots + Z_{Ni}I_i + \cdots + Z_{NN}I_N + V_{N,oc}. \end{aligned} \quad (4)$$

In the above expression, $V_{i,oc}$ is the received voltage at the ith port when all of the antenna terminals are open circuited, and Z_{ij} is the mutual impedance between the ith and the jth port defined as $Z_{ij} = V_i/I_j|_{I_k=0,\, k\neq j}$. If we assume that each antenna is loaded by load impedance Z_{iL} at its terminals and use the relationship $V_i = -Z_{iL}I_i$, we can express the terminal voltages in the following matrix form:

$$\begin{bmatrix} 1+\frac{Z_{11}}{Z_{1L}} & \cdots & \frac{Z_{1i}}{Z_{iL}} & \cdots & \frac{Z_{1N}}{Z_{NL}} \\ \vdots & \ddots & \vdots & \ddots & \vdots \\ \frac{Z_{i1}}{Z_{1L}} & \cdots & 1+\frac{Z_{ii}}{Z_{iL}} & \cdots & \frac{Z_{iN}}{Z_{NL}} \\ \vdots & \ddots & \vdots & \ddots & \vdots \\ \frac{Z_{N1}}{Z_{1L}} & \cdots & \frac{Z_{Ni}}{Z_{iL}} & \cdots & 1+\frac{Z_{NN}}{Z_{NL}} \end{bmatrix} \begin{bmatrix} V_1 \\ \vdots \\ V_i \\ \vdots \\ V_N \end{bmatrix} = \begin{bmatrix} V_{1,oc} \\ \vdots \\ V_{i,oc} \\ \vdots \\ V_{N,oc} \end{bmatrix}$$

or

$$\mathbf{ZV} = \mathbf{V}_{oc}. \quad (5)$$

Note that, if we stack columnwise the received voltage vectors $\mathbf{V}$ obtained for different plane-wave incident angles, the resulting matrix is, in fact, the active pattern matrix $\mathbf{A}_{true}$ in Eq. (1) (apart from an unimportant scaling factor). Similarly, if we stack the open circuit voltage vectors $\mathbf{V}_{oc}$ and assume that they are the same as the voltages received under stand-alone conditions, the resulting matrix is the stand-alone pattern matrix $\mathbf{A}_{theo}$. Therefore, the mutual coupling matrix in (1) can be written as

$$\mathbf{M} = \mathbf{Z}^{-1}. \quad (6)$$

This completes the derivation of $\mathbf{M}$ under the $\mathbf{Z}$ approach.

Since the normalized impedance $\mathbf{Z}$ is intrinsic to the structure and is completely independent of angle, $\mathbf{M}$ is also angle independent. This is a highly desirable conclusion. However, it hinges on the assumption that the received voltage at the terminals of an antenna when all of the antenna elements are open circuited is the same as the received voltage when all of the other elements are absent. From the electromagnetic point of view, this is clearly not true as the induced currents on the antenna elements will not be identically zero under the open-circuit condition. As a result, the total voltage developed at the antenna terminals is not only due to the incident field, but also to fields produced by the induced currents on other elements. Therefore, while Eq. (5) is always true, the coupling matrix $\mathbf{M}$ given by (6) does not rigorously relate the active and stand-alone element patterns. Under certain situations, however, this model may work approximately. For example, if we consider an array comprised of half-wave dipole elements, the induced currents on every element should be very small under the open-circuit condition, and the $\mathbf{Z}$ approach may be quite adequate. This will be examined numerically in Section III.

B. The C Approach. In the second approach, the mutual-coupling matrix is viewed as an average of the angular-dependent relationship between the active and stand-alone element patterns [7]. Under this assumption, $\mathbf{M}$ can be obtained by using the MMSE matching between the two patterns at a number of incident angles:

$$\mathbf{M} = \mathbf{C} = \mathbf{A}_{true}\mathbf{A}_{theo}^{H}(\mathbf{A}_{theo}\mathbf{A}_{theo}^{H})^{-1}. \quad (7)$$

We refer to the above formulation as the C approach.

The effectiveness of the C approach will now be examined from the induced current point of view based on the method of moments (MoM). In MoM, the integral equation of the induced currents on all of the antennas in the array can be written in a matrix form as follows:

$$\mathbf{LI} = \mathbf{V} \quad (8)$$

where $\mathbf{I}$ is the current, $\mathbf{V}$ is the incident plane-wave excitation, and $\mathbf{L}$ is the moment matrix. Suppose that we remove all but the ith antenna in the array; we can find the stand-alone current distribution on the ith antenna by solving a smaller moment system described by

$$\mathbf{L}_i^0\mathbf{I}_i^0 = \mathbf{V}_i. \quad (9)$$

N such systems can be written for all of the elements in the array. Since the right-hand side is determined by the incident field only, it does not change whether the antenna is stand-alone or in the array environment. Thus, we rewrite Eq. (8) as

$$[\mathbf{L}]\begin{bmatrix} \mathbf{I}_1 \\ \vdots \\ \mathbf{I}_N \end{bmatrix} = \begin{bmatrix} \mathbf{L}_i^0 & & \mathbf{0} \\ & \ddots & \\ \mathbf{0} & & \mathbf{L}_N^0 \end{bmatrix}\begin{bmatrix} \mathbf{I}_1^0 \\ \vdots \\ \mathbf{I}_N^0 \end{bmatrix}$$

or

$$\mathbf{LI} = \mathbf{L}^0\mathbf{I}^0. \quad (10)$$

By solving (10), the actual current distribution is related to the stand-alone current by

$$\mathbf{I} = \mathbf{L}^{-1}\mathbf{L}^0\mathbf{I}^0. \quad (11)$$

Next, we try to extract the currents at the terminals of the antenna elements from the $\mathbf{I}$ vector, and stack them over all of the incident angles to arrive at the active pattern matrix $\mathbf{A}_{true}$. Similarly, we try to extract the terminal currents from the $\mathbf{I}^0$ vector, and stack them to form the stand-alone pattern matrix $\mathbf{A}_{theo}$. First, we sift out the terminal currents from $\mathbf{I}$

and the corresponding rows from the matrix $(\mathbf{L}^{-1}\mathbf{L}^0)$ in (11) to form

$$\mathbf{I}_{\text{term}} = (\mathbf{L}^{-1}\mathbf{L}^0)|_{\text{term}}\mathbf{I}^0 \tag{12}$$

where the subscript "term" indicates the rows corresponding to the antenna terminals. Next, we sift out the terminal currents from $\mathbf{I}^0$ by writing

$$\mathbf{I}^0 = \begin{bmatrix} \mathbf{S}_1 & & \mathbf{0} \\ & \ddots & \\ \mathbf{0} & & \mathbf{S}_N \end{bmatrix} \begin{bmatrix} I^0_{1,\text{term}} \\ \vdots \\ I^0_{N,\text{term}} \end{bmatrix} \tag{13}$$

where $\mathbf{S}_i$ is the shape of the current distribution on the ith element and $I^0_{i,\text{term}}$ is its corresponding terminal current. Substituting (13) into (12), we can find the relationship between the actual and stand-alone terminal currents. Note that the moment matrices $\mathbf{L}$ and $\mathbf{L}^0$ are angular independent. If the shape of the current distribution on a stand-alone antenna element is also angular independent, then Eq. (12) can be rigorously cast into the form of (1). To summarize, we have shown that the relationship between the active element pattern and the stand-alone element pattern is angular independent provided that the shape of the current distribution on each stand-alone antenna element is independent of angle. When this condition is satisfied, the mutual-coupling matrix can be effectively determined by (7).

Let us now examine when the angular-independent current shape condition can be met. The first situation has been discussed in [5], where all of the antennas are vertical wires and the incident directions have the same elevation angle. In this case, the stand-alone current distribution of an antenna is exactly the same over all of the incident angles. A second common situation is when the antenna elements are working near resonance. In this case, the stand-alone current distribution on an antenna is dominated by the resonant mode, and thus has approximately the same shape over all of the incident angles. An example of this situation is an array of half-wave dipoles.

III. NUMERICAL EXAMPLES

In this section, we illustrate the conditions for the Z and C approaches to be valid using computer simulation. We study a linear array consists of four dipoles, whose centers are spaced 0.45 wavelength apart, as shown in Figure 1. The simulations are carried out using NEC.

In the first example, the dipoles are a half wavelength in length. All of the dipoles are loaded with 73 Ω of load impedance at the center. Elements 1 and 4 are rotated 45 and −45°, respectively, about the y-axis. Elements 2 and 3 are rotated 45 and −45°, respectively, about the x-axis. We determine the coupling matrix using both the C approach and the Z approach for this structure. The current at the center of each antenna is computed for incident angles from −90 to 90° at a step of 1°. This serves as the reference active element pattern. The values at ±75, ±45, and 0° are used to calculate the C matrix from (7). To determine the Z matrix, we first obtain the mutual admittance by short circuiting all of the antenna ports, driving the jth antenna with a voltage source, and computing $Y_{ij} = I_i/V_j|_{V_k=0,\, k\neq j}$. By inverting the resulting generalized admittance matrix, we get the mutual impedance Z_{ij}. The normalized impedance matrix Z is then obtained from (5).

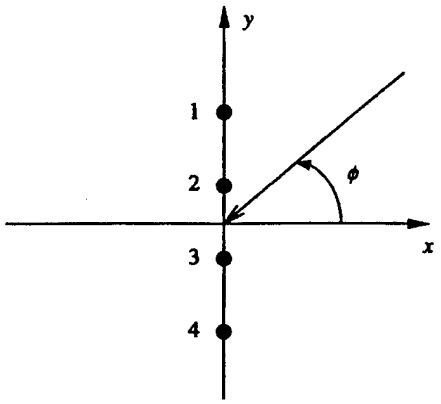

Figure 1 Array geometry

Once we obtain the two coupling matrices, we use them to calculate the active element patterns from the stand-alone element patterns. Notice that, since the elements are tilted, even the stand-alone element patterns are not isotropic. The active element patterns of antenna elements 1 and 2 are plotted in Figure 2(a) and (b), respectively. The solid curves are the active element patterns directly computed by NEC. The dashed curves are obtained using the Z approach, and the dotted lines are modeled using the C approach. We find that the dashed curves are quite close to the computed ones, but are not exactly the same. This is because the $\mathbf{V}_{oc}$ condition described in Section II-A is only approximately satisfied, even for an array of half-wave dipoles. On the other hand, the curves using the C approach match almost perfectly with the computed ones. In this case, the antennas operate in resonance, and the stand-alone current distribution has the same shape over all incident angles, even though they are not all vertically aligned.

To further observe the effectiveness of the mutual-coupling models, we apply the active element patterns to a direction-finding problem, which is quite sensitive to the element patterns. Two uncorrelated incoming signals are assumed from the incident angles of 50 and 65°. The signal-to-noise ratio (SNR) is set to 30 dB. The angles of arrival are determined using the standard MUSIC algorithm, and the resulting normalized power spectra are plotted in Figure 3. The solid curve is the result from the reference active element patterns. For comparison, the result by neglecting the mutual-coupling effect is obtained by using the stand-alone element patterns, and is plotted as the dash–dot curve. The large degradation shows the importance of taking mutual coupling into consideration. The dashed curve is the result of the Z approach. The dotted curve is obtained using the C approach. It is observed that the C approach performs almost as well as the reference active element patterns, while the Z approach leads to some degradation in the peak position and width of the power spectra.

In the second example, we replace the half-wave dipole elements with full-wave dipoles. Compared with the previous example, the $\mathbf{V}_{oc}$ condition is strongly violated for the Z approach, and the near-resonant condition is not satisfied for the C approach. Figure 4 shows the computed and modeled active element patterns. This time, neither the Z nor the C approach is close to the reference result.

Finally, we make the full-wave dipoles perpendicular to the xy-plane. Now, the vertical wire condition is satisfied for

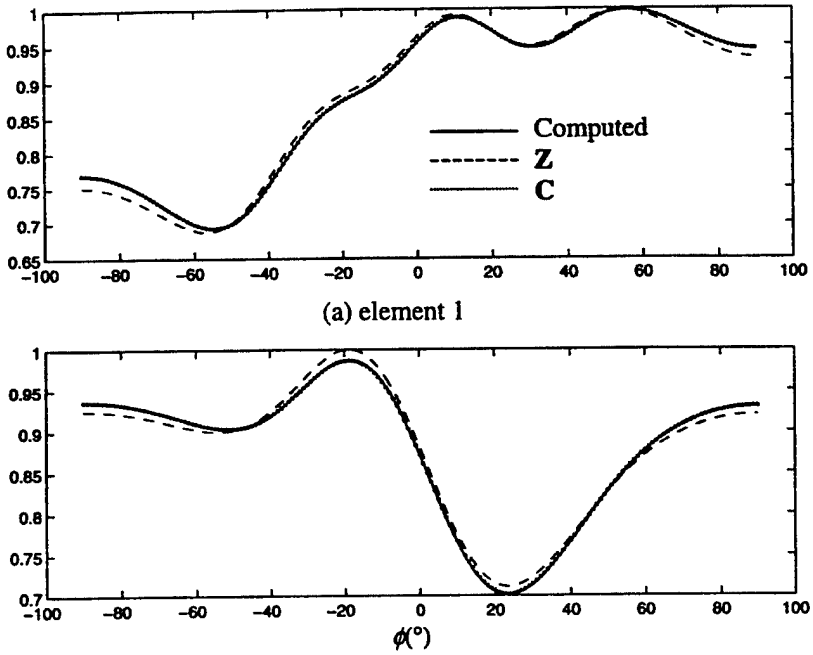

Figure 2 Computed and modeled active element patterns for array of rotated half-wave dipoles

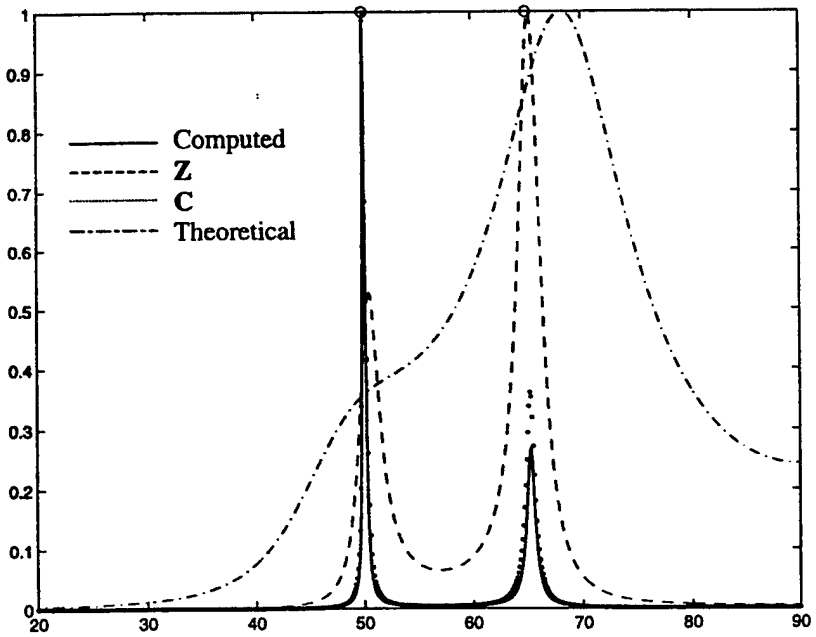

Figure 3 Direction-finding result using different element patterns

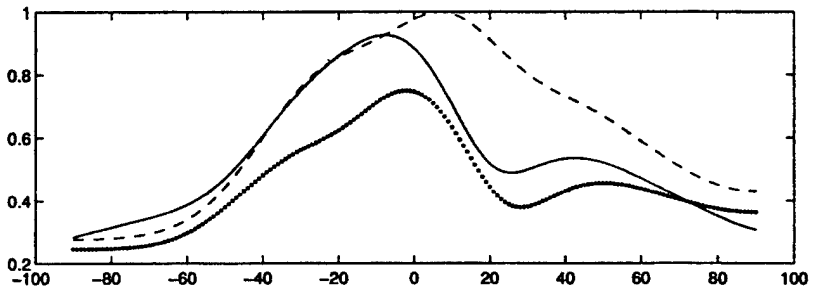

(a) element 1

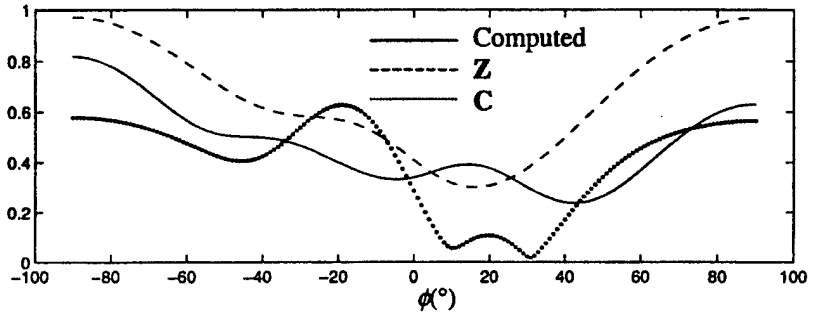

(b) element 2

Figure 4 Computed and modeled active element patterns for array of rotated full-wave dipoles

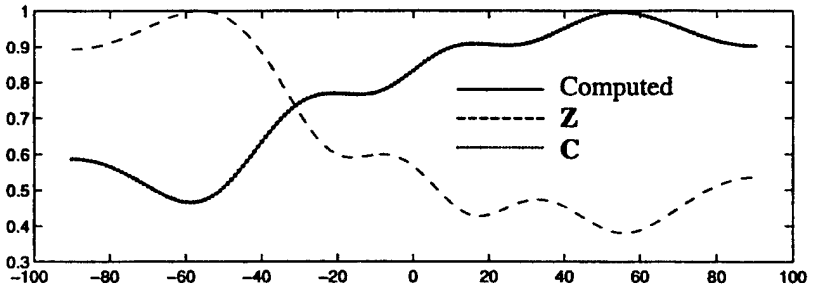

(a) element 1

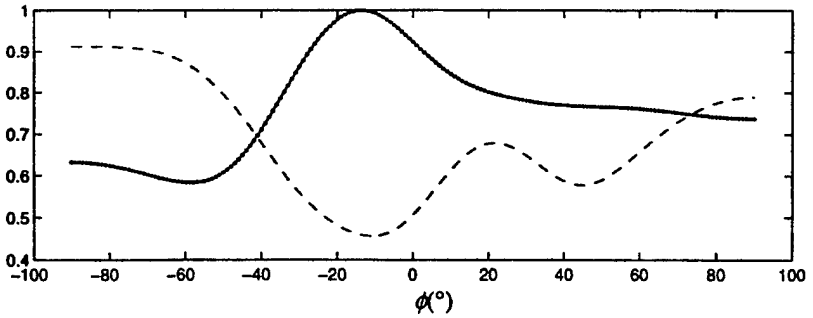

(b) element 2

Figure 5 Computed and modeled active element patterns for array of vertical full-wave dipoles

the C approach. The resulting element patterns are plotted in Figure 5. The Z approach still works poorly as in example 2. However, the C approach perfectly models the active element patterns. As discussed in Section II-B, the matching in this case is exact.

IV. EXTENSION OF THE MUTUAL-COUPLING MODEL

As can be seen in the examples, the C approach is more accurate than the Z approach. Yet, the situations when the C approach can be applied are still quite limited. The approach fails for more complex antenna structures. By observing Eq. (11), we can see that, if the array elements consist of thin wires, each piece of wire affects the active element pattern in the same manner as a dipole antenna. Thus, for certain cases, the model in (1) can be extended to include the coupling from all parts of the array. For example, if we have an array of Yagi antennas, we may include the coupling from the parasitic elements to model the active element patterns more accurately. More specifically, we extend the model as follows:

$$\mathbf{A}_{\text{true}} = [\mathbf{C} \quad \mathbf{C}'] \begin{bmatrix} \mathbf{A}_{\text{theo}} \\ \mathbf{A}'_{\text{theo}} \end{bmatrix} \tag{14}$$

where $\mathbf{A}'_{\text{theo}}$ is the stand-alone receiving patterns of the parasitic elements and $\mathbf{C}'$ describes the coupling from the parasitic elements to the driven elements. Like the standard C approach, (14) is valid if all of the parasitic elements are vertical or their lengths are close to the resonant length. The MMSE matching can again be used to determine the coupling matrix, except that the number of incident angles needed to give a unique solution is increased.

As an example, we look at an array consisting of four parallel Yagi antennas, as shown in Figure 6(a). All of the elements in the array are perpendicular to the xy-plane, and the separation between two adjacent Yagis is one wavelength. Each Yagi antenna consists of three wires, with the center wire being the driven element, as shown in Figure 6(b). The stand-alone element pattern is plotted in Figure 6(c). Next, the coupling matrix in (14) is determined from the computed

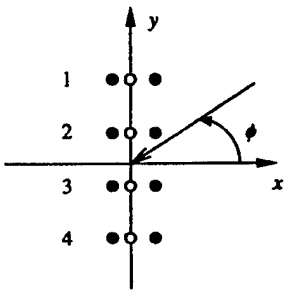

(a) Array geometry.

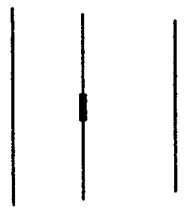

(b) Yagi element

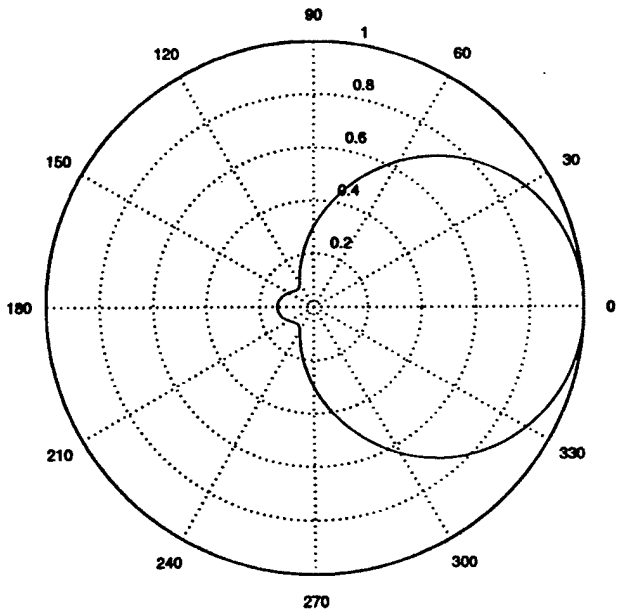

(c) Stand-alone element pattern

Figure 6 Four-element array with Yagi elements

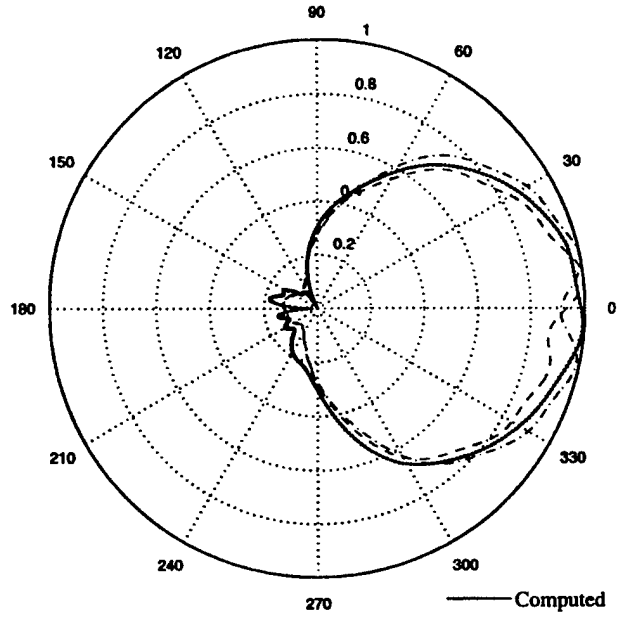

(a) element 1

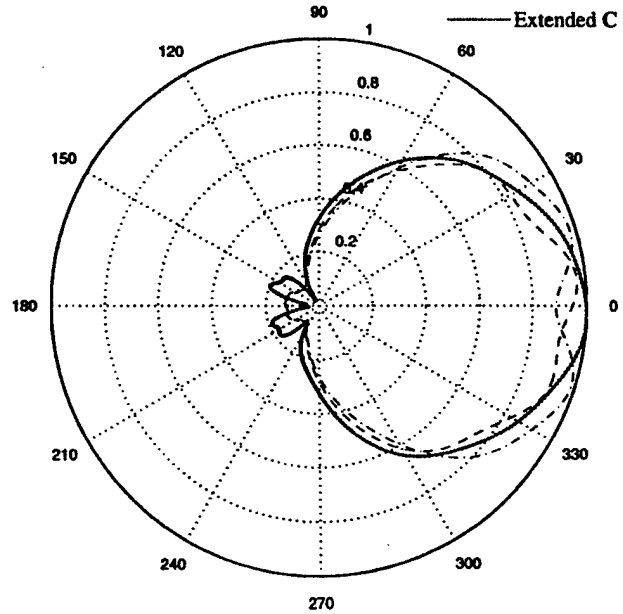

(b) element 2

Figure 7 Computed and modeled active element patterns for an array of Yagi antennas

active element patterns at 12 incident angles uniformly distributed between -180 and 180°. The reference and the modeled active element patterns of the first and second antennas are plotted in Figure 7(a) and (b), respectively. The solid curves are the reference patterns, and the dotted curves are obtained using the extended-C approach. They match with the reference patterns very well. As a comparison, we also model the active element patterns using the Z approach and the C approach. The results are shown in dashes and dash–dot curves, respectively. The agreement is obviously not as good. This is because the open-circuit voltage condition does not hold for the Z approach, and the constant current shape condition for each array element is violated for the C approach.

V. CONCLUSIONS

In this paper, the two commonly used approaches for determining the mutual-coupling matrix in array antennas have been discussed. It has been shown that the Z approach is an approximation that applies when the element pattern under the open-circuit condition can be well approximated by the stand-alone element pattern. It has also been shown that the C approach holds true whenever the current distribution of a stand-alone element has the same shape over all incident angles. This condition is satisfied for vertical wire antennas or near-resonant antennas. We have found from our numerical examples that the C approach is, in general, more accurate than the Z approach. We have also extended the C approach to model more complex wire elements by considering each wire as an individual antenna. An example of an Yagi array has been provided to demonstrate the effectiveness of the extended-C model.

REFERENCES

1. D.F. Kelley and W.L. Stutzman, Array antenna pattern modeling methods that include mutual coupling effects, IEEE Trans Antennas Propagat 41 (1993), 1625–1632.
2. T. Su, K. Dandekar and H. Ling, Simulation of mutual coupling effect in circular arrays for direction finding applications, Microwave Opt Technol Lett 26 (2000), 331–336.
3. I.J. Gupta and A.A. Ksienski, Effect of mutual coupling on the performance of adaptive arrays, IEEE Trans Antennas Propagat AP-31 (1983), 785–791.
4. T. Svantesson, Modeling and estimation of mutual coupling in a uniform linear array of dipoles, IEEE Int Conf Acoust, Speech, Signal Processing, Phoenix, AZ, 1999, pp. 2961–2964.
5. C.-C. Yeh, M.-L. Leou, and D.R. Ucci, Bearing estimations with mutual coupling present, IEEE Trans Antennas Propagat 37 (1989), 1332–1335.
6. R.S. Adve and T.K. Sarkar, Compensation for the effects of mutual coupling on direct data domain adaptive algorithms, IEEE Trans Antennas Propagat 48 (2000), 86–94.
7. B. Friedlander and A.J. Weiss, Direction finding in the presence of mutual coupling, IEEE Trans Antennas Propagat 39 (1991), 273–284.
8. C.M.S. See, A method for array calibration in parametric sensor array processing, IEEE Singapore Int Conf Commun Syst, Singapore, 1994, pp. 915–919.
9. A.N. Lemma, E.F. Deprettere, and A.J. Veen, Experimental analysis of antenna coupling for high-resolution DOA estimation algorithms, IEEE Workshop Signal Processing Advances in Wireless Commun, Annapolis, MD, May 1999, pp. 362–365.
10. NEC-2 manual, Lawrence Livermore National Lab, 1996.

© 2001 John Wiley & Sons, Inc.

J. of Electromagn. Waves and Appl., Vol. 15, No. 7, 865–883, 2001

A FREQUENCY EXTRAPOLATION TECHNIQUE FOR COMPUTING ANTENNA-PLATFORM RADIATION PROBLEMS

T. Su, Y. Wang, and H. Ling

Department of Electrical and Computer Engineering
The University of Texas at Austin
Austin, TX 78712, USA

Abstract—A frequency extrapolation technique is proposed to obtain the broad band radiation patterns of antenna-platform radiation problems. A frequency-dependent time-of-arrival model is applied to the induced current computed at low frequencies. The model parameters are estimated by applying the ESPRIT superresolution algorithm to the computed data. A pre-multiplication scheme in conjunction with the complex time-of- arrival estimation from ESPRIT is used to determine the additional frequency-dependent factors in the model. The current at high frequencies is then extrapolated based on the model and the radiated field is computed using the extrapolated current. The algorithm is applied to several 2D and 3D antenna-platform radiation problems. The extrapolated radiation patterns are found to be in good agreement with those generated by brute force computation. Since the current required for the extrapolation is only computed at lower frequencies, large savings in computation time and memory can be achieved.

1 Introduction

2 Frequency Dependent Model and Determination of Model Parameters

3 Algorithm Testing and Error Estimation Using Simulated Data

4 Numerical Results

5 Conclusions

Acknowledgment

References

1. INTRODUCTION

The numerical solution of electromagnetic scattering and radiation problems from complex structures is usually very computer intensive in time and memory, especially at high frequencies. In the standard method of moments (MoM), for example, the computation complexity scales as f^6 where f is the frequency. Even for fast solvers such as the fast multipole method [1, 2], the frequency scaling is still between f^2 and f^3. Thus it is desirable to obtain the broad band response from the computation results at only a few frequencies. This can be accomplished by fitting the computed frequency response to a reduced-order model and extracting the model parameters from the data. Approaches based on model-based parameter estimation have been studied extensively and applied to many aspects in electromagnetic computation [3–11]. The appropriate reduced-order models to parameterize the physical observables are different depending on the frequency region of interest. In the low frequency range, the rational function model is widely used, while in the high frequency range, the time-of-arrival model is the preferred choice in characterizing the ray-optical behaviors of fields and currents.

In this paper, we address the model-based frequency extrapolation of antenna-platform radiation problems. It is well known that the radiation patterns of antennas are strongly affected by the mounting platform. Since the simulation of such radiation problems is very costly to generate as a function of frequency, we set out to extrapolate the high frequency response from computed data at lower frequencies. Our approach entails fitting the computed current at low frequencies to a time-of-arrival model and estimating the model parameters by the superresolution algorithm ESPRIT [12]. Previously, this approach has been applied to radar signature prediction with good success [10]. In that work, the coefficients of the time-of-arrival model were assumed to be frequency independent. In the radiation problem, the primary radiation from the antenna is usually frequency dependent. Furthermore, when there exist higher-order multiple interactions on the platform, the amplitude of each mechanism is in general also frequency dependent [13–17]. Thus a more accurate model is needed to parameterize the current. Here we generalize the extrapolation algorithm by using a frequency-dependent time-of-arrival model. To extract the additional frequency dependence in this model, we adopt an approach similar to the one proposed in [15], which was developed to effectively extract the frequency dependency of the scattering mechanisms in measured backscattered data. Our results show that the radiation pattern can be accurately extrapolated based on the

frequency dependent model.

This paper is organized as follows. Section 2 describes the frequency-dependent time-of-arrival model and the procedure to determine the model parameters. Section 3 gives a numerical example of the extrapolation algorithm using simulated data. The performance of the algorithm in the presence of noise is investigated and the errors in the estimation of model parameters are quantified. In Section 4 we apply the algorithm to extrapolate the induced current in antenna-platform radiation problems. The radiation patterns predicted at high frequencies are compared against the reference MoM computation in both 2D and 3D platforms. Conclusions are given in Section 5.

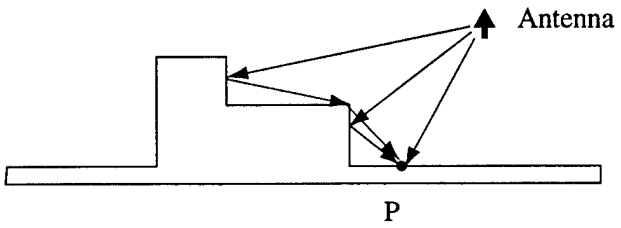

Figure 1. Time-of-arrival model for the induced current at point P accounts for the direct incident radiation from the antenna and the multiple scattered waves from other parts of the platform.

2. FREQUENCY DEPENDENT MODEL AND DETERMINATION OF MODEL PARAMETERS

We postulate that the current induced on a complex platform due to illumination from a primary source can be well described by a time-of-arrival model at high frequencies. The different time-of-arrival terms correspond to the different incident wave mechanisms from both the direct antenna radiation and higher-order scattering from other parts of the platform, as illustrated in Fig. 1. Therefore, the current at an arbitrary point P on the platform can be expressed as:

$$J(\omega) = \sum_n a_n e^{-j\omega t_n} \tag{1}$$

where t_n is the arrival time of the nth incident wave and a_n is its amplitude. In [10], a_n was assumed to be independent of frequency. However, in the antenna-platform radiation problem, the primary radiation from the antenna is in general frequency dependent. For

instance, the radiation strength of a dipole antenna is proportional to the ω (or $\omega^{1/2}$ for a line source in 2D problems). Furthermore, for complex platforms, the incident waves to a specific current element can come from the scattered fields from other parts of the platform. These secondary incident fields are also frequency dependent. For canonical shapes, their exact frequency dependencies are predicted by the geometrical theory of diffraction (GTD), and are in the form of ω^{α} where α is the frequency factor. For example, the strength of the scattered field from corner diffraction has a frequency dependency of ω^{-1}, and that from edge diffraction has a frequency dependency of $\omega^{-1/2}$. Therefore, the time-of-arrival model can be improved by incorporating the frequency factor:

$$J(\omega) = \sum_n a_n \omega^{\alpha_n} e^{-j\omega t_n} \tag{2}$$

where α_n, is the frequency factor for each incident wave. Compared with (1), this model is better matched to the actual physics of the radiation and scattering mechanisms.

Since we are attempting to extrapolate the frequency response to a much broader range, the accurate estimation of the frequency factors is critical. A small error in α will result in dramatic difference in amplitude at frequencies in the extrapolated region. However, the existing superresolution algorithms based on eigenspace decomposition (e.g., ESPRIT and MUSIC) apply only to signals in the form of (1). For instance, the ESPRIT algorithm [12] estimates (a_n, t_n) from uniformly sampled current data from ω_1, to ω_M based on the data model:

$$J(\omega_m) = \sum_n a_n e^{-j\omega_m t_n} + n(\omega_m), \qquad \omega_m = \omega_1, \omega_2, \ldots, \omega_M \tag{3}$$

where n denotes additive Gaussian white noise. This model can be easily extended to estimate complex time-of-arrivals via analytic continuation. If we separate the real and imaginary part of t_n the resulting model can be written as

$$J(\omega) = \sum_n a_n e^{\omega \mathrm{Im}(\tilde{t}_n)} e^{-j\omega \mathrm{Re}(\tilde{t}_n)} \tag{4}$$

where the tilda symbol is used to indicate a complex number. This is the well-known complex exponential model and has been used to approximately model the frequency dependence in a_n [13]. Comparing (4) to the frequency-dependent time-of-arrival model (2), we find that the only difference between the two is the frequency dependency, which is in the form of ω^{α} in (2) and $e^{\omega \mathrm{Im}(\tilde{t}_n)}$ in (4). For a narrow band signal,

(4) is usually a good approximation of (2), and can be simply used to model the frequency dependence within this band. However, in order to achieve accurate extrapolation results, the complex exponential model is a poor choice since it is not properly matched to the underlying physics.

To better determine the frequency factor α_n, we adopt an approach similar to the one proposed in [15] based on a pre-multiplication concept. We multiply the data by an assumed frequency factor $\omega^{-\alpha_m}$. The data model then becomes

$$\hat{J}(\omega) = \omega^{-\alpha_m} J(\omega) = \sum_n a_n \omega^{(\alpha_n - \alpha_m)} e^{-j\omega t_n} \tag{5}$$

Next, we apply ESPRIT and the complex exponential model on $\hat{J}(\omega)$ to estimate the real and imaginary parts of $\tilde{t}_n$. Note that if the frequency dependence of the pre-multiplier is exactly matched to that of a particular mechanism, the resulting exponential term will have no frequency dependence. Consequently, the estimated complex time-of-arrival term will have a zero imaginary part. Therefore, by repeatedly pre-multiplying the signal using different values of α_m and observing the imaginary parts of the resulting $\tilde{t}_n$, we can detect the correct frequency dependence α_n whenever $\mathrm{Im}(\tilde{t}_n)$ goes to zero. The implicit assumption of this approach is that the mismatched terms will not significantly distort the estimation of $\mathrm{Im}(\tilde{t}_n)$ of the matched term. This is usually true when the arrival times $\mathrm{Re}(\tilde{t}_n)$ are well separated. When two or more of the arrival times are very close to each other, this algorithm becomes less accurate due to the interference between the exponential terms. The imaginary part of $\tilde{t}_n$ may not vanish even when the corresponding frequency factor is matched by the pre-multiplication. Quantitative evaluation of the resulting error will be discussed in detail in the next section. Once α_n and t_n are estimated, the amplitude a_n can be easily found by the standard least squares procedure.

3. ALGORITHM TESTING AND ERROR ESTIMATION USING SIMULATED DATA

To test the extrapolation algorithm, we consider the signal

$$J(\omega) = (1 + 0.4j)\omega^{-1/2} e^{-j2.8\omega} + (4.3 - 2.2j)\omega^{1/2} e^{-j1.3\omega} + n, \quad \omega = 5, 6, \ldots, 35 \tag{6}$$

where n is additive Gaussian white noise. The signal-to-noise ratio (SNR) is set to 10 dB. We now use a two-term time-of-arrival model

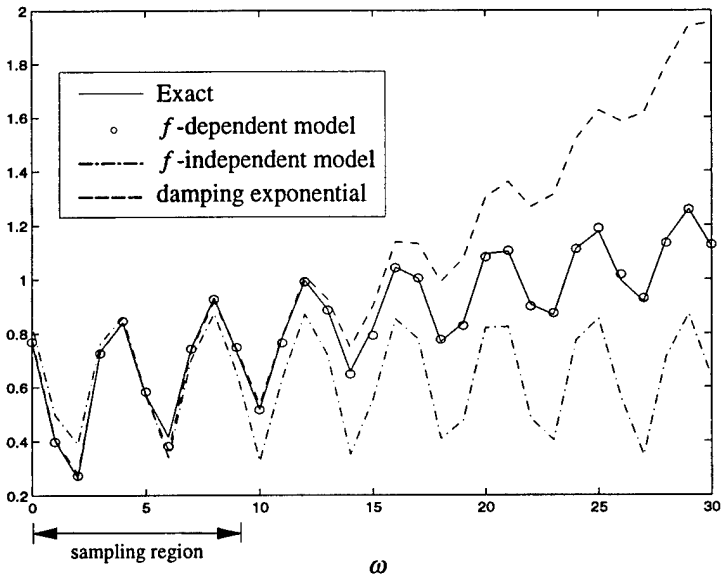

Figure 2. Extrapolation of a simulated signal using different models.

to extrapolate the signal based on its first 10 samples. The actual signal is plotted as the solid line in Fig. 2. The extrapolation results of three different models are plotted. The frequency independent model, which is plotted in dashed dot, is obtained by the model in (1) with real time-of-arrival t_n determined by ESPRIT. This model matches badly with the original curve, even in the sampled region. The complex exponential model, plotted in dashed line, uses the model in (4) with complex $\tilde{t}_n$. The resulting curve is in good agreement with the actual signal within the sampled region, but not in the extrapolated region. This indicates that although the model (4) can be a very good approximation to the actual signal in the sampled region, it cannot be used to accurately extrapolate the signal because it does not have the correct frequency dependency. The frequency-dependent time-of-arrival model, which is plotted in dots, matches the best with the original signal in both the sampled region and the extrapolated region. Its parameters are estimated using the method described in Section 2.

To show the detail workings of the pre-multiplier procedure, the imaginary parts of t_n corresponding to the two terms in (6) are plotted as functions of α_m in Figs. 3(a) and 3(b) at the SNR levels of ∞ and 10 dB, respectively. The two curves cross zero at the corresponding frequency factor of -0.5 and 0.5. It can be observed that the shapes

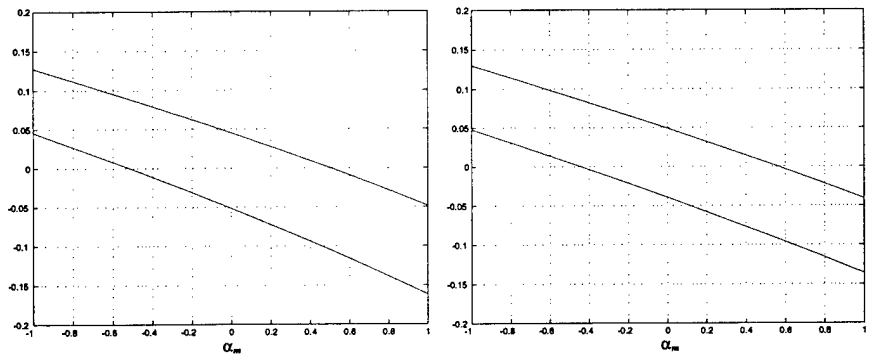

(a) SNR= ∞ (b) SNR = 10 dB

Figure 3. Variation of $\mathrm{Im}(t_n)$ as a function of the pre-multiplication factor α_m for the simulated signal at two different SNR levels.

of the curves change when the SNR is decreased, especially for the term with smaller power ($\alpha_n = -0.5$). However, the positions of the zero-crossing points vary only weakly as the SNR is decreased.

Next, we examine the error performance of the extrapolation algorithm through numerical simulation. Among the three sets of model parameters a_n, α_n and t_n the time-of-arrival t_n is directly estimated by the ESPRIT algorithm. When frequency dependent mechanisms are present in the signal, the estimation error in t_n is expected to be larger due to the interference between the exponential terms, especially when two or more arrival times are very close to each other. In this example, we estimate the arrival times in a simulated signal consisting of two frequency dependent exponential terms using ESPRIT. As a comparison, we also determine the arrival times in a two-term frequency independent signal. In both signals, the power of the stronger term is five times that of the weaker term. For the frequency dependent signal, the two frequency factors are set to 0.5 and -0.5 for the stronger and weaker terms, respectively. The test is performed 1000 times subject to random noise. In Fig. 4(a), the root mean squared (RMS) error on the time-of-arrival estimate of the weaker term is plotted as a function of the separation between the two arrival times and for different SNR conditions. The dashed lines are the estimation errors from the frequency independent signal, while the solid lines are the errors from the frequency dependent signal. Both axes are calibrated in terms of the Fourier resolution, which is the reciprocal of the available data bandwidth. It is shown that the arrival time error is larger for the frequency dependent signal, especially when the SNR is high. However, the degradation is not too severe overall.

Good estimation (with error less than 0.1 Fourier bin) is still achievable for signal separation well within one Fourier bin.

The RMS error of estimating the frequency factor an of the weaker signal is plotted in Fig. 4(b) for the frequency dependent signals used in the above test. We observe that the error decreases as the separation between the exponential terms increases and as the SNR increases, similar to the trends in Fig. 4(a). When the two arrival times are close, the interaction between the two terms results in error on the estimation of α_n and the error is strongly affected by the noise level. We can further decrease the error by imposing the constraint that the frequency factors are integer multiples of 1/2, as dictated by GTD. This is implemented when we deal with actual electromagnetic data in the next section.

Finally we look at the extrapolation error of the entire frequency-dependent time-of-arrival model. An extrapolation ratio of 3 to 1 is used in the example, i.e., the frequency response is extrapolated to three times the original bandwidth. The percentage RMS error is plotted in Fig. 4(c). When the separation between the two terms is large, the extrapolation error behaves similar to the errors of t_n and α_n. When the two terms become too close in time, we note that the error curves actually reach a maximum and then drop off. This is because below this point, the two exponential terms are too close to be resolved within the extrapolation region of interest. For larger extrapolation bandwidth, the position of the peak should move toward zero.

4. NUMERICAL RESULTS

We now apply the frequency extrapolation technique to computation data from antenna-platform radiation problems. In the first example, a two-dimensional structure shown in Fig. 5 is considered. The platform is 14 m in length and 3 m in height. The antenna is a horizontal line source placed at 5 m above the platform. The induced current on the platform is computed from 0.1 to 0.5 GHz at 21 frequency points using 2D MoM. The current is extrapolated to 1.3 GHz and radiated field is then computed based on the extrapolated current. Both the frequency-independent and frequency-dependent time-of-arrival models are used to perform the extrapolation, and the resulting radiated fields at the observation angle of $\theta = 40°$ are plotted in Figs. 6(a) and 6(b), respectively. Also plotted is the reference MoM results obtained via brute force computation. The primary radiation of the dipole antenna is not included in the plots so that we can better observe the secondary radiation from the platform. It is obvious

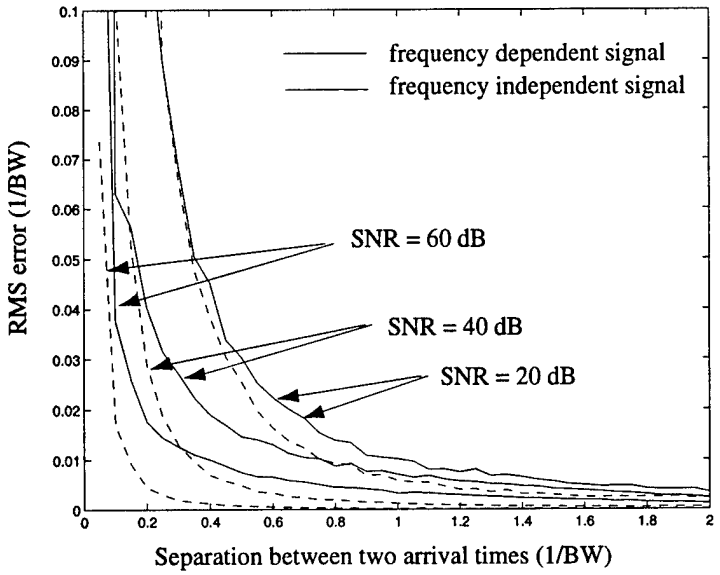

(a) RMS error in estimating the time-of-arrival t_n using ESPRIT.

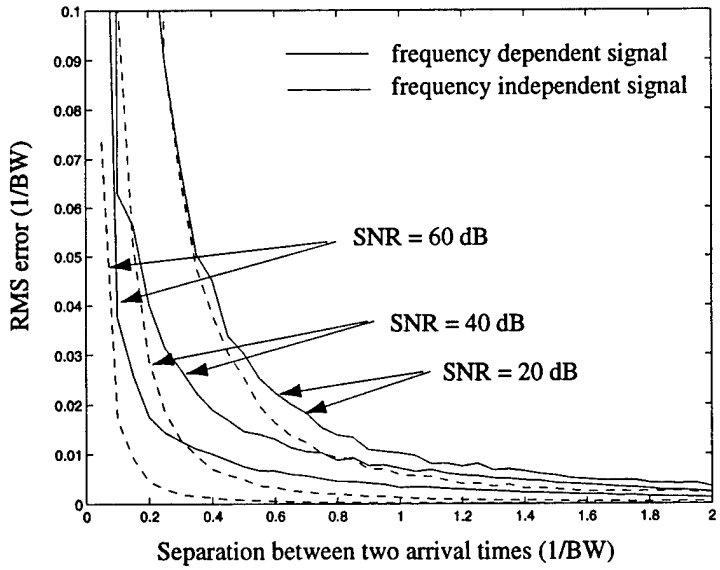

(b) RMS error in estimating the frequency factor α_n.

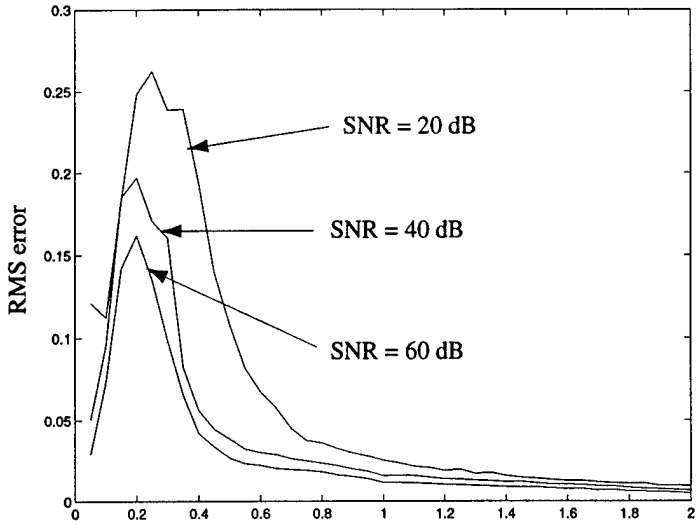

(c) Percentage RMS error of the extrapolated signal at the extrapolation ratio of 3:1.

Figure 4. Error performance of the extrapolation algorithm as a function of the separation between two arrival times at different SNR levels.

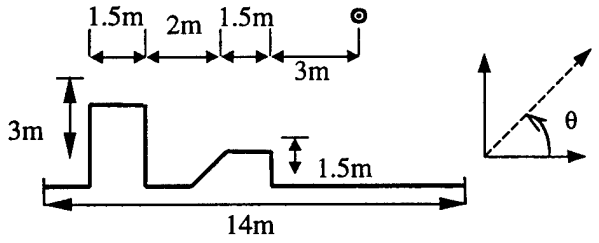

Figure 5. 2D platform geometry.

that the frequency dependency in the field response is not captured by the frequency-independent time-of-arrival model, while the field predicted by the frequency dependent model is in good agreement with the computed result. The time domain response corresponding to Fig. 6(b) is plotted in Fig. 6(c). It is shown that the time-domain peaks are well characterized by the extrapolated field. Finally, the

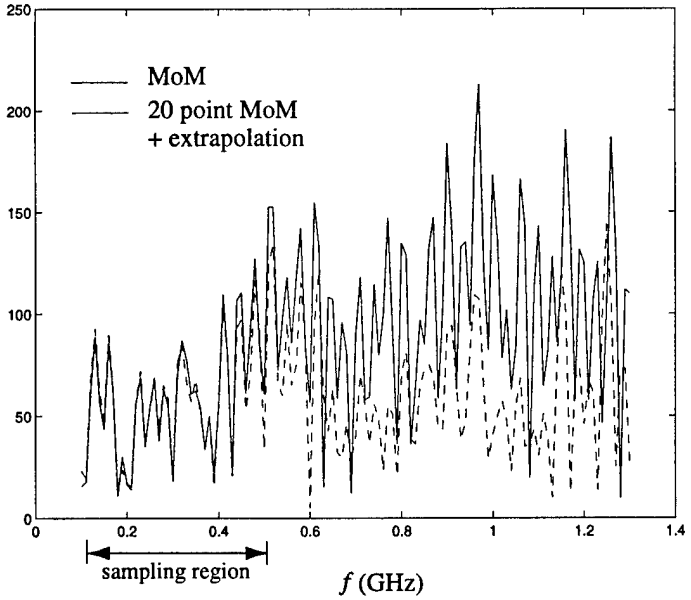

(a) Frequency response predicted by the frequency-independent time-of-arrival model at $\theta = 40°$.

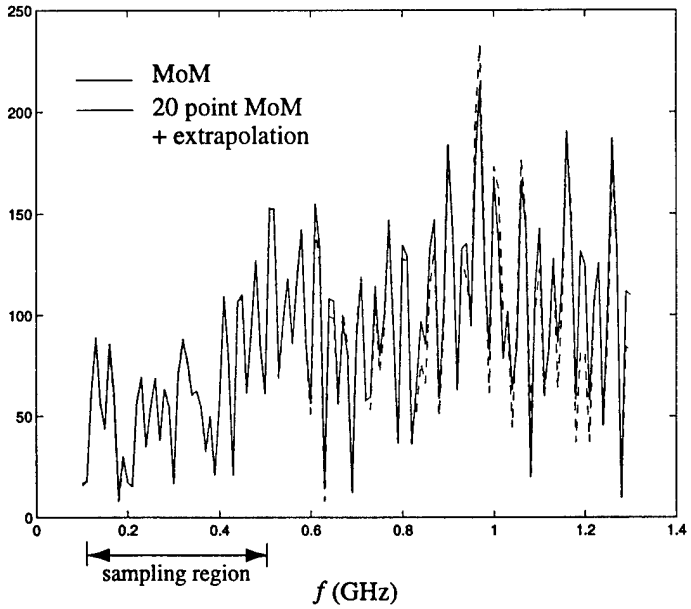

(b) Frequency response predicted by the frequency dependent model at $\theta = 40°$.

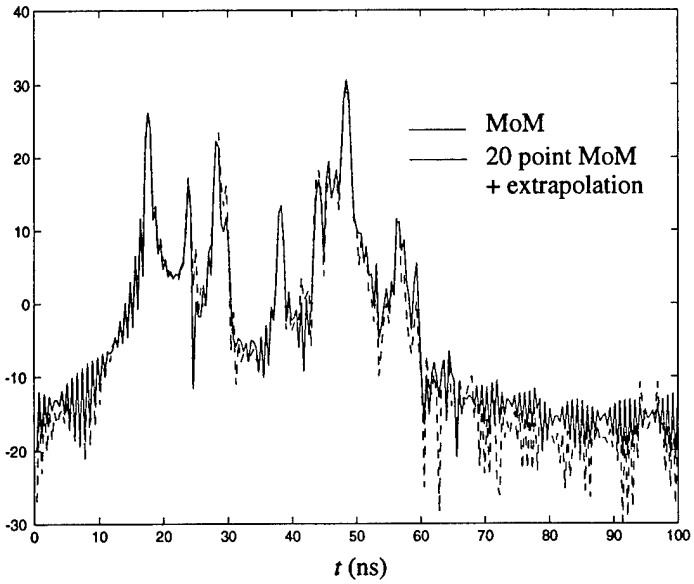

(c) Time domain response predicted by the frequency dependent model.

Figure 6. Frequency extrapolation example for the 2D platform.

radiation patterns obtained through brute force MoM computation and frequency extrapolation are plotted as functions of frequency and observation angles in Figs. 7(a) and 7(b), respectively. Very good agreement is observed between the two figures. For a quantitative comparison, the correlation index between the two figures is computed using the definition

$$R = \frac{\iint E_1^*(f,\theta)E_2(f,\theta)df\,d\theta}{\frac{1}{2}\iint \left(|E_1(f,\theta)|^2 + |E_2(f,\theta)|^2\right) df\,d\theta} \tag{7}$$

where E_1 and E_2 are the radiated fields in linear scale obtained by extrapolation and MoM computation, respectively. The correlation index between the two figures is 0.9992 in the sampled region and 0.9857 in the extrapolated region. As expected, the correlation is lower in the extrapolated region. However, the drop off is relatively small.

Next, we look at a 3D platform shown in Fig. 8. The antenna is a horizontal dipole oriented in the x direction. The induced current is computed from 0.1 to 0.36 GHz at 13 frequencies and extrapolated to

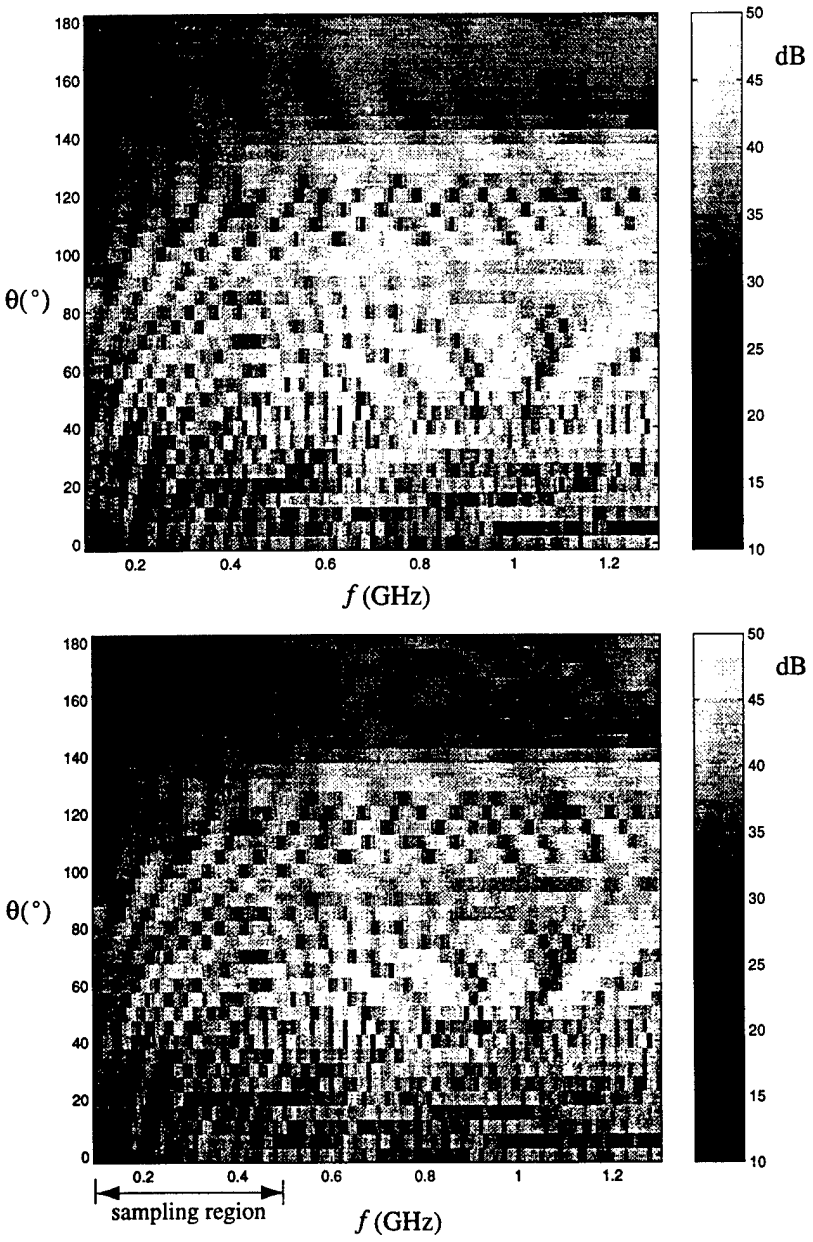

Figure 7. Comparison of the radiated field generated from brute force MoM computation and frequency extrapolation as a function of frequency and observation angle.

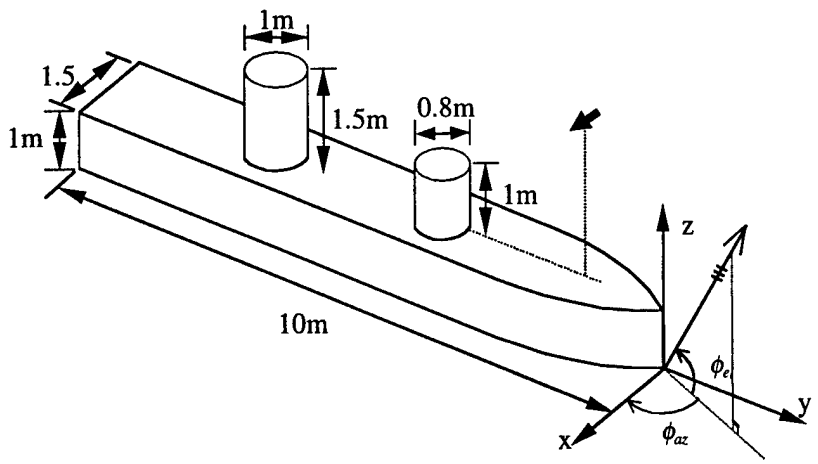

Figure 8. 3D platform geometry.

0.7 GHz. The computation is carried out using FISC [18], which is a 3D MoM code based on the fast multipole method. The extrapolated frequency and time domain responses at the observation angle $\phi_{el} = 30°$, $\phi_{az} = -60°$ are plotted in Figs. 9(a) and 9(b), respectively. Also plotted for comparison are the reference responses computed by FISC via brute force. The major radiation features are captured in both domains by the extrapolation. In the time domain response, we observe that the amplitudes of some of the weaker peaks are not correctly predicted by the extrapolation, although their arrival times are estimated quite accurately. We believe this is due to the estimation error of α_n in the current parameterization, as we expect larger errors in the frequency factors for the weaker time-of-arrival terms. Figs. 10(a) and 10(b) show the reference and extrapolated radiation patterns as functions of frequency and azimuth angle when the elevation angle is fixed at 50°. Good qualitative agreement is observed. The correlation index between the two figures is found to be 0.9980 in the sampled region and 0.9742 in the extrapolated region, respectively. This result is a little worse than the 2D example because the noise level of the FISC-computed current is higher than that of the 2D MoM code. As was shown in the last section, the extrapolation performance is affected by the SNR in the computed data. The computation time of the brute force reference results is about 50 hours on a PentiumII 400 MHz PC, while the total computation time to carry out the EM computation in the sampled region and the extrapolation process is 7 hours.

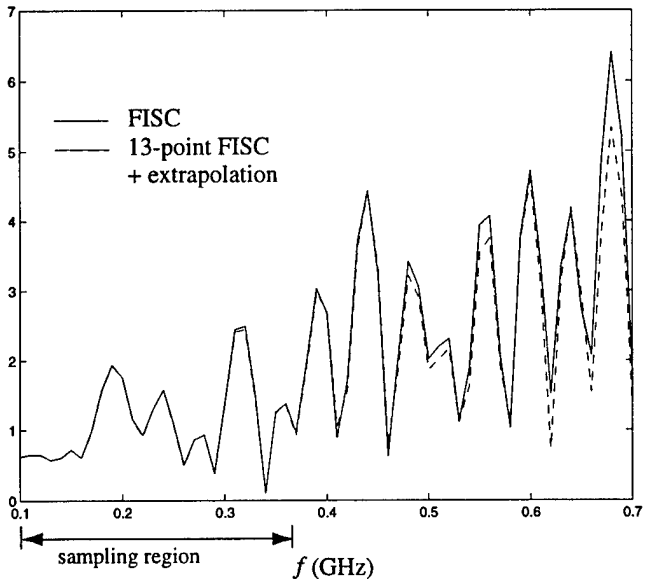

(a) Frequency response predicted by the frequency dependent model at $\phi_{el} = 30°$, $\phi_{az} = -60°$.

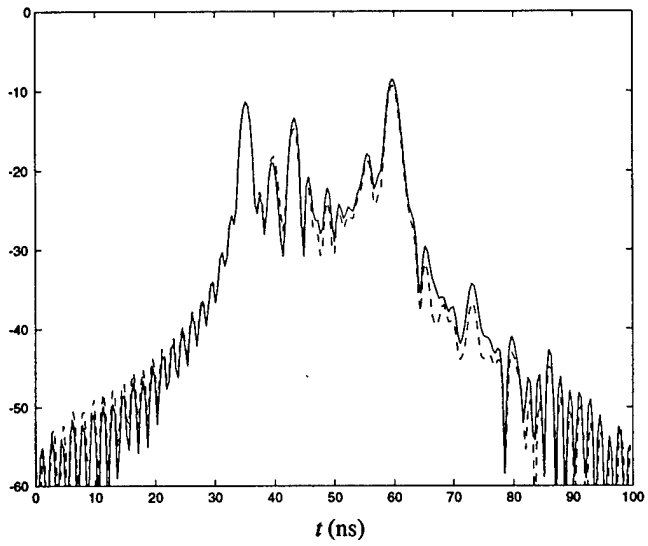

(b) Time domain response predicted by the frequency dependent model.

Figure 9. Frequency extrapolation example for the 3D platform.

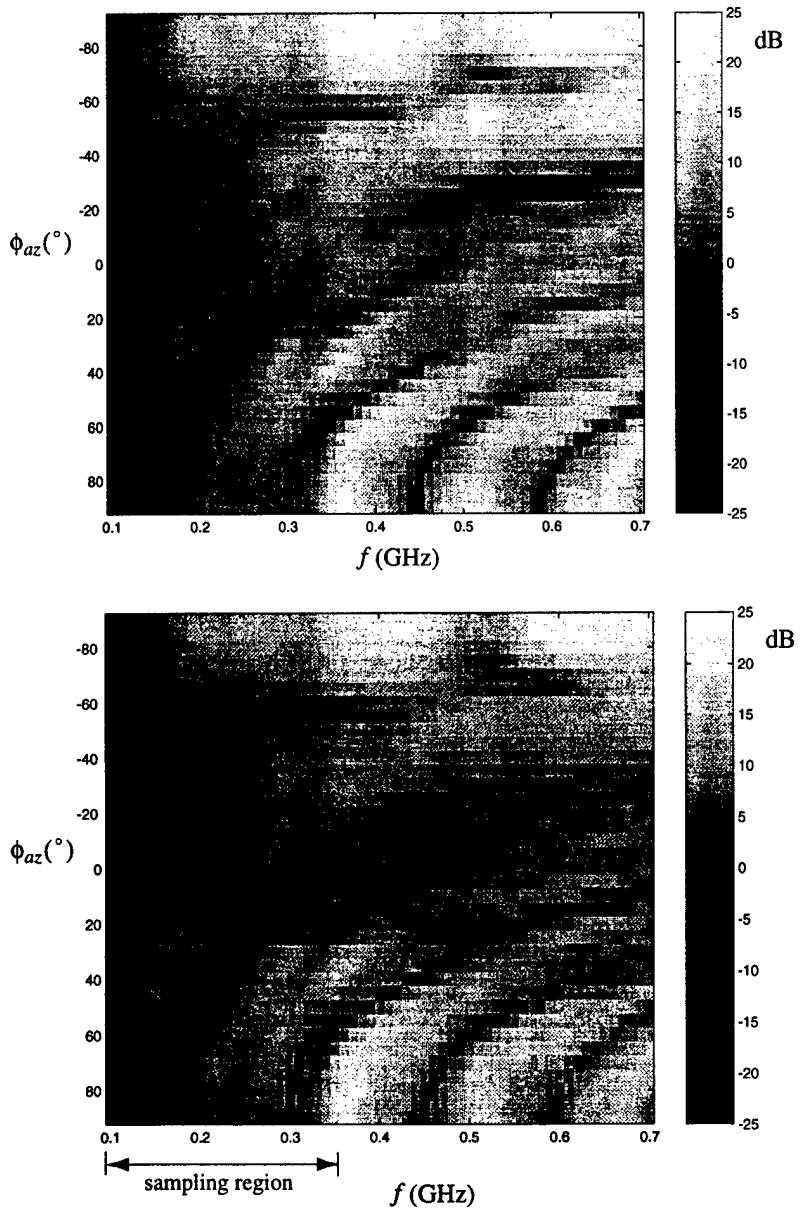

Figure 10. Comparison of the radiated field generated from brute force FISC computation and frequency extrapolation as a function of frequency and azimuth angle at the elevation angle of $\phi_{el} = 50°$.

5. CONCLUSIONS

In this paper, the frequency-dependent time-of-arrival model has been applied to extrapolate the induced current and radiation pattern in antenna-platform radiation problems. The model parameters are estimated by applying the ESPRIT superresolution algorithm to the computed data. A pre-multiplication scheme in conjunction with the complex time-of-arrival estimation from ESPRIT is used to determine the additional frequency-dependent factors. The performance of the algorithm in the presence of noise has been evaluated based on simulated data and errors in the estimation of model parameters have been quantified. Our results show that the method is quite robust. The algorithm has been applied to extrapolate the induced currents and radiation patterns in both 2D and 3D antenna-platform radiation problems. The radiation patterns computed from the extrapolated currents have been found to be in good agreement with those generated by brute force computation.

Although the determination of model parameters is more complicated, the frequency dependent model show significant performance improvement over the frequency independent model. This is due to the improved modeling of the scattering physics. Since the current required for the extrapolation is only computed at lower frequencies, large savings in computation time and memory can be achieved.

ACKNOWLEGMENT

This work is supported by the Office of Naval Research under Contract No. N00014-98-1-0178, and in part by the Air Force MURI Center for Computational Electromagnetics under contract AFOSR F49620-96-1-0025.

REFERENCES

1. Coifman, R., V. Rokhlin, and S. Wandzura, "The fast multipole method for the wave equation: a pedestrian prescription," *IEEE Antennas Propagat. Mag.*, Vol. 35, 7–12, June 993.
2. Song, J., C. C. Lu, and W. C. Chew, "Multilevel fast multipole algorithm for electromagnetic scattering by large complex objects," *IEEE Trans. Antennas Propagat.*, Vol. 45, No. 10, 1488–1493, Oct. 1997.
3. Miller, E. K., "Model-based parameter estimation in electromagnetics: part I. background and theoretical development," *Ap-*

plied Computational Electromagnetics Society Newsletter, Vol. 10, No. 3, Nov. 1995.

4. Miller, E. K., "Model-based parameter estimation in electromagnetics: part II. applications to EM observables," *Applied Computational Electromagnetics Society Newsletter,* Vol. 11, No. 2, 35–56, Feb. 1996.
5. Miller, E. K., "Model-based parameter estimation in electromagnetics: part III. Application to EM integral equations," *Applied Computational Electromagnetics Society Newsletter,* Vol. 10, No. 3, 9–29, Nov. 1995.
6. Kottapalli, K., T. K. Sarkar, Y. Hua, E. K. Miller, and G. J. Burke, "Accurate computation of wide-band response of electromagnetic systems utilizing narrow-band information," *IEEE Trans. Microwave Theory Tech.,* Vol. 39, 682–687, Apr. 1991.
7. Adve, R. S. and T. K. Sarkar, "Generation of accurate broadband information from narrowband data using the Cauchy method," *Microwave Opt. Tech Lett.,* Vol. 6, No. 10, Aug. 1993.
8. Altman, Z. and R. Mittra, "Combining an extrapolation technique with the method of moments for solving large scattering problems involving bodies of revolution," *IEEE Trans. Antennas Propagat.,* Vol. 44, 548–553, Apr. 1996.
9. Reddy, C. J., M. D. Deshpande, C. R. Cockrell, and F. B. Beck, "Fast RCS computation over a frequency band using method of moments in conjunction with asymptotic waveform evaluation technique," *IEEE Trans. Antennas Propagat.,* Vol. 46, No. 8, 1229–1233, Aug. 1998.
10. Wang, Y. and H. Ling, "Radar signature prediction using moment method codes via a frequency extrapolation technique," *IEEE Trans. Antennas Propagat.,* Vol. 47, 1008–1015, June 1999.
11. Su, T., Y. Wang, and H. Ling, "Model-based frequency extrapolation of antenna radiation characteristics on complex platforms," *Proceedings of the 15th Annual Symposium of the Applied Computational Electromagnetics Society,* 272–277, Monterey, Mar. 1999.
12. Roy, R., A. Paulraj, and T. Kailath, "ESPRIT — A subspace rotation approach to estimation of parameters of cisoids in noise," *IEEE Trans. Acoust., Speech, Signal Processing,* Vol. ASSP-34, 1340–1342, Oct. 1986.
13. Hurst, M. P. and R. Mittra, "Scattering center analysis via Prony's method," *IEEE Trans. Antennas Propagat.,* Vol. AP-35, 986–988, Aug. 1987.

14. Carriere, R. and R. L. Moses, "High resolution radar target modeling using a modified Prony estimator," *IEEE Trans. Antennas Propagat.*, Vol. 40, 13–18, Jan. 1992.
15. Moghaddar, A., Y. Ogawa, and E. K. Walton, "Estimating the time-delay and frequency decay parameter of scattering components using a modified MUSIC algorithm," *IEEE Trans. Antennas Propagat.*, Vol. 42, 1412–1418, Oct. 1994.
16. Potter, L. C., D. Chiang, R. Carriere, and M. J. Gerry, "A GTD-based parametric model for radar scattering," *IEEE Trans. Antennas Propagat.*, Vol. 43, 1058–1067, Oct. 1995.
17. Cuomo, K. M., J. E. Piou, and J. T. Mayhan, "Ultrawide-band coherent processing," *IEEE Trans. Antennas Propagat.*, Vol. 47, 1094–1107, June 1999.
18. User's Manual for FISC (Fast Illinois Solver Code), Center for Computational Electromagnetics, University of Illinois at Urbana-Champaign and DEMACO, Inc., IL, Jan. 1997.

Tao Su was born in Beijing, China in 1973. He received his B.S. degree in electronics engineering from Tsinghua University, Beijing, in 1996, and the M.S. degree in electrical engineering from the University of Texas at Austin in 1997. He is now working toward the Ph.D. degree in the University of Texas at Austin.

Yuanxun Wang was born in 1973. He received the B.S. degree from University of Science and Technology of China, Hefei, in 1993, and the M.S. and Ph.D. degree at the University of Texas at Austin in 1996 and 1999, respectively. Dr. Wang is now working as a post-doctoral researcher at the University of California at Los Angeles.

Hao Ling was born in Taichung, Taiwan, on September 26, 1959. He received the B.S. degrees in electrical engineering and physics from the Massachusetts Institute of Technology, Cambridge, in 1982, and the M.S. and Ph.D. degrees in electrical engineering from the University of Illinois at Urbana-Champaign, in 1983 and 1986, respectively. In September 1986, he joined the faculty of the University of Texas at Austin, and is currently a Professor of electrical and computer engineering. He participated in the Summer Visiting Faculty Program in 1987 at the Lawrence Livermore National Laboratory, CA. In 1990, he was an Air Force Summer Fellow at the Rome Air Development Center, Hanscom Air Force Base, MA.

J. of Electromagn. Waves and Appl., Vol. 15, No. 11, 1521–1537, 2001

FIRST ORDER TRIANGULAR PATCH BASIS FUNCTIONS FOR ELECTROMAGNETIC SCATTERING ANALYSIS

L. C. Trintinalia

Department of Telecommunications and Control Engineering
Escola Politécnica da Universidade de São Paulo
São Paulo, SP 05508-900, Brazil

H. Ling

Department of Electrical and Computer Engineering
The University of Texas at Austin
Austin, TX 78712, USA

Abstract—This paper analyzes a set of first order triangular patch basis functions for the method of moments (MoM) solution of electromagnetic scattering problems, and compares its performance to the traditional Rao-Wilton-Glisson (RWG) basis. These basis functions provide a faster convergence and a smoother surface current representation. It is shown that the computational complexity involved is about the same as the RWG basis, which means that existing computer codes can be adapted to use them with minimal modifications.

1 Introduction

2 Description of the Problem

3 EFIE Formulation

4 Numerical Results

5 Summary

References

1. INTRODUCTION

Since the introduction of the Rao-Wilton-Glisson (RWG) triangular patch basis functions [1], they have become the most widely used basis functions for solving electromagnetic scattering problems with the method of moments. These basis functions have the highly desirable property of being free of line charges while being able to model any arbitrary shape surface. For this reason they have been used by many authors [2–9]. Improvements in the original formulation such as using curvilinear triangular patches [10] and incorporating edge conditions [11] have also been reported.

Some authors [12] have pointed out that the results obtained using the RWG basis are sometimes very dependent on the triangulation scheme used. Furthermore, it is well recognized that the resulting current distribution often contains discontinuities that hinder its use for accurate current and near field prediction. Filtering scheme has been proposed to alleviate this problem [13], but leads to loss of spatial resolution. These aforementioned problems are due to the fact that the RWG basis functions cannot represent an arbitrary linear current distribution on each triangle.

In [14], Wang and Webb presented a new set of hierarchical basis functions suitable for a p-adaptation scheme from linear to higher order. They show that much better results can be obtained, for the same meshing, with second or higher order basis functions. To use these bases, however, a new code has to be written.

In this paper we present an enhanced set of triangular patch basis functions, which retain the same nice properties as the standard RWG basis, but are capable of represent any linear current distribution over each triangle. With the improvement, these basis functions are much less sensitive to the triangulation scheme and provide a much better representation of the real current distribution, leading to a faster convergence of the moment method solution. These functions are equivalent to the first order basis functions of Wang and Webb [14], but are presented here in a simpler formulation that allows existing RWG codes to be easily modified to use them.

2. DESCRIPTION OF THE PROBLEM

When we discretize a closed surface using N_f triangular patches, we obtain a set of $N_e = 2N_f/2$ edges connecting these triangles. We want to develop a set of basis functions that can represent an arbitrary linear current distribution over each triangle. For each triangle i we would

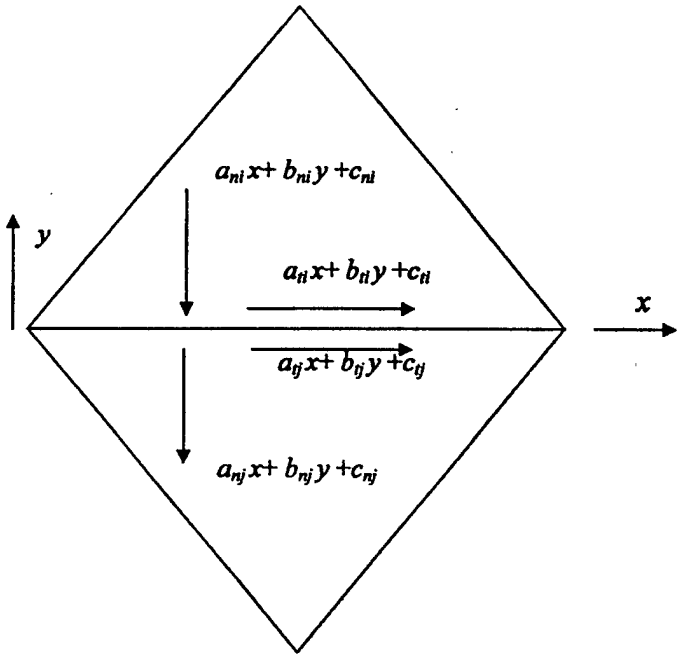

Figure 1. Linear current components of two adjacent triangles.

have a different current distribution given by:

$$\vec{J}_i(x_i, y_i) = (a_{xi}x_i + b_{xi}y_i + c_{xi})\,\hat{x}_i + (a_{yi}x_i + b_{yi}y_i + c_{yi})\,\hat{y}_i \quad (1)$$

where x_i and y_i are local coordinates in the directions tangential to the triangle i. Since we have N_f triangles, the number of degrees of freedom for this problem is equal to $6N_f$.

For electromagnetic problems we are interested only in current distributions whose components normal to the edges are continuous, to avoid the presence of artificial line charges. From Fig. 1, we see that by imposing this additional condition for each edge of our surface we are adding two constraints for each edge ($a_{ni} = a_{nj}$, $c_{ni} = n_{nj}$), thereby reducing the degrees of freedom from $6N_f$ to $3N_f$. We need, consequently, a set of $3N_f$ divergence-conforming basis functions [15] to properly solve this problem.

In [1], Rao et al propose a set of basis functions (RWG basis) having one function associated with each edge, leading therefore to a set of only $3N_f/2$ basis functions. Clearly, such set cannot represent an arbitrary linear current distribution as described earlier, i.e., it is

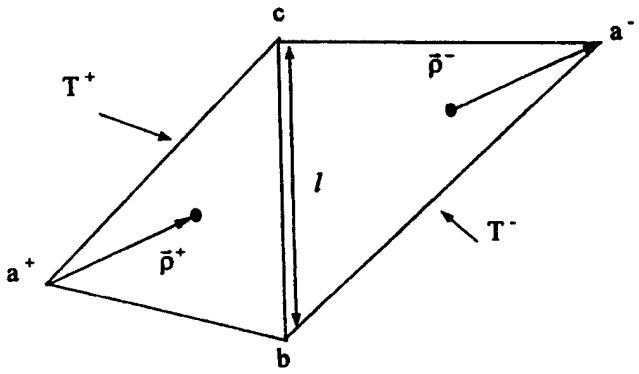

Figure 2. Triangle pair and geometrical parameters associated.

not complete in that sense. This has already been pointed out in [14] and [15].

To solve this problem we developed a new set of linear basis functions (which we shall call the first order basis) where we have two vector basis functions associated with each edge *b*-*c*, as seen in Fig. 2:

$$\vec{f}_1(\vec{r}) = \begin{cases} \dfrac{l}{(2A^+)^2} \|\vec{\rho}^+ \times \vec{\rho}_c^+\| \vec{\rho}_b^+ & \vec{r} \text{ in } T^+ \\ \dfrac{l_n}{(2A^-)^2} \|\vec{\rho}^- \times \vec{\rho}_c^-\| \vec{\rho}_b^- & \vec{r} \text{ in } T^- \end{cases}$$

$$\vec{f}_2(\vec{r}) = \begin{cases} \dfrac{l}{(2A^+)^2} \left\|\vec{\rho}^+ \times \vec{\rho}_b^+\right\| \vec{\rho}_c^+ & \vec{r} \text{ in } T^+ \\ \dfrac{l_n}{(2A^-)^2} \left\|\vec{\rho}^- \times \vec{\rho}_b^-\right\| \vec{\rho}_c^- & \vec{r} \text{ in } T^- \end{cases} \tag{2}$$

where $\vec{\rho}^+ = \vec{r} - \vec{r}_{a^+}$, $\vec{\rho}^- = \vec{r}_{a^-} - \vec{r}$ and $\vec{\rho}_{b,c}^{+,-} = \vec{r}_{b,c} - \vec{r}_{a^+,-}$. $A^\pm$ is the area of the respective triangle and "×" denotes the cross product. Each of these basis functions is parallel to one external edge and has a magnitude linearly proportional to the distance to the other external edge, as shown in Fig. 3.

The first order basis functions share the following properties with the RWG functions:

- The current has no component normal to the boundary of the surface formed by triangles T^+ and T^- (external edges).
- The component of current normal to the edge between the two triangles (internal edge) is continuous across the edge. While it

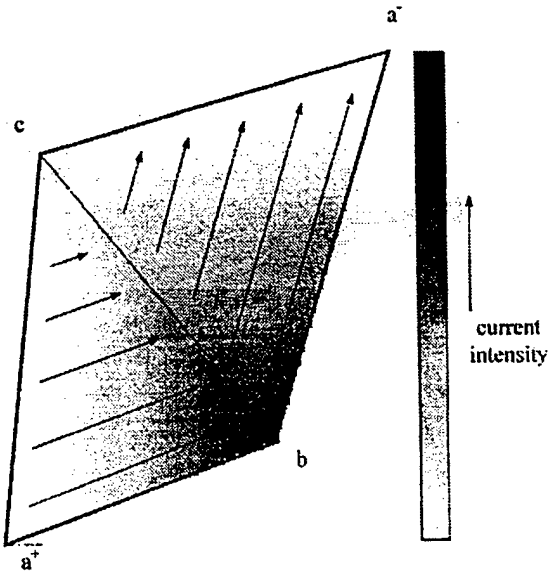

Figure 3. First order triangular patch basis function (of type 1) intensity and direction.

was a constant for the RWG basis functions, it is now a linear function, going from zero at one vertex to one at the opposite vertex.

- The surface divergence of these functions, which is proportional to the surface charge density, is constant over each triangle. The resulting surface charge density has the same magnitude but opposite signs on the two triangles.

In fact, it can be shown that an RWG basis function can be obtained by adding the two first order basis functions of equal strength for the same edge. Because of the properties described, it will be shown that the electric field integral equation (EFIE) formulation used with the RWG functions [1] can still be used, with only minor modifications for the first order basis functions.

As an example of the improvement that can be obtained with the first order basis functions, Fig. 4 shows the best representation (in the mean square sense) of a sinusoidal current on a rectangular plate that can be obtained with the RWG and the first order basis functions with the same number of triangular patches. We can see that the first order basis representation is significantly smoother and closer to the exact expression than the RWG basis.

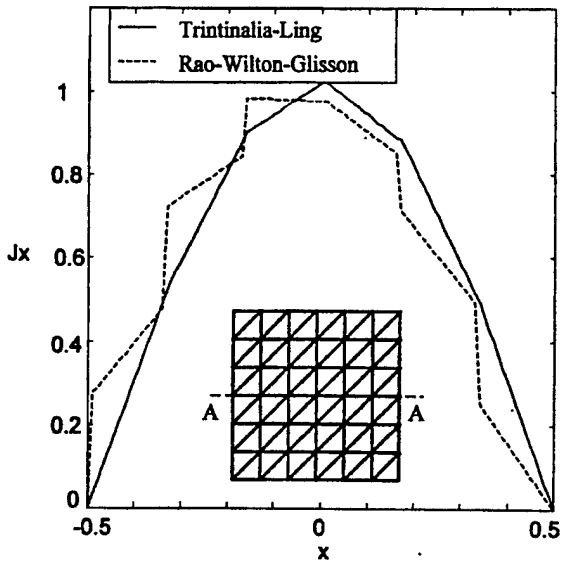
Trintinalia-Ling
Rao-Wilton-Glisson
Jx
x
A
A
1
0.8
0.6
0.4
0.2
0
-0.5
0
0.5

(a)

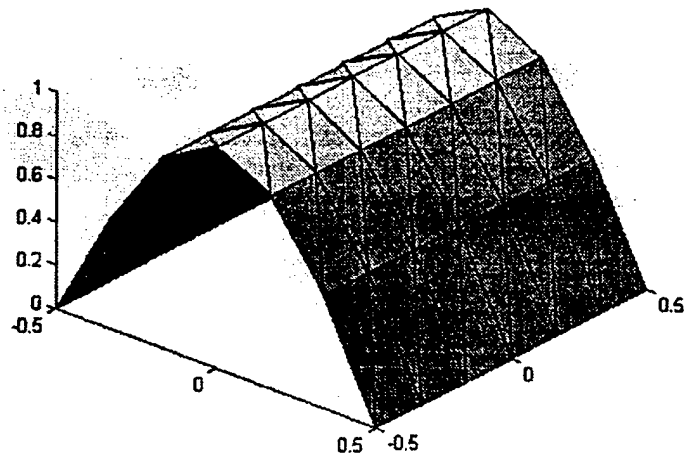
1
0.8
0.6
0.4
0.2
0
-0.5
0
0.5
0
0.5
-0.5

(b)

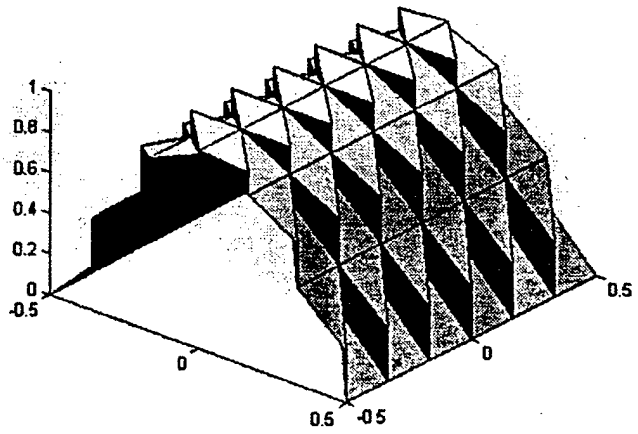

(c)

Figure 4. Sinusoidal current representation using first order basis functions (b) and the original RWG basis functions (c) over a square plate, using 72 triangular patches. Figure (a) shows the A-A′ cut of both representations.

3. EFIE FORMULATION

We will now outline the implementation of the EFIE using the first order basis. Using the standard EFIE formulation with the Galerkin method, we obtain:

$$\left\langle \vec{E}^i, \vec{f}_{m_{1,2}} \right\rangle = j\omega \left\langle \vec{A}, \vec{f}_{m_{1,2}} \right\rangle + \left\langle \nabla\Phi, \vec{f}_{m_{1,2}} \right\rangle \tag{3}$$

where $\left\langle \vec{a}, \vec{b} \right\rangle = \int_S \vec{a} \cdot \vec{b}\, dS$ and $\vec{f}_{m_{1,2}}$ denotes the basis functions in (2) at the m-th edge. As in [1], because of the properties of $\vec{f}_m$ at the edges, the last term in (3) can be rewritten as

$$\left\langle \nabla\Phi, \vec{f}_{m_{1,2}} \right\rangle = \nabla \cdot \vec{f}^{+}_{m_{1,2}} \int_{T_m^+} \Phi\, dS + \nabla \cdot \vec{f}^{-}_{m_{1,2}} \int_{T_m^-} \Phi\, dS \tag{4}$$

with

$$\nabla \cdot \vec{f}^{\pm}_{m_{1,2}} = \pm \frac{l_m}{2A^{\pm}}. \tag{5}$$

And

$$\left\langle \vec{A}, \vec{f}_{m_{1,2}} \right\rangle = \int_{T_m^+} \vec{A} \cdot \vec{f}_{m_{1,2}}\, dS + \int_{T_m^-} \vec{A} \cdot \vec{f}_{m_{1,2}}\, dS, \tag{6a}$$

$$\left\langle \vec{E}^i, \vec{f}_{m_{1,2}} \right\rangle = \int_{T_m^+} \vec{E}^i \cdot \vec{f}_{m_{1,2}}\, dS + \int_{T_m^-} \vec{E}^i \cdot \vec{f}_{m_{1,2}}\, dS. \tag{6b}$$

One difference should be noted here. While in [1] the values of the terms involving the vector potential and the incident field in (6) were approximated by their values at the centroid of the triangles, with our new set of basis/testing functions one should use a different and more precise approximation:

$$\int_{T_m^\pm} \vec{A} \cdot \vec{f}_{m_{1,2}}\, dS \cong \frac{A_m^\pm}{3} \sum_{i=1}^{3} \left(\vec{A} \cdot \vec{f}_{m_{1,2}} \right) \Big|_{\vec{r}=\vec{r}_i} \tag{7a}$$

$$\int_{T_m^\pm} \vec{E}^i \cdot \vec{f}_{m_{1,2}}\, dS \cong \frac{A_m^\pm}{3} \sum_{i=1}^{3} \left(\vec{E}^i \cdot \vec{f}_{m_{1,2}} \right) \Big|_{\vec{r}=\vec{r}_i} \tag{7b}$$

with

$$\begin{aligned} \vec{r}_1 &= \frac{2}{3}\vec{r}_a + \frac{1}{6}\vec{r}_b + \frac{1}{6}\vec{r}_c; \\ \vec{r}_2 &= \frac{1}{6}\vec{r}_a + \frac{2}{3}\vec{r}_b + \frac{1}{6}\vec{r}_c; \\ \vec{r}_3 &= \frac{1}{6}\vec{r}_a + \frac{1}{6}\vec{r}_b + \frac{2}{3}\vec{r}_c. \end{aligned} \tag{8}$$

This is necessary because we have 3 degrees of freedom for each triangle now, so we need at least 3 testing points. Moreover, this approximation leads to exact results when the vector potential or the incident field varies linearly. Similarly, the scalar potential integral in (4) can be approximated as:

$$\int_{T_m^\pm} \Phi\, dS \cong \frac{A_m^\pm}{3} \sum_{i=1}^{3} \Phi \Big|_{\vec{r}=\vec{r}_i}. \tag{9}$$

The remaining steps to derive the matrix equation are similar to those in [1]. In particular, the integrals related to the scalar and vector potential determination, after transforming to a local system of normalized area coordinates, can be written as a functions of the

integrals I^{pq}, I^{pq}_{ξ}, I^{pq}_{η} and I^{pq}_{ζ}:

$$\Phi^{pq}_{n_{1,2}} = \frac{\mp l_n}{j4\pi\omega\varepsilon} I^{pq}, \tag{10}$$

$$\begin{aligned}\vec{A}^{pq}_{n_{1,2}} &= \pm\frac{\mu l_n \vec{\rho}_{b,c}}{8\pi A^q}\left[\|(\vec{r}_{1q}-\vec{r}_{a\pm})\times\vec{\rho}_{c,b}\|\, I^{pq}_{\xi} + \|(\vec{r}_{2q}-\vec{r}_{a\pm})\times\vec{\rho}_{c,b}\|\, I^{pq}_{\eta}\right.\\ &\quad \left. + \|(\vec{r}_{3q}-\vec{r}_{a\pm})\times\vec{\rho}_{c,b}\|\, I^{pq}_{\zeta}\right] \end{aligned}\tag{11}$$

where

$$\begin{aligned} I^{pq} &= \int_0^1\int_0^{1-\eta}\frac{e^{-jkR}}{R}d\xi d\eta, \qquad I^{pq}_{\xi} = \int_0^1\int_0^{1-\eta}\xi\frac{e^{-jkR}}{R}d\xi d\eta,\\ I^{pq}_{\eta} &= \int_0^1\int_0^{1-\eta}\eta\frac{e^{-jkR}}{R}d\xi d\eta, \qquad I^{pq}_{\zeta} = I^{pq} - I^{pq}_{\xi} - I^{pq}_{\eta};\\ R &= |\vec{r}-\vec{r}\,'|, \quad \vec{r}\,'\in T^q, \quad \vec{r}\in T^p. \end{aligned}\tag{12}$$

Here, the notation $\Phi^{pq}_{n_{1,2}}$ or $\vec{A}^{pq}_{n_{1,2}}$ means the potential at a point $\vec{r}$ in the triangle p due to basis function (1 or 2) associated with edge n flowing on triangle q. The positions $\vec{r}_{1q}, \vec{r}_{2q}, \vec{r}_{3q}$ are the three vertices of triangle q (independent of n) and the other parameters are those specified in Fig. 2.

4. NUMERICAL RESULTS

In order to compare the convergence of the first order basis against the standard RWG basis we first analyzed the scattering by a perfectly conducting square plate. Fig. 5 and Fig. 6 show respectively the predicted co-polarization and cross-polarization RCS of a square plate of side 1λ at normal incidence, plotted as a function of the number of basis functions used ($3N_f/2$ for RWG and $3N_f$ for first order basis). We can see a much faster convergence with the first order basis than with the RWG basis. Note that this is so even though for the same number of bases, the triangular mesh for the RWG result is twice as dense as that used in the first order basis result.

Fig. 7 shows the current distribution on the plate obtained using a discretization of 72 triangular patches for both sets of basis functions. We observe rather abrupt variations of the current along the transversal direction for the RWG basis. For the first order basis, on the other

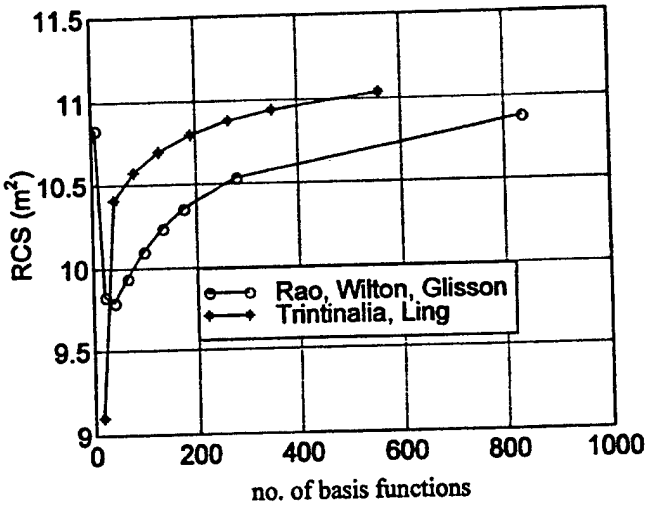

Figure 5. Predicted RCS for normal incidence at a square plate of side 1 m ($\lambda = 1m$), as a function of the number of basis functions used.

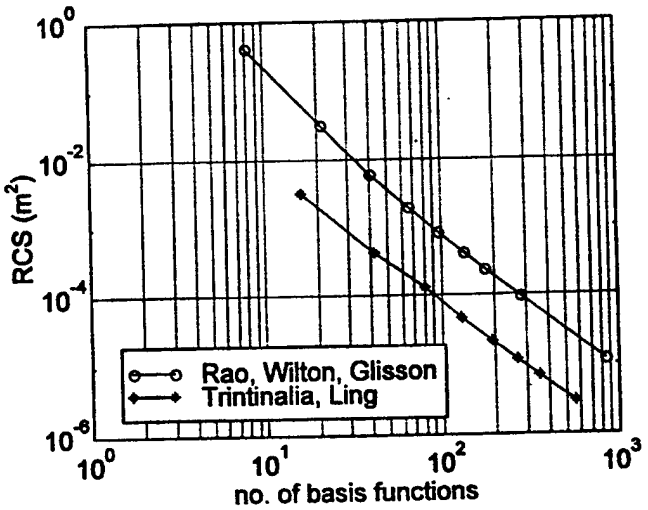

Figure 6. Predicted cross-polarization for normal incidence at a square plate of side 1λ, as a function of the number of basis functions used.

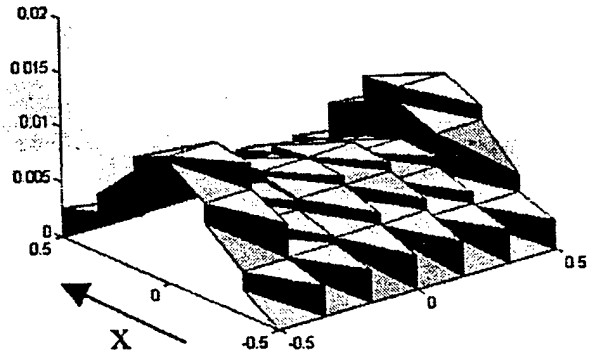

(a)

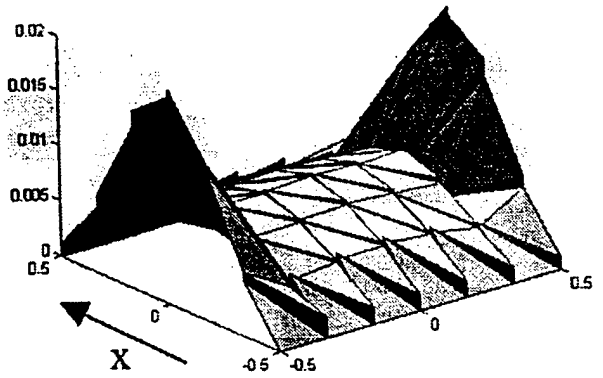

(b)

Figure 7. Magnitude of current distribution (x component) over a PEC square plate of side 1λ obtained using a 72 triangular patch discretization for (a) RWG basis functions and (b) first order basis functions.

hand, the current behavior is smoother, as expected. Also, for the first order basis solution the current distribution reaches higher values close to the edges, as it should due to the edge singularity.

As a second example we examined the scattering from a sphere. Fig. 8 shows the current distribution over a PEC sphere using a discretization of 160 triangular patches. In this figure only the real part of the θ component is shown, but similar behavior is exhibited

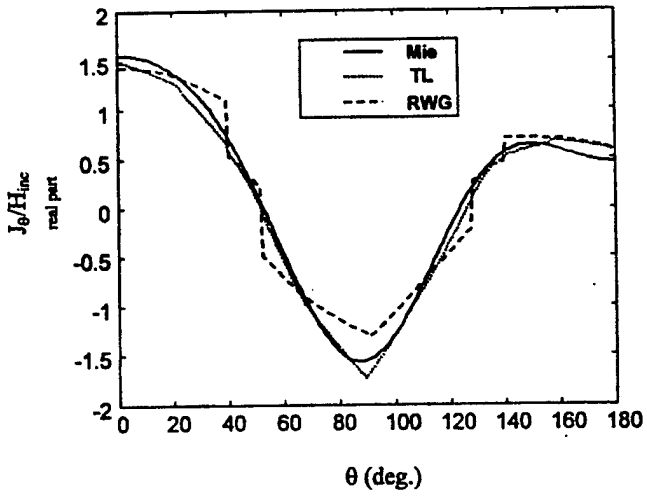

Figure 8. Current distribution (real part only) over a PEC sphere of radius $0.4\,\lambda$, obtained using a 160 triangular patch discretization for RWG basis and first order basis (TL), compared against the exact Mie's solution. The wave is incident from $\theta = 0°$.

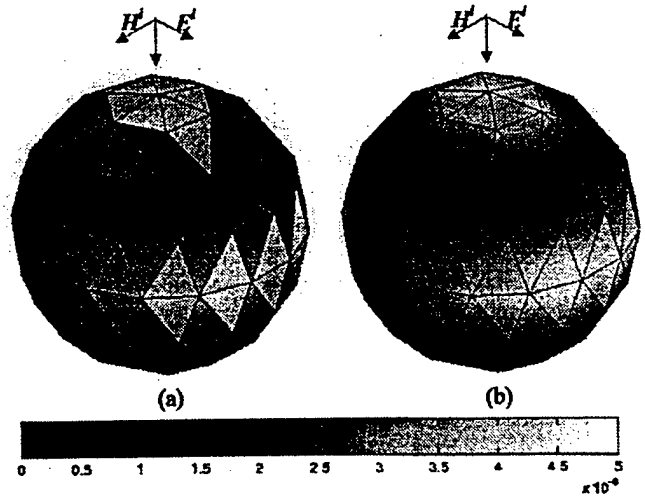

Figure 9. Real part of the total current density (vector magnitude) over a PEC sphere of radius $0.4\,\lambda$, obtained using a 160 triangular patch discretization for RWG basis functions (a) and first order basis functions (b). The wave is incident from $\theta = 0°$ (top).

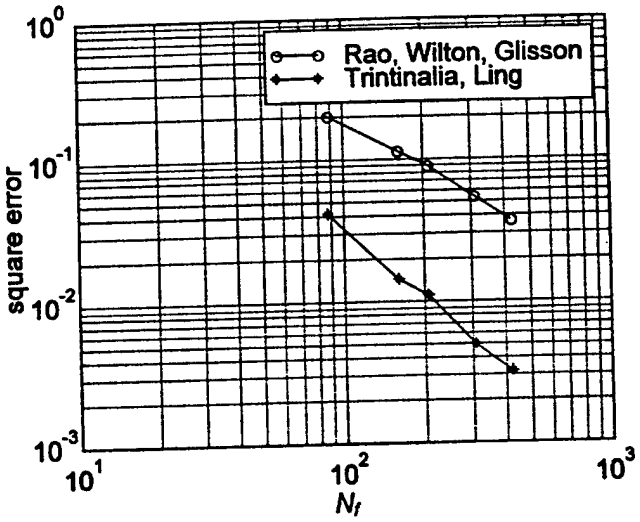

Figure 10. Mean square error in current distribution for a $0.4\,\lambda$ radius sphere, obtained using the RWG basis and the first order basis, as a function of the number of triangular patches used.

for the imaginary part as well as the other current component. We can see that the agreement with the exact Mie's solution is better for the first order basis than for the RWG basis. Fig. 9 shows the real part of the total current density on the surface of the sphere. Notice that the first order basis solution presents a much smoother behavior than the RWG one. Fig. 10 shows the total mean square error in the current distribution obtained using both formulations, as a function of the number of facets, for the same sphere problem. Here we observe again that the convergence of the first order basis solution is much faster than the RWG solution.

We also ran a frequency scan of the RCS prediction for a 0.2 m radius sphere using both bases. The results, compared against the exact Mie's solution, are shown in Fig. 11. We note that at lower frequencies (discretization $< 0.2\,\lambda$) both models provide very good agreement with the exact solution. For higher frequencies though ($d > 0.3\,\lambda$) both models start to diverge from the exact solution, but the first order basis is more stable than the RWG basis as the frequency increases.

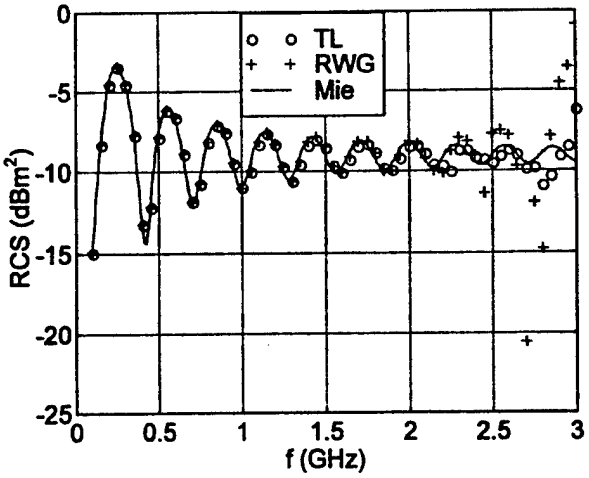

Figure 11. RCS prediction as a function of frequency for a sphere of radius 0.2 m, using a 424-facet model (discretization $\cong$ 0.05 m) for RWG basis functions and first order basis (TL) functions, compared against the exact Mie's solution.

5. SUMMARY

In this paper we presented an enhanced set of triangular patch basis functions which represent an improvement over the traditional Rao, Wilton and Glisson triangular patch basis functions. These basis functions are equivalent to the first order set described in [14] but are presented here in a simpler formulation that allows its use in existing RWG codes with minimal modifications. It has been shown that these new basis functions provide a much better representation of the current distribution than RWG while keeping the same computational complexity. In the examples we have analyzed, we always obtained, for the same triangulation scheme, a better result using the first order basis functions in terms of RCS prediction. In terms of current distribution, the comparative performance is even better for this new formulation. Therefore we can conclude that this set of basis functions really represents an improvement over the traditional RWG basis. Also, its implementation can be easily extended to the magnetic field and combined field integral equation formulations.

As a final remark we should mention that the development of higher-order basis functions has received much attention recently [14–17]. Higher-order basis achieves a faster convergence rate at the

price of increased computational cost for the matrix elements. In comparison, the formulation presents here does not claim to provide faster convergence rate, but is a fast and easy modification to existing RWG-based computer codes to achieve enhanced performance.

REFERENCES

1. Rao, S. M., D. R. Wilton, and A. W. Glisson, "Electromagnetic scattering by surfaces of arbitrary shape," *IEEE Trans. Antennas Propagat.*, Vol. 30, 409–418, May 1982.
2. Song, J. M., C. C. Lu, W. C. Chew, "Multilevel fast multipole algorithm for electromagnetic scattering by large complex objects," *IEEE Trans. Antennas Propagat.*, Vol. 45, 1488–1493, Oct. 1997.
3. Hodges, R. E. and Y. R. Samii, "The evaluation of MFIE integrals with the use of vector triangle basis functions," *Microwave Optical Technology Letters,* Vol. 14, 9–14, Jan. 1997.
4. Trintinalia, L. C. and H. Ling, "Electromagnetic scattering from 3-D arbitrary coated cavities via a connection scheme using triangular patches," *J. Electr. Wave Applic.*, Vol. 8, 1411–1423, Nov. 1994.
5. Rao, S. M., C. C. Cha, R. L. Cravey, et al., "Electromagnetic scattering from arbitrary shaped conducting bodies coated with lossy materials of arbitrary thickness," *IEEE Trans. Antennas Propagat.*, Vol. 39, 627–631, May 1991.
6. Umashankar, K., A. Taflove, and S. M. Rao, "Electromagnetic scattering by arbitrary shaped 3-dimensional homogeneous lossy dielectric objects," *IEEE Trans. Antennas Propagat.*, Vol. 34, 758–766, June 1986.
7. Rao, S. M. and D. R. Wilton, "Transient scattering by conducting surfaces of arbitrary shape," *IEEE Trans. Antennas Propagat.*, Vol. 39, 56–61, Jan. 1991.
8. Peters, T. J. and J. L. Volakis, "Application of a conjugate-gradient FFT method to scattering from thin planar material plates," *IEEE Trans. Antennas Propagat.*, Vol. 36, 518–526, Apr. 1988.
9. Sarkar, T. K., S. M. Rao, and A. R. Djordjevic, "Electromagnetic scattering and radiation from finite microstrip structures," *IEEE Trans. Microwave Theory Tech.*, Vol. 38, 1568–1575, Nov. 1990.
10. Wilkes, D. and C. C. Cha, "Method of moments solution with parametric curved triangular patches," *Proc. 1991 IEEE Int. Symp. Antennas Propagat.*, 1512–1515, 1991.

11. Brown, W. J. and D. R. Wilton, "Singular basis functions and curvilinear triangles in the solution of the electric field integral equation," *IEEE Trans. Antennas Propagat.*, Vol. 47, 347–353, Feb. 1999.
12. Kim, J. S., J. H. Yun, A. K. Lee, and N. Kim, "EMI analysis of finite sized image planes configuration using triangular patch model," *Electronics Letters,* Vol. 34, 1735–1736, Sept. 1998.
13. Altman, Z., R. Mittra, O. Hashimoto, and E. Michielssen, "Efficient representation of induced currents on large scatterers using the generalized pencil of function method," *IEEE Trans. Antennas Propagat.*, Vol. 44, 51–57, Jan. 1996.
14. Wang, J. and J. P. Webb, "Hierarchal vector boundary elements and p-adaption for 3-D electromagnetic scattering," *IEEE Trans. Antennas Propagat.*, Vol. 45, 1869–1879, Dec. 1997.
15. Graglia, R. D., D. R. Wilton, and A. F. Peterson, "Higher order interpolatory vector bases for computational electromagnetics," *IEEE Trans. Antennas Propagat.*, Vol. 45, 329–342, Mar. 1997.
16. Donepudi, K. C., J. M. Jin, S. Velamparambil, J. M. Song, and W. C. Chew, "A higher-order parallelized multilevel fast multipole algorithm for 3D scattering," Univ. of Illinois Center for Comp. Electromag. Tech. Rept. CCEM-36-99, Urbana, IL, Nov. 1999.
17. Yu, T. and W. Cai, "High order current basis functions for method of moments in electromagnetic scattering," *IEEE Antennas Propagat. Soc. Int. Symp. Dig.*, Vol. 1, 472–475, July 2000.

Luiz Cezar Trintinalia was born in São Paulo, Brazil, on June 12, 1964. He received the B.S. degree in Electrical Engineering, in 1987 and the M.S. degree, also in Electrical Engineering in 1992, both from Escola Politécnica da Universidade de São Paulo in Brazil. He received the Ph.D. degree in Electrical Engineering from the University of Texas at Austin, in 1996. He joined the faculty of Escola Politécnica da Universidade de São Paulo in 1987 and is currently an Assistant Professor of the Department of Telecommunications and Control Engineering. His research interests are in computational electromagnetics, smart antennas for cellular systems and radar signal analysis for scattering mechanism interpretation and target identification

Hao Ling was born in Taichung, Taiwan, on September 26, 1959. He received the B.S. degrees in Electrical Engineering and Physics from the Massachusetts Institute of Technology, Cambridge, in 1982,

and the M.S. and Ph.D. degrees in Electrical Engineering from the University of Illinois at Urbana-Champaign, in 1983 and 1986, respectively. In September 1986, he joined the faculty of the University of Texas at Austin and is currently a Professor of Electrical and Computer Engineering. In 1982 he was associated with the IBM Thomas J. Watson Research Center, Yorktown Heights, NY, where he conducted low-temperature experiments in the Josephson Program. He participated in the Summer Visiting Faculty Program in 1987 at the Lawrence Livermore National Laboratory, CA. In 1990 he was an Air Force Summer Fellow at the Rome Air Development Center, Hanscom Air Force Base, MA. His research interests are in radar signature prediction, computational techniques, and radar signal analysis for scattering mechanism interpretation and target identification. Dr. Ling was a recipient of the National Science Foundation Presidential Young Investigator Award in 1987, the NASA Certificate of Appreciation in 1991, and the Archie Straiton Junior Faculty Teaching Excellence Award in 1993 and holder of the Chevron Centennial Fellowship in Engineering.

On the Simultaneous Modeling of Array Mutual Coupling and Array-Platform Interactions

Tao Su and Hao Ling
Dept. of Electrical and Computer Engineering
The University of Texas at Austin
Austin, TX 78712

Abstract

The active element patterns of antenna arrays are strongly affected by the interaction between the elements and the mounting platform. In this paper, a combined model is proposed to model the array response including both mutual coupling and the platform effect. The mutual coupling is described by a coupling matrix while the platform scattering is represented using the point scatterer model. An algorithm based on the matching pursuit concept is proposed to determine the model coefficients. Numerical results show that the active element patterns are well described by the model.

Key words: Array mutual coupling, array-platform interaction, point scatterer model

I. Introduction

It is well known that the characteristics of an antenna array are strongly affected by the mutual coupling between array elements [1-8]. Mutual coupling is often modeled using a coupling matrix [3-5]. For an N-element array, the coupling matrix is an N by N matrix relating the active element patterns, which are the antenna element patterns in the array environment, to the free-standing element patterns. Under most conditions, the coupling matrix provides a very effective way to model the array response in the presence of mutual coupling. However, if the array is mounted on a platform, the active element patterns are further modified by the scattering from the platform [9]. In this case, the mutual coupling matrix alone is insufficient to describe the radiation physics. Recently, we have shown that antenna-platform interactions can be well described by a sparse point scatterer model [10,11]. In this approach, the scattered field from the platform is approximated by the contributions of a few point scatterers. In this paper, we propose a combined model that takes into account of both the mutual coupling and the antenna-platform interaction. This model combines the coupling matrix approach and the point scatterer description of the platform scattering to fully characterize the radiation physics associated with arrays mounted on complex platforms. In Section II, the mutual coupling model is reviewed and the combined model is described. In Section III, an algorithm based on the matching pursuit concept [12] is proposed to determine the model parameters including the position and strength of the point scatterers. Numerical results are provided in Section IV to demonstrate the effectiveness of the model.

II. The Combined Model

Assume an array with N elements is located in the xy-plane and receives a plane wave incident from angle ϕ in the azimuth plane. The standard mutual coupling model [3-5] relates the active element patterns to the free-standing element patterns by a coupling matrix as follows:

$$\mathbf{A}_{true} = \mathbf{C}\mathbf{A}_{theo} \tag{1}$$

where $\mathbf{A}_{true}$ and $\mathbf{A}_{theo}$ are the active and free-standing element patterns, respectively, and $\mathbf{C}$ is the N by N coupling matrix. For antenna elements having isotropic patterns in the xy-plane, the elements of $\mathbf{A}_{theo}$ are given by:

$$\mathbf{A}_{theo}(i,\phi) = e^{jk(x_i\cos\phi + y_i\sin\phi)},\ i = 1,\cdots,N \tag{2}$$

where (x_i, y_i) is the coordinate of the ith element. The active pattern matrix $\mathbf{A}_{true}$ has the same structure as $\mathbf{A}_{theo}$, except each row represents the antenna element pattern in the array environment. Given the active element patterns at a few incident angles, the matrix $\mathbf{C}$ can be determined using the pseudo inverse as follows:

$$\mathbf{C} = \mathbf{A}_{true}\mathbf{A}_{theo}^{\mathbf{H}}(\mathbf{A}_{theo}\mathbf{A}_{theo}^{\mathbf{H}})^{-1} \tag{3}$$

In [8], we demonstrated that the model in (1) is valid if the current distribution on each stand-alone element has a constant shape for all incident angles. It was also shown that when the antenna elements are resonant, the constant-current-shape condition is approximately satisfied. This situation should still hold true even if a platform exists. Thus the mutual coupling model can be extended to the case when a platform is present, provided that we replace the free-standing element patterns in $\mathbf{A}_{theo}$ by the array element patterns in the presence of the platform (but in the absence of the other elements). Next we consider how the platform affects the stand-alone pattern of each element.

For a stand-alone element, the platform scattering changes the incident field over the element. The total incident field on the element can be viewed as a sum of the direct incident field and the scattered field from the platform. As shown in [10,11], for an electrically large platform, the scattered field can be adequately described using a sparse point scatterer model. Consequently, we can incorporate the platform effect in the mutual coupling model as follows:

$$\mathbf{A}_{true} = \mathbf{C}(\mathbf{A}_{theo} + \mathbf{P}\mathbf{A}_{plat}) = \mathbf{C}[\mathbf{I}\ \mathbf{P}]\begin{bmatrix}\mathbf{A}_{theo}\\ \mathbf{A}_{plat}\end{bmatrix} \tag{4}$$

In this model, $\mathbf{A}_{plat}$ represents the incident fields upon the point scatterers representing the platform. It has the exact same form as an ideal element pattern in (2), where (x_i, y_i) represents the coordinate of the point scatterer. Each column of the matrix **P** describes the scattering from each point scatterer to the array elements. It includes both the strength of the scatterer and the phase delay from the scatterer to the array elements. **I** is the identity matrix. It is clearly shown in this equation that the stand-alone element patterns consist of two parts, the free-standing element patterns and the modification due to the platform. Thus the model is consistent with the physics of the actual problem.

III. Determination of Model Coefficients

To determine the positions of the point scatterers, one standard way is to generate a projection image [13] in two-dimensional (2D) space. In this method, we assume a point scatterer is located at (x, y). The matrix $\mathbf{A}_{plat}$ becomes a row vector given by:

$$\mathbf{A}_{plat}(\phi) = e^{jk(x\cos\phi + y\sin\phi)} \tag{5}$$

We can then determine the matrix **C[I P]** using the pseudo inverse technique similar to (3). Once **C** and **CP** are explicitly obtained, the column vector **P** can be determined by left-multiplying **CP** by $\mathbf{C}^{-1}$. The above process can be viewed as a projection of the assumed point scatterer response onto the actual array response including platform effects. The energy in **P** will be maximum if we choose the correct point scatterer location. Thus we can take the norm of **P** to form a 2D image as a function of (x, y). The positions of the point scatterers are determined from the peaks in the image.

However, the drawback of this approach is that the 2D image is generated using one-dimensional data. The sidelobes of the peaks are expected to be very high such that the peaks corresponding to the weaker point scatterers may be shadowed. To illustrate this, we consider the simplified projection image of a single point scatterer without any array elements. Suppose the point scatterer is located at (x_0, y_0), the image strength at an assumed point (x, y) is given by

$$\begin{aligned}\Psi(x,y) &= \left| \int_0^{2\pi} e^{jk(x\cos\phi + y\sin\phi)} [e^{jk(x_0\cos\phi + y_0\sin\phi)}]^* d\phi \right| \\ &= \left| \int_0^{2\pi} e^{jkr(\cos\phi_0\cos\phi + \sin\phi_0\sin\phi)} d\phi \right| \\ &= \left| 2\pi J_0(kr) \right| \end{aligned} \tag{6}$$

where $r = \sqrt{(x-x_0)^2 + (y-y_0)^2}$ is the distance between (x, y) and (x_0, y_0). Thus the projection image of a single point scatterer is a zeroth order Bessel function centered at (x_0, y_0). The sidelobe of the Bessel function is so high (about 8 dB) that simultaneous identification of point scatterers is nearly impossible. To overcome this problem, we employ a matching pursuit algorithm [12] to determine the point scatterer positions iteratively.

In the matching pursuit algorithm, a projection image is generated at each iteration. The first image is generated using $\|\mathbf{P}\|$ as described above. The strongest point in the image is picked to be the first point scatterer. The position information is stored in $\mathbf{A}_{plat}$. In the second iteration, we assume the position of the next point scatterer and append $\mathbf{A}_{plat}$ by one row. A new projection image is then formed using the norm of the last column of $\mathbf{P}$ and the second point scatterer is determined. The process is repeated until the total energy in the projection image is small enough to be neglected.

Using this method, the point scatterers are determined one at a time. Once a point scatterer is included in the model, its sidelobe is taken into account so that it will not overshadow the weaker point scatterers in the subsequent projection images.

IV. Numerical Results

In this section, two examples are provided to validate the combined model of mutual coupling and platform effects. In the first example, we simulate a linear array of half-wave dipoles mounted on a ship-like platform. The array and the platform geometry are shown in Fig. 1. The separation between the array elements is 0.45 wavelength. We simulate the problem with FISC [14], which is a method of moments code based on the multi-level fast multipole method. The active element patterns at 36 uniformly distributed incident angles are used to extract the model coefficients in (4). Fig. 2 shows the projection image generated in the first iteration of the matching pursuit algorithm. A strong point scatterer can be identified at the back corner of the front cylinder. The high sidelobes associated with this scatterer can also be seen from the image. In Fig. 3, the first 15 point scatterers extracted by the matching pursuit algorithm are plotted over the

platform. The scatterers are mostly distributed along the centerline of the ship, and correspond to the expected specular reflection, tip diffraction and corner scattering mechanisms on the topside structure. Two weak scatterers are asymmetric about the center line. The asymmetry is due to numerical noise in the extraction.

Once the combined model is obtained, we can reconstruct the active element patterns at arbitrary incident angles. The reconstructed and simulated active element patterns are plotted in Fig. 4, in dashed and solid lines, respectively. The agreement between the two is very good. As a comparison, we also obtained a model based on the traditional mutual coupling model in (1) without any platform considerations. The active element patterns reconstructed from the traditional model are plotted in dash-dot lines. It can be seen that the fine structures of the array response are not captured by the traditional model. The difference is more dramatic when we examine the phase error of the reconstructed element patterns by the combined model and the traditional model. They are shown in Fig. 5 in solid and dashed curves, respectively. We can see that the combined model performs considerably better in terms of phase error.

In some applications such as direction finding, the phase of the active element patterns can be quite important. To demonstrate this, we simulate the array response when there are two incoming signals separated by 15°. A signal-to-noise ratio of 30 dB is assumed. The MUSIC superresolution algorithm is employed to determine the incoming signal directions in the presence of noise. The normalized MUSIC power spectrum using the exact active element patterns is plotted as solid curve in Fig. 6. The power spectra resulting from the combined model and the traditional coupling model are plotted in

dashed and dash-dot curves, respectively. We can see that the two incident signals can be well separated using the combined model, while the traditional model fails.

In the second example, a 7-element circular array of dipoles with a center pole and some surrounding structures is simulated. The array-platform geometry is shown in Fig. 7. The combined model is extracted using the active element patterns computed at 36 angles and is used to reconstruct the patterns. The projection image in the first iteration of the matching pursuit algorithm is shown in Fig. 8. The strongest scattering from the platform is observed to be coming from the corner of the nearby box. The extracted point scatterers are also plotted as circles in this figure. While the ring structure in the image resembles the case where there is a point scatterer at the center of the array, none is extracted by the algorithm. We believe this is because the scatterers are too close to the antenna elements. As a result, $\mathbf{A}_{theo}$ and $\mathbf{A}_{plat}$ in (4) are too similar and the effect from the point scatterers is included in the $\mathbf{C}$ matrix instead. Despite this degeneracy, the resulting model is still adequate in describing the active element patterns. Fig. 9 shows the phase errors in the reconstructed active element patterns based on the model. We again see that the combined model performs much better than the traditional coupling model. The direction finding results corresponding to the different active element patterns are plotted in Fig. 10. As expected, the combined model outperforms the traditional coupling model, as it can clearly distinguish the two incoming signals.

V. Conclusions

In this paper, we have proposed a combined model to describe the response of an antenna array in the presence of both mutual coupling and platform effects. The mutual

coupling between the array elements is described by a coupling matrix. In addition, the platform effect is approximated using the point scatterer model. We have also proposed an algorithm based on matching pursuit to determine the model coefficients. Numerical results show that the active element patterns reconstructed from the model is in good agreement with the actual data. The main attractiveness of the new model is that it provides physical insights into the coupling and scattering mechanisms. By parameterizing the active element patterns using the proposed model, we can locate the position and strength of the dominant point scatterers that give rise to platform scattering.

Acknowledgment

This work was supported by the Office of Naval Research under Contract No. N00014-98-1-0178 and N00014-01-0234.

References

[1] D. F. Kelley and W. L. Stutzman, "Array antenna pattern modeling methods that include mutual coupling effects," *IEEE Trans. Antennas Propagat.*, v. 41, pp 1625-1632, Dec. 1993.

[2] I. J. Gupta and A. A. Ksienski, "Effect of mutual coupling on the performance of adaptive arrays," *IEEE Trans. Antennas Propagat.*, v. 31, pp 785-791, Sept. 1983.

[3] B. Friedlander and J. Weiss, "Direction finding in the presence of mutual coupling," *IEEE Trans. Antennas Propagat.*, v. 39, pp 273-284, Mar. 1991.

[4] T. Svantesson, "Modeling and estimation of mutual coupling in a uniform linear array of dipoles," *IEEE Int. Conf. Acoust. Speech Signal Processing*, pp. 2961-2964, Phoenix, 1999.

[5] C. M. S. See, "A method for array calibration in parametric sensor array processing," *IEEE Singapore Int. Conf. on Communication Systems*, pp. 915-919, Singapore, 1994.

[6] R. S. Adve and T. K. Sarkar, "Compensation for the effects of mutual coupling on direct data domain adaptive algorithms," *IEEE Trans. Antennas Propagat.*, vol. 48, pp. 86-94, Jan. 2000.

[7] T. Su, K. Dandekar and H. Ling, "Simulation of mutual coupling effect in circular arrays for direction finding applications," *Microwave Optical Tech. Lett.*, vol. 26, pp. 331-336, Sept. 2000.

[8] T. Su and H. Ling, "On modeling mutual coupling in antenna arrays using the coupling matrix," *Microwave Optical Tech. Lett.*, vol. 28, pp. 231-237, Feb. 2001.

[9] T. Milligan, F. Obelleiro, L. Landesa, J. Taboada and J. Rodriguez, "Synthesis of onboard array antennas including interaction with the mounting platform and mutual coupling effects," *IEEE Antennas Propagat. Mag.*, vol. 43, pp. 76-82, Apr. 2001.

[10] C. Ozdemir, R. Bhalla and H. Ling, "A radiation center representation of antenna radiation pattern on a complex platform," *IEEE Trans. Antennas Propagat.*, vol. AP-48, pp. 992-1000, June 2000.

[11] T. Su, C. Ozdemir and H. Ling, "On extracting the radiation center representation of antenna radiation patterns on complex platform," *Microwave Optical Tech. Lett.*, vol. 26, pp. 4-7, July 2000.

[12] S. G. Mallat and Z. Zhang, "Matching pursuits with time-frequency dictionaries," *IEEE Trans. Signal Processing*, v. 41, pp. 3397-3415, Dec. 1993.

[13] G. T. Herman, *Image Reconstruction from Projections*, Academic Press, New York, 1980.

[14] *User's Manual for FISC (Fast Illinois Solver Code)*, Center for Computational Electromagnetics, University of Illinois at Urbana-Champaign and DEMACO, Inc., IL, Jan. 1997.

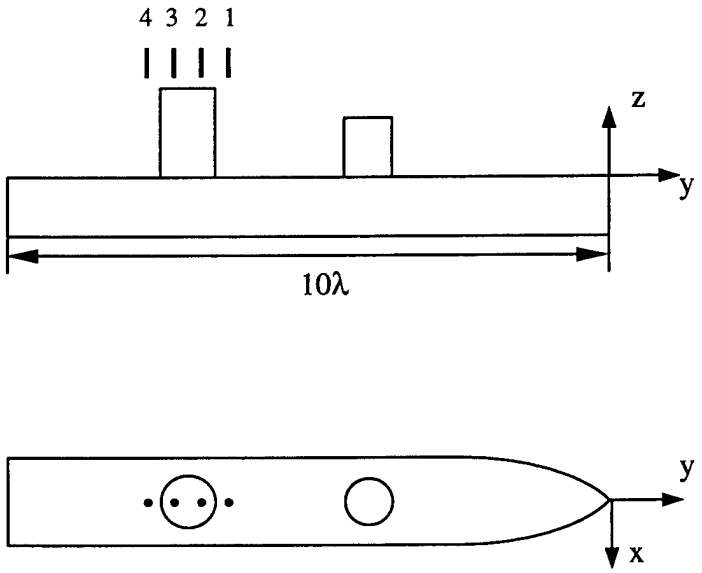

Fig. 1. Array-platform geometry of example 1

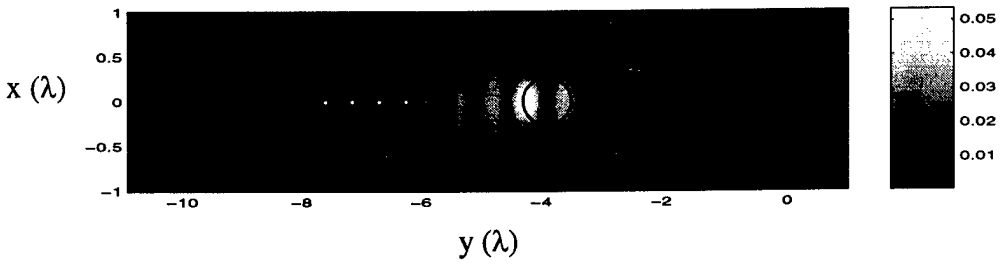

Fig. 2. Projection image in the first iteration of the matching pursuit algorithm

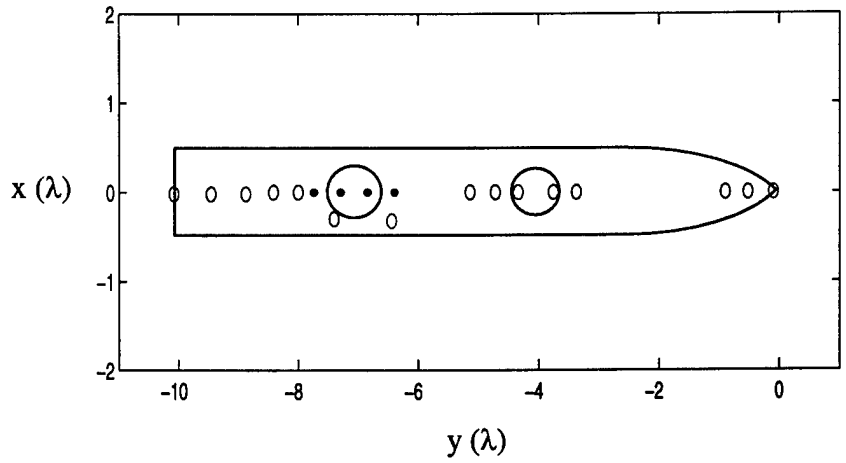

Fig. 3. The extracted point scatterers

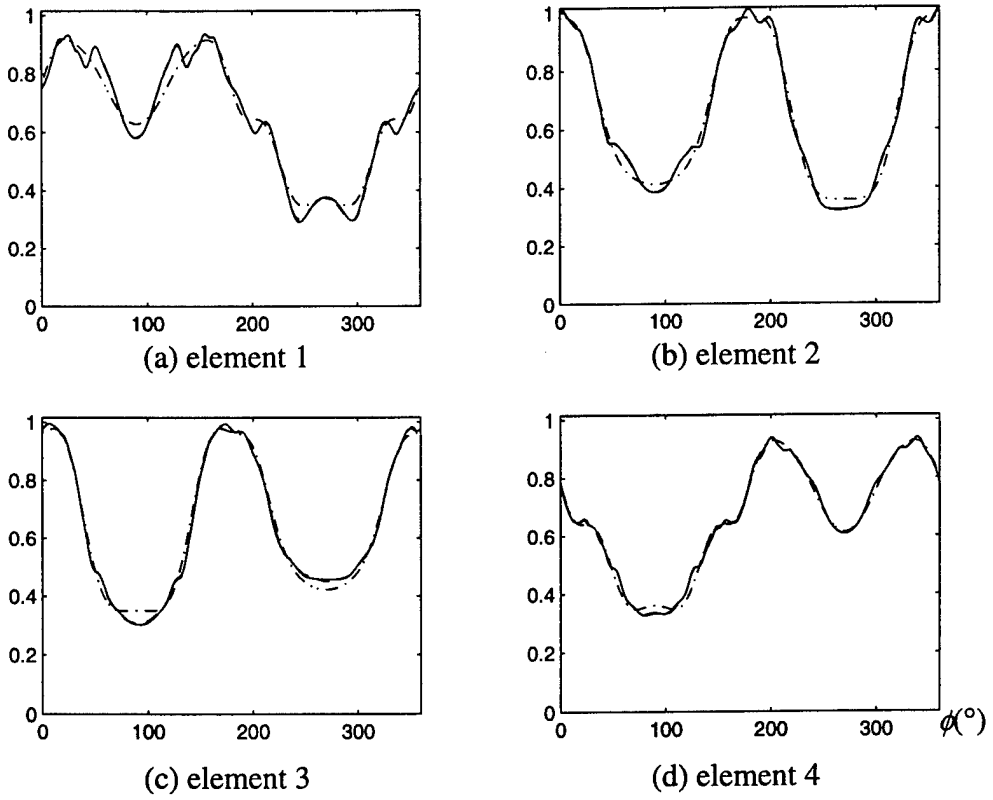

Fig. 4. Actual and reconstructed active element patterns

——— Actual data

------- Combined model

-·-·-·- Traditional coupling model

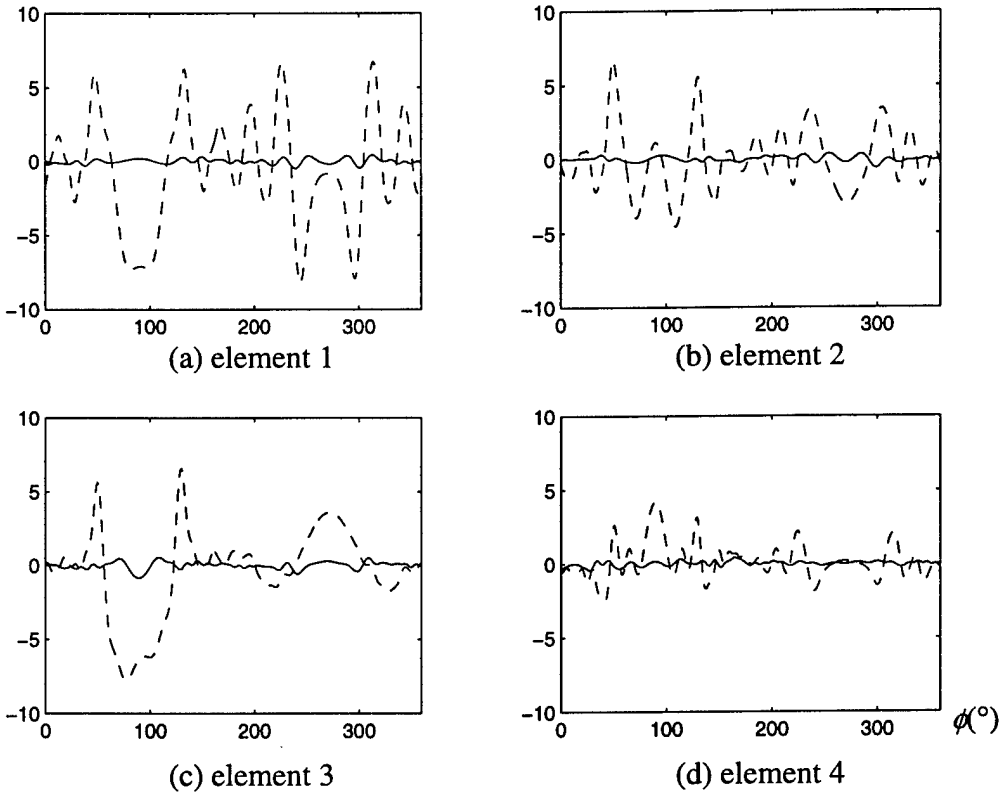

Fig. 5. Phase error of the reconstructed active element patterns

——— Combined model

------- Traditional coupling model

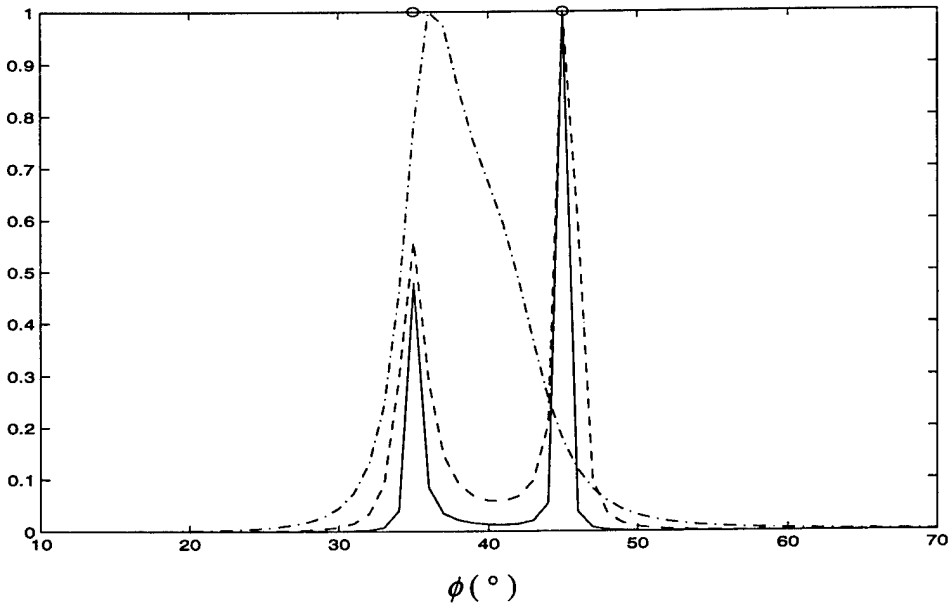

Fig. 6. MUSIC power spectra using different active element patterns

——— Actual data
------ Combined model
—·—·— Traditional coupling model

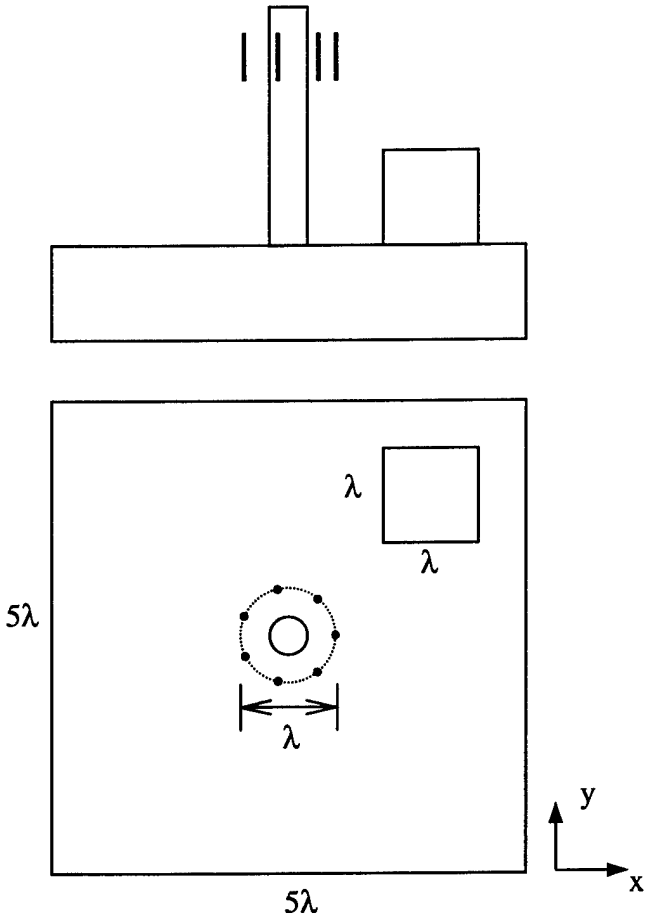

Fig. 7. Array-platform geometry of example 2

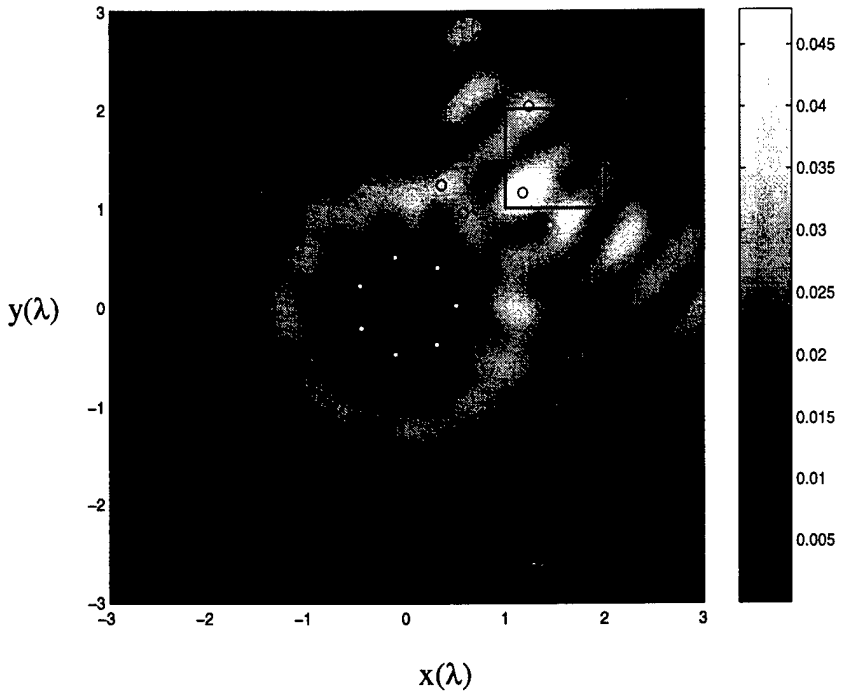

Fig. 8. First-iteration projection image and extracted point scatterers

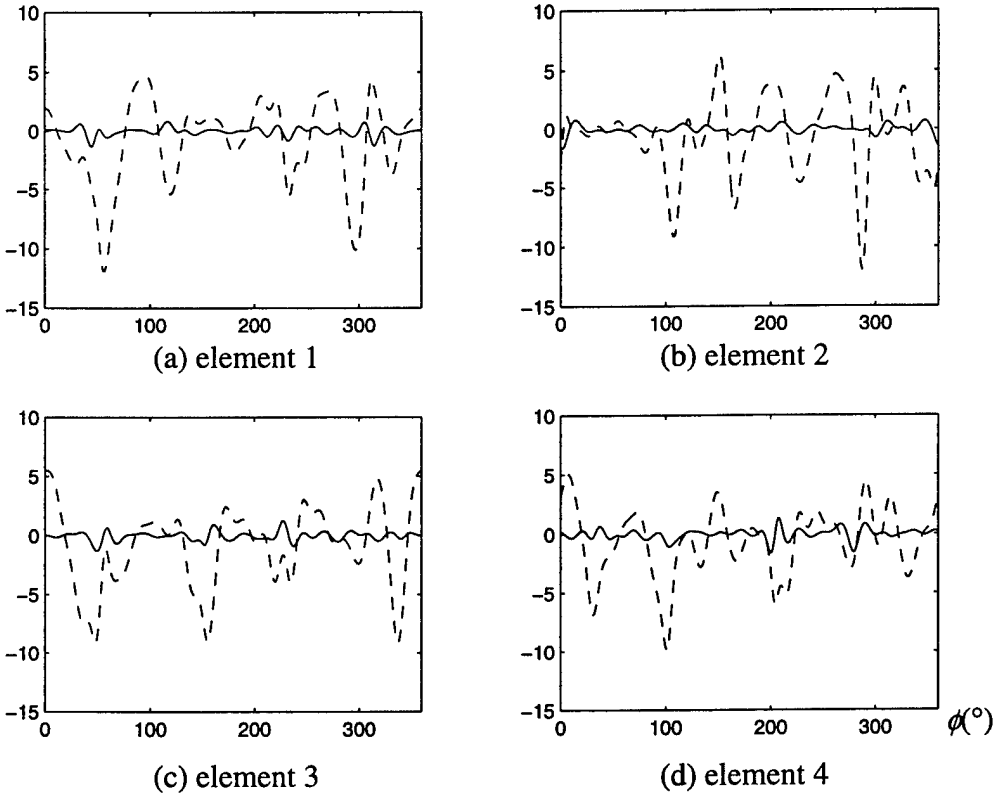

Fig. 9. Phase error of the reconstructed active element patterns
——— Combined model
------- Traditional coupling model

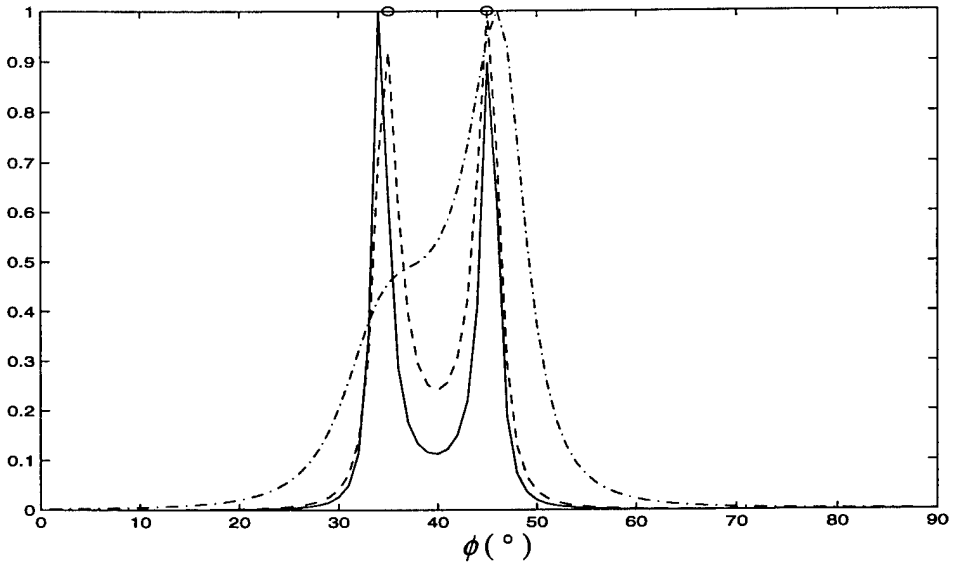

Fig. 10. MUSIC power spectra using different active element patterns

——— Actual data
------ Combined model
–·–·– Traditional coupling model

Experimental Study of Mutual Coupling Compensation in Smart Antenna Applications

Kapil R. Dandekar, Hao Ling, and Guanghan Xu

Department of Electrical and Computer Engineering

The University of Texas at Austin

(dandekar, ling, xu)@ece.utexas.edu

Abstract:

This paper investigates the benefit of mutual coupling compensation via a Method of Moments (MoM) approach in a uniform circular antenna array operating at 1.8 GHz. This mutual coupling compensation technique is applied to a direction of arrival (DOA) study of up to two co-channel mobile users. Field measurements and computer simulations are examined to explore the assumptions of the technique and verify its effect when using the Bartlett and MUSIC DOA algorithms. Computer simulations considering the application of the technique to downlink beamforming are also included. Experimental results show that the mutual coupling compensation technique improves uplink DOA algorithm performance primarily by reducing unwanted sidelobe levels. This reduction in sidelobe levels aids in downlink beamforming weight design. Specifically, simulation results show that use of the compensation technique allows DOA-based downlink beamforming algorithms to perform similarly to spatial signature-based algorithms. All field measurements were made using the smart antenna testbed at the University of Texas at Austin.

Index Terms: Adaptive Arrays, Antenna Array Mutual Coupling, Array Signal Processing, Direction of Arrival Estimation

I. Introduction:

Planning for 3rd generation cellular systems is currently underway to handle the increasing demand for wireless services. Smart antenna technology, making use of adaptive antenna arrays, is capable of improving system capacity and quality, and will be an essential component in these next generation cellular systems. Fully realizing the potential of smart antenna systems requires an appreciation of the underlying electromagnetic effects governing antenna array operations. These electromagnetic effects include mutual coupling as well as amplitude and phase mismatch between array elements.

It has become clear to the smart antenna community that the actual response of the antenna array can deviate significantly from the assumed and simplistic model due to electromagnetic coupling among the antenna elements as well as scattering from the antenna tower and nearby structures. Most studies of mutual coupling in antenna arrays can be best characterized as array calibration methods [1-5]. These methods are generally derived using parametric antenna array models that do not directly consider the underlying electromagnetic principles. A costly alternative to these methods involves determining the actual array response using field measurements.

The same problem can also be approached from a fundamental electromagnetics perspective [6-10]. In this paper, this approach is applied to uniform circular arrays to demonstrate in field measurements the effects of mutual coupling compensation. In this mutual coupling compensation technique, the Method of Moments [11] (MoM) is used to compute an array response that compensates for mutual coupling. The paper will then examine uplink (mobile to basestation) DOA algorithm performance in field

measurements for scenarios involving up to two co-channel mobile users. The study will also consider compensation in downlink (basestation to mobile) beamforming scenarios and thus determine the applicability of the technique.

Section II introduces a mathematical model of the smart antenna array and describes the manner in which the mutual coupling compensation technique can be derived. Section III briefly describes the MoM calculation necessary for coupling characterization. Field measurement and simulation results of the considered compensation technique are discussed in Section IV.

II. Smart Antenna Model

A. Array Output

Assume that there are M elements in the base station antenna array located at (x_i, y_i), $1 \leq i \leq M$. We define the concept of a steering vector (sometimes called array response vector) that can be thought of as the spatial analog of an impulse response in temporal processing. Specifically, it characterizes the relative phase response of each antenna array element to an incident signal with DOA θ. Equation (1) represents the basic form of the theoretical (uncompensated) steering vector.

$$\vec{\mathbf{a}}_U(\theta) = \begin{bmatrix} \exp(-jk(x_1\cos\theta + y_1\sin\theta)) \\ \exp(-jk(x_2\cos\theta + y_2\sin\theta)) \\ \exp(-jk(x_3\cos\theta + y_3\sin\theta)) \\ \bullet\bullet\bullet \\ \exp(-jk(x_M\cos\theta + y_M\sin\theta)) \end{bmatrix} \tag{1}$$

In the above equation, k is the wavenumber of the incident electromagnetic radiation that can be expressed as $2\pi/\lambda$. An array manifold matrix, **A** contains as its columns a collection of steering vectors corresponding to a set of angles.

DOA algorithms directly use knowledge of the array steering vector to generate a spatial spectrum that gives signal power versus direction. A simple approach to this DOA estimation is to assume the ideal steering vector given in Equation (1). This ideal steering vector is a function of array geometry and incident angle, but does not take into account mutual coupling effects. Specifically, Equation (1) does not take into account the retransmission of energy from each antenna element to the others.

The concept of a spatial signature will be relevant for the discussion of downlink beamforming algorithms and is introduced here. The spatial signature model considers uplink antenna array output due to a single user to be a linear combination of the steering vectors of all the direct path and multipath components.

$$\vec{\mathbf{x}}(t) \cong \vec{\mathbf{a}}(\theta_1)s_1(t) + \sum_{i=2}^{N_M} \alpha_i \vec{\mathbf{a}}(\theta_i)s_1(t) = \vec{\mathbf{v}}_1 s_1(t) \qquad (2)$$

$\vec{\mathbf{v}}_1$ is defined to be the spatial signature of mobile user 1. $\vec{\mathbf{a}}(\theta_1)s_1(t)$ is the direct path component and $\alpha_i\vec{\mathbf{a}}(\theta_i)s_1(t)$, $2 \le i \le N_M$, are the multipath components. The α_i contain the relative amplitude and phase of the i^{th} signal component (modeling relative attenuation and delay respectively).

B. Distortion Matrix

A distortion matrix, C, is used to encapsulate the effect of mutual coupling as well as the amplitude and phase distortions caused by imperfect antenna array elements. This

matrix, which can be estimated from collected measurement data [1-5], is applied to the equation of the theoretical steering vector form of (1) to develop a steering vector that takes mutual coupling and unknown sensor gains and phases into account.

$$\vec{\mathbf{a}}_C(\theta) = C(\theta)\vec{\mathbf{a}}_U(\theta) \tag{3}$$

In the literature, to simplify the problem, the distortion matrix is generally considered to be independent of angle. This assumption will be considered in Section IV. Array calibration methods attempt to estimate the matrix C algorithmically off-line [2,3], on-line [4,12], or specifically measure $\vec{\mathbf{a}}_C(\theta)$ using field measurements. However, one of the main problems in estimating the distortion matrix is that it is hard to separate coupling, gain, and phase issues from environmental factors such as tower platform effects and other scatterers located close to the array [9].

C. Uplink Direction of Arrival Algorithms

An important quantity in many array signal processing algorithms is the Spatial Covariance Matrix, **R**. It is defined in Equation (4).

$$\mathbf{R} = E\left(\vec{\mathbf{x}}(t)\vec{\mathbf{x}}^H(t)\right) \tag{4}$$

$\vec{\mathbf{x}}^H(t)$ indicates the complex conjugate transpose of vector $\vec{\mathbf{x}}(t)$. In practice, this matrix is estimated using N snapshots of the actual antenna array output (with sampling interval T), as shown in Equation (5).

$$\tilde{\mathbf{R}} = \frac{1}{N}\sum_{k=1}^{N}\vec{\mathbf{x}}(kT)\vec{\mathbf{x}}^H(kT) \tag{5}$$

An eigenvalue decomposition of **R** can be used to find the orthogonal projector onto the estimated noise subspace, $\Pi^{\perp}$. Using this information, the equations for the Bartlett and MUSIC spatial spectra can be derived [13]:

$$\mathbf{P}_{\text{BARTLETT}}(\theta) = \frac{\vec{\mathbf{a}}^{H}(\theta)\tilde{\mathbf{R}}\vec{\mathbf{a}}(\theta)}{\vec{\mathbf{a}}^{H}(\theta)\vec{\mathbf{a}}(\theta)} \tag{6}$$

$$\mathbf{P}_{\text{MUSIC}}(\theta) = \frac{\vec{\mathbf{a}}^{H}(\theta)\vec{\mathbf{a}}(\theta)}{\vec{\mathbf{a}}^{H}(\theta)\Pi^{\perp}\vec{\mathbf{a}}(\theta)} \tag{7}$$

D. Downlink Beamforming Methods

DOA information gathered during uplink is used by a given downlink beamforming algorithm for the purpose of transmitting information most efficiently from the base station to the mobile user. Each downlink beamforming method has its own technique for how best to accomplish this efficient transmission [14,15].

- Dominant DOA (DomDOA) method – For a given mobile user, this method takes the angle at which there is the greatest received power during uplink (determined by uplink spatial spectrum) and focuses all transmitted energy in that direction.
- Pseudoinverse DOA (PseDOA) method – In addition to transmitting in the direction of the strongest DOA of the desired user like the DomDOA method, nulls are placed in the antenna radiation pattern at both the non-dominant DOAs of the desired user and all the DOAs of any other mobile users in the system.
- Spatial Signature (SS) method – This method uses the spatial signature of the mobile user when constructing the downlink weight vector. It differs from the

prior two methods in that instead of focusing signal energy only in the direction of the dominant DOA of the desired mobile user, it steers the beam of signal energy in all directions corresponding to the desired mobile user.

- Pseudoinverse Spatial Signature (PseSS) method – Whereas the SS method tried to maximize SNR without inserting nulls, this method maximizes SNR while inserting nulls. Specifically, nulls are inserted at the DOAs corresponding to the spatial signature of the other mobile users in the system.

It is important to note that the SS and PseSS methods do not use steering vectors at all when constructing downlink beamforming weights. While the spatial signature can be modeled as a linear combination of steering vectors, this decomposition is unnecessary when determining the spatial signature and using spatial signature based downlink beamforming algorithms.

III. Mutual Coupling Compensation

Our approach to mutual coupling compensation entails developing an estimate for the actual array response $\vec{\mathbf{a}}_C(\theta)$ given an arbitrary geometry antenna array via MoM code. The MoM code used in this study is NEC (Numerical Electromagnetics Code), which was originally developed at the Lawrence Livermore Laboratory [16] to perform MoM analysis to model the interaction between electromagnetic fields and wire segments. A wire segment model of an arbitrary geometry antenna array can be specified in an input file to NEC. NEC results are well accepted in the literature and versions of NEC are freely distributed on the World Wide Web.

Fundamentally, the MoM represents the unknown induced current on an object in terms of a given set of basis functions and enforces Maxwell's boundary conditions at a finite number of points on the object being modeled [11]. Thus, in the MoM, each antenna array element is represented as a wire of finite thickness divided up into segments. At the heart of the MoM is the calculation of a system impedance matrix Z_{QQ} giving the coupling between segment i and j in the antenna array model ($1 \leq i,j \leq Q$) where Q is the total number of wire segments in the model. The value of Q needs to be chosen to be large enough so that the obtained current solution on each of the antenna elements converge to a fixed function. In general, the higher the number of segments, the greater the validity and resolution of the answer (at the expense of greater computational effort). A detailed formulation of the modeling of an antenna array using the MoM can be found in the work of Pasala [7] and Adve [10].

A 7-element circular array was used in simulations and measurements in this study. The simulated antenna elements are each coaxial dipole elements containing four collinear $\lambda/2$ dipole antennas (illustrated in Figure 1) with an operating frequency of 1.88 GHz. Each of the dipole elements is represented as a wire divided up into segments for MoM analysis. Lump loading is used to model the isolation between the dipole antennas and the load impedance of the array elements.

Two types of mutual coupling compensation using MoM were considered in this study. In the first type of compensation, MoM calculations were used to determine the true steering vectors in the azimuth plane perpendicular to the axis of the array elements. This complete array manifold is then used when performing uplink DOA analysis. In the

second compensation technique, based upon [1-5,9], the steering vectors at only a few angles are computed, and Equation (3) is solved for the distortion matrix (assuming angular independence) using the equation:

$$C = A_{true} A_{theo}^{H} (A_{theo} A_{theo}^{H})^{-1} \tag{8}$$

where the columns of A_{true} and A_{theo} are the MoM determined (compensated) steering vectors and the theoretical (uncompensated) steering vectors respectively, corresponding to a particular set of angles. This distortion matrix is then applied using Equation (3) to determine compensated steering vectors. Field measurement comparsion of the results of these two types of compensation allow the assumption of angular independence of the distortion matrix to be examined.

IV. Results

A. Steering Vector Relative Angle Change

We first consider the difference between the ideal (from Equation (1)) and compensated (from NEC simulations) array steering vectors. As a metric, we use the calculation of relative angle change (RAC) between theoretical and compensated array vectors. For a compensated steering vector, a_C, and an uncompensated steering vector, a_U, this metric can be written as:

$$RAC(\%) = 100 \times \sqrt{1 - \frac{\left| \mathbf{a}_C^{*} \cdot \mathbf{a}_U \right|^2}{\left\| \mathbf{a}_C \right\| \left\| \mathbf{a}_U \right\|}} \tag{9}$$

This metric has been used in simulations and measurements [15,17] to provide a measure of the difference between spatial signatures. It is used in this study to quantify the difference between compensated and uncompensated steering vectors, and is shown

in Figure 2. This graph shows that there is an appreciable difference between the compensated and uncompensated steering vectors.

B. Experimental Setup

Data collection was performed outdoors on an open field in the Pickle Research Campus at the University of Texas at Austin. There were two signal generators used to represent mobile users transmitting to the smart antenna basestation. The first signal generator was held stationary. The second signal generator was moved to five distinct angles at approximately the same distance and the same transmission power as the first signal generator. Data was then collected using the smart antenna testbed and uplink spatial spectra were considered for each generator transmitting individually and both generators transmitting together. The position of each of the signal generator locations is listed in Table 1.

C. Uplink Direction of Arrival Algorithm

Figure 3 shows the spatial spectra generated using uncompensated and compensated steering vectors for measurement data due to a single mobile user (referred to as "Stationary User" in Table 1). In this figure, we consider the application of the full array manifold calculated using the MoM. Figure 3a contains Bartlett DOA algorithm output and Figure 3b contains the MUSIC spatial spectrum. These spatial spectra show that while the effect on the detected DOA is minimal for both uncompensated and compensated results, sidelobe levels are significantly reduced through use of mutual coupling compensation. Specifically, Figure 3b shows the typical (for all tested cases)

sidelobe reduction of approximately 3 dB. While compensation has little effect on the main lobe of the Bartlett spatial spectra in Figure 3a, the effect is more pronounced on the MUSIC spatial spectra in Figure 3b.

Figure 4 shows the same results as Figure 3 for a different mobile user. Specifically, it represents the Bartlett and MUSIC DOA algorithm output given the full NEC calculated array manifold for a single mobile user (referred to as "Position 1" in Table 1). Again, this figure shows that mutual coupling compensation has a greater effect on the main lobe of MUSIC spatial spectrum output shown in Figure 4b compared with the effect on the main lobe of the Bartlett spatial spectrum shown in Figure 4a. Both spatial spectra in Figure 4 show a reduction in unwanted sidelobe levels.

Figure 5 shows the uncompensated and compensated MUSIC spatial spectra for a situation in which there was two mobile users ("Stationary User" and "Position 5" in Table 1) transmitting simultaneously. This figure again illustrates the previous results of significant sidelobe reduction along with sharpening of the lobes corresponding to mobile users. Specifically, note that the DOA of the stationary user is made much more prominent compared to the sidelobes due to compensation. These sidelobes could be mistaken for either another mobile user or multipath signal energy – either of which has adverse consequences for downlink beamforming methods such as the PseDOA method. In general for all tested cases (single and multiple user scenarios), mutual coupling compensation increased lobes in the spatial spectra corresponding to desired users' DOAs and decreased all other sidelobes.

Figure 6 shows the effect of assuming the distortion matrix is independent of angle using the same spatial spectrum considered in Figure 3b. For all of the results in

the paper not including those of Figure 6, the compensation technique involved using the entire array manifold computed through NEC. In Figure 6, this technique is referred to as the "Look-up Table" approach. The other tested compensation technique is to compute the distortion matrix (assuming angular independence) using Equation (8) with a relatively small number of MoM-generated and theoretical steering vectors. Results from this study show that making use of the assumption that C is independent of angle yields a performance increase over theoretical steering vector use. This performance increase does not quite match the benefit due to the use of the complete MoM-generated array manifold. However, it should be pointed out that using the "Look-up Table" approach has the disadvantage of requiring more storage than a computed distortion matrix.

D. Downlink Beamforming Algorithm

To determine the effect that mutual coupling compensation has on downlink beamforming, the MoM model for the antenna array was used. The uplink spatial spectra from measurement data for all of the tested cases were used to compute downlink beamforming weights for scenarios involving the Stationary User (User 1) and the mobile user at each of 5 different tested positions (User 2). Figure 7 shows the resulting simulated radiation pattern from using each of the four downlink beamforming methods described in Section II-D. Figure 7a shows the downlink radiation pattern for the Stationary User and Figure 7b shows the pattern for the mobile user at Position 4. This figure shows, for the DOA based methods DomDOA and PseDOA, the effects of using compensated and uncompensated steering vectors. As seen in the top pattern of Figures 7a and 7b, use of compensated steering vectors does not significantly improve the

performance of the DomDOA method. Specifically, both of these patterns show that the main lobes of the uncompensated and compensated DomDOA method are practically the same. Furthermore, both patterns show similar performance to that of the SS method. However, the bottom pattern of Figures 7a and 7b shows that there is significant improvement in the performance of PseDOA method when using compensated steering vectors. These patterns clearly show an improved main lobe when using the compensated PseDOA method instead of the uncompensated PseDOA method. In addition, these patterns show that use of compensation allows the PseDOA method to work comparably to the PseSS method.

To quantify the results illustrated by Figure 7, Table 2 shows the gain in signal power for each mobile user that is realized through use of the compensated PseDOA method over the uncompensated PseDOA method and the PseSS method. Signal power is determined by the value of the radiation plot at the known DOA of the desired user. As seen in this table, the use of compensated steering vectors instead of uncompensated vectors in the PseDOA method (Column 1 for User 1 and Column 3 for User 2) nearly always significantly improves transmitted signal power. Furthermore, this table shows that use of compensated steering vectors allows the PseDOA method to work just as well as the PseSS method (Column 2 for User 1 and Column 4 for User 2), which is normally not true [14].

Table 3 shows the improvement in SIR for the two mobile users using the compensated PseDOA method over the uncompensated PseDOA method. In this table, signal power is determined as before and interference power for one mobile user is determined by the value at that user's DOA on the other user's radiation plot. This table

shows that use of compensated steering vectors instead of uncompensated vectors often significantly improves SIR (Column 1 versus Column 2 for User 1 and Column 3 versus Column 4 for User 2). The results in this table also show that SIR performance is more stable as a function of user position when using compensated steering vectors (Column 1 for User 1 and Column 3 for User 2). This result has beneficial implications for the minimization of cellular call dropping.

V. Conclusion

In this paper, we have examined the benefit of mutual coupling compensation during uplink DOA estimation and during downlink beamforming. Results from our measurement campaign allow us to make several comments regarding mutual coupling compensation. It has been shown through the use of MoM calculations that steering vectors taking into account mutual coupling differ significantly, in terms of relative angle change, from theoretical steering vectors. By using more accurate steering vectors, we observed the expected performance improvement. The performance improvement in terms of direction finding comes from reduced sidelobe levels, which allows for easier distinction of signal sources. The DOA performance increase also translates into improved downlink SIR performance, allowing a DOA-based downlink beamforming method (Pseudoinverse DOA method) to work comparably to spatial signature based methods. This work showed how off-line calculations using basic electromagnetic computations could lead to significant improvements in smart antenna system performance.

VI. References

[1] B. Friedlander and A. Weiss, "Direction finding in the presence of mutual coupling," *IEEE Trans. Antennas Propagat.*, vol. AP-39, pp. 273-284, March 1991.

[2] J. Pierre and M. Kaveh, "Experimental performance of calibration and direction finding algorithms," *Proceedings of ICASSP 1991*, pp. 1365-1368, 1991.

[3] C. See, "A method for array calibration in parametric sensor array processing," *Proceedings of ICCS 1994*, pp. 915-919, 1994.

[4] C. See, "Sensor array calibration in the presence of mutual coupling and unknown sensor gains and phases," *Electronics Letters*, vol. 30, pp. 373-374, March 1994.

[5] A. Lemma, E. Deprettere, and A. van der Veen, "Experimental Analysis of Antenna Coupling for High-Resolution DOA Estimation Algorithms," *1999 IEEE 2nd Workshop on Signal Processing Advances in Wireless Communications*, pp. 362-365, July 1999.

[6] I. Gupta and A. Ksienski, "Effect of Mutual Coupling on the Peformance of Adaptive Arrays," *IEEE Trans. on Antennas and Propagat.*, vol. AP-31, no. 5, Sept. 1983.

[7] K. Pasala and E. Friel, "Mutual Coupling Effects and Their Reduction in Wideband Direction of Arrival Estimation," *IEEE Trans. on Aerospace and Electronic Systems*, vol. 30, no. 4, Oct. 1994.

[8] T. Svantesson, *Direction Finding in the Presence of Mutual Coupling,* Chalmers University of Technology Technical Report No. 307L, 1999.

[9] T. Su, K. R. Dandekar, and H. Ling, "Simulation of Mutual Coupling Effect in Circular Arrays for Direction Finding Applications," To appear in *Microwave and Optical Technology Letters,* Sept. 2000.

[10] R. Adve and T. Sarkar, "Compensation for the Effects of Mutual Coupling on Direct Data Domain Adaptive Algorithms," vol. AP-48, no. 1, Jan. 2000.

[11] C. Balanis, Antenna Theory: Analysis and Design 2nd Edition, Wiley & Sons, New York, 1998.

[12] A. Paulraj and T. Kailath, "Direction of arrival estimation by eigenstructure method with unknown sensor gain and phase," *Proceedings of ICASSP 1998*, pp. 640-643, March 1985.

[13] H. Krim and M. Viberg, "Two Decades of Array Signal Processing Research: The Parametric Approach," *IEEE Signal Processing Magazine*, pp. 67-94, July 1996.

[14] S. Jeng, G. Okamoto, G. Xu, H.-P. Lin, and W.J. Vogel, "Experimental Evaluation of Smart Antenna System Performance for Wireless Communications," *IEEE Transactions on Antennas and Propagation*, vol. 46, no. 6, pp. 749-757, June 1998.

[15] K. Dandekar, *Space division multiple access systems: Using ray tracing for vector channel propagation study*, Univ. of Texas at Austin M.S. Thesis, 1998.

[16] G. J. Burke and A. J. Poggio, "Numerical Electromagnetics Code (NEC)-method of moments," Technical Document 11, Naval Ocean Systems Center, San Diego, Calif., Jan. 1981.

[17] S. Jeng, G. Xu, H.-P. Lin, and W.J. Vogel, "Experimental Studies of Spatial Signature Variation at 900 MHz for Smart Antenna Systems," *IEEE Transactions on Antennas and Propagation*, vol. 46, no. 7, pp. 953-962, July 1998.

VII. Figures and Tables

Position	Approximate Angular Position*
Stationary User	29°
Position 1	42°
Position 2	48°
Position 3	65°
Position 4	78°
Position 5	97°

Table 1 – Signal Generator Positions

* Measured using average of compensated and uncompensated uplink spatial spectra of signal generator transmitting alone

Trial	User 1 Uncomp PseDOA Method (dB)	User 1 PseSS Method (dB)	User 2 Uncomp PseDOA Method (dB)	User 2 PseSS Method (dB)
1	0.93	0.17	-0.82	0.76
2	4.48	0.22	4.71	1.08
3	2.73	0.46	0.65	0.45
4	3.06	0.29	3.60	0.71
5	3.33	-0.12	25.67	-0.74

Table 2 – Compensated PseDOA Method Improvement between Stationary User (User 1) and User 2 (at each of 5 tested positions)

Trial	User 1 Comp SIR (dB)	User 1 Uncomp SIR (dB)	User 2 Comp SIR (dB)	User 2 Uncomp SIR (dB)
1	19.68	23.70	22.39	25.16
2	21.59	14.45	23.19	23.62
3	22.59	26.57	23.38	22.86
4	21.38	16.36	23.93	12.36
5	23.98	14.15	22.51	-10.48

Table 3 – PseDOA Method SIR Improvement between Uncompensated and Compensated Calculations

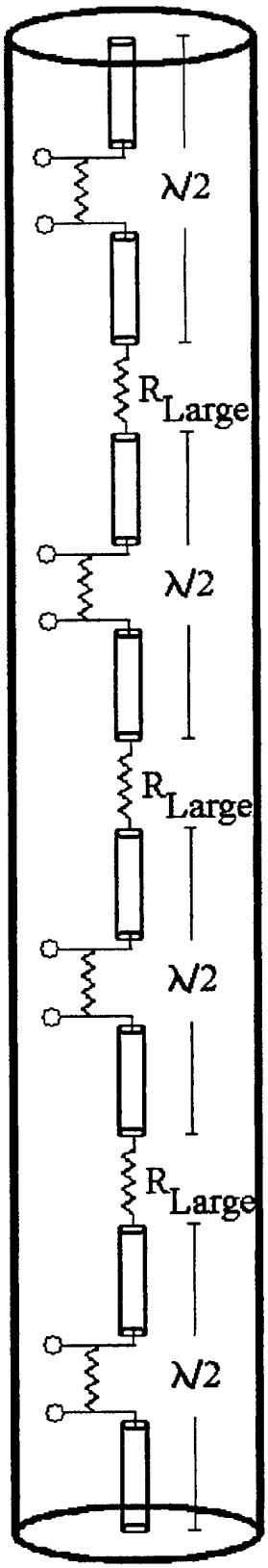

Figure 1 – Collinear Dipole Antenna Array Element

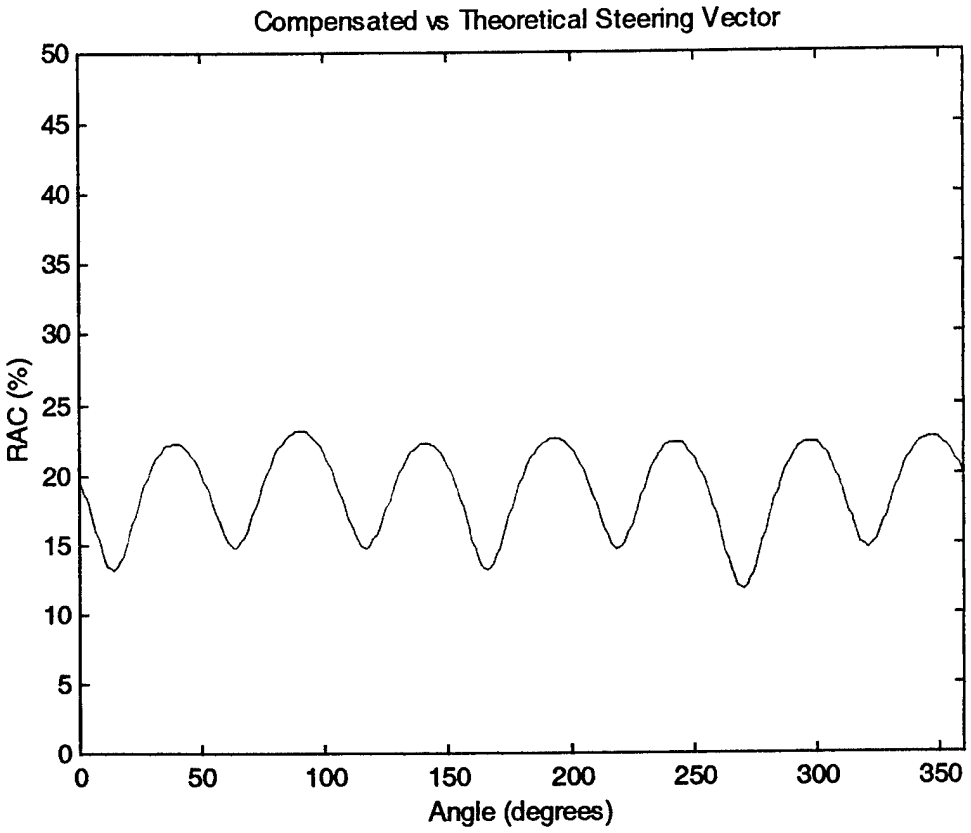

Figure 2 – Compensated vs Theoretical Steering Vector RAC

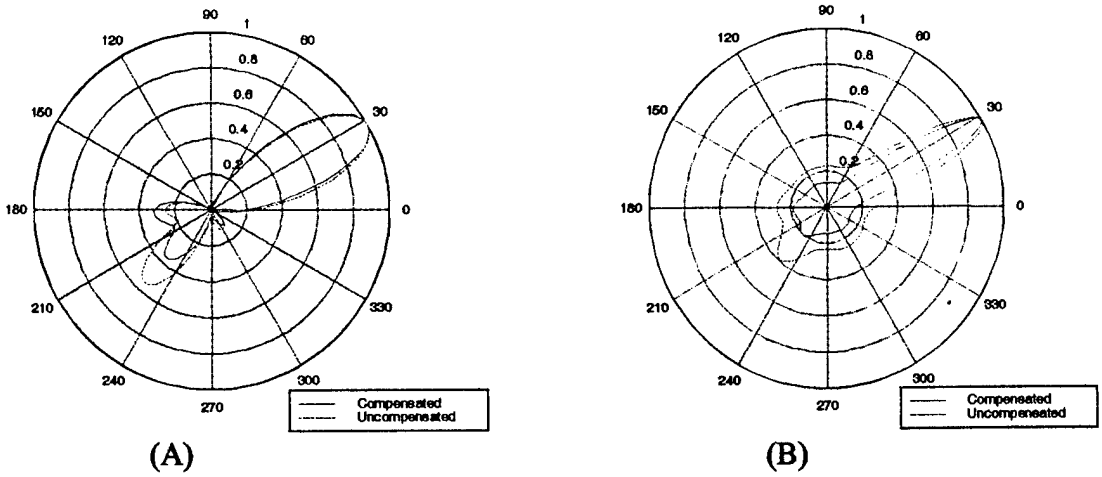

Figure 3 – Experimental Data Stationary User Spatial Spectra – (A) Bartlett DOA Algorithm (B) MUSIC DOA Algorithm

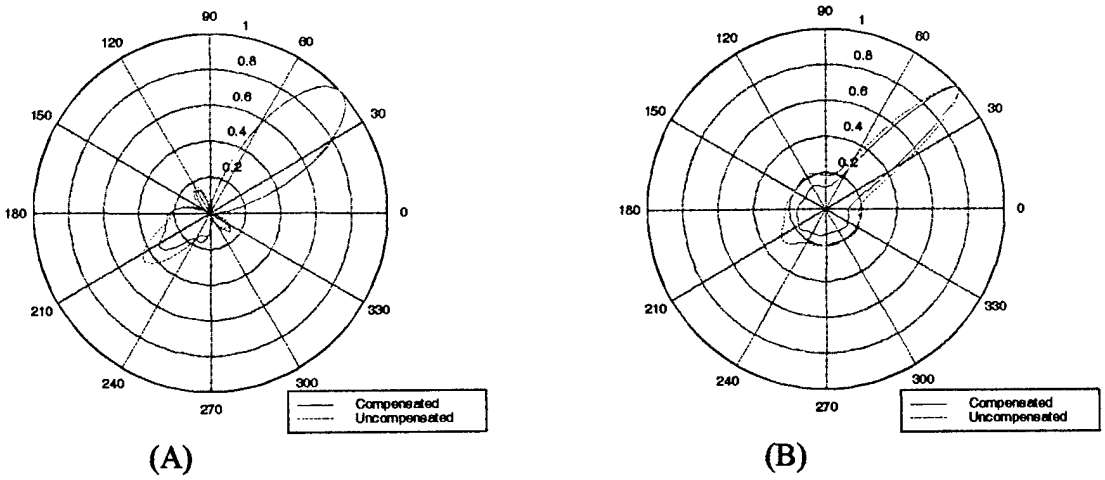

Figure 4 – Experimental Data Mobile Position 1 Spatial Spectra - (A) Bartlett DOA Algorithm (B) MUSIC DOA Algorithm

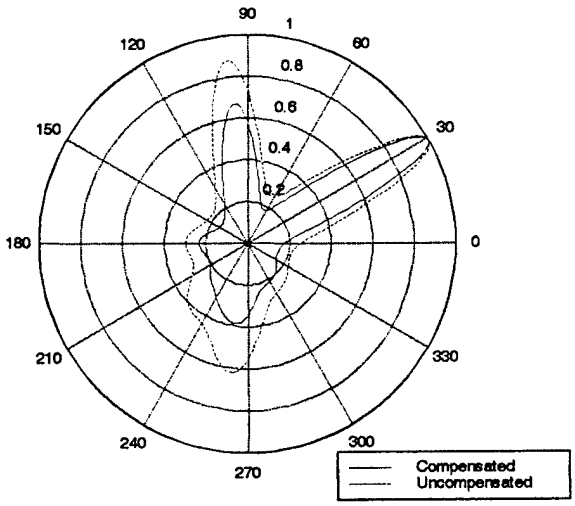

Figure 5 – Experimental Data Multiuser MUSIC Spatial Spectra – Stationary User & Mobile Position 5

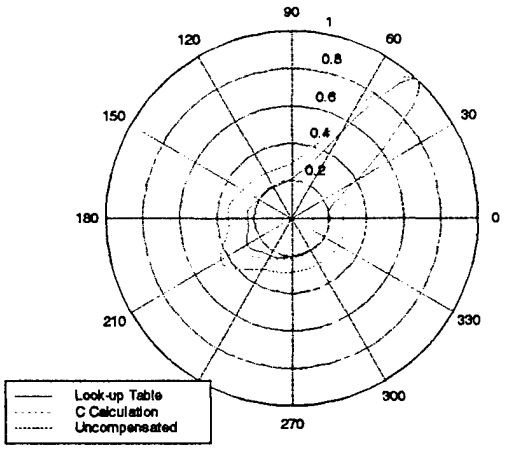

Figure 6 – Compensation Technique Effect – Stationary User Spatial Spectra

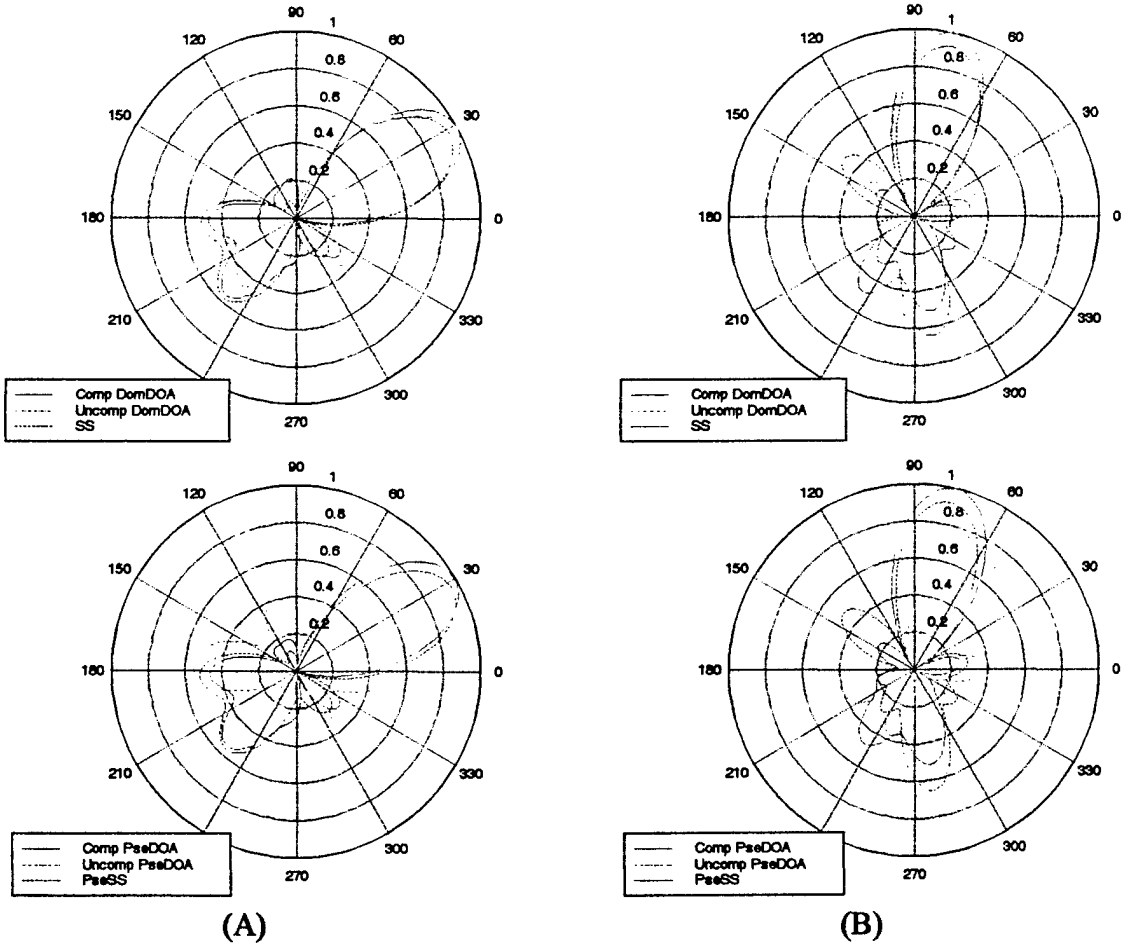

Figure 7 – Downlink Beamforming Spectra for (A) Stationary User and (B) User at Position 4

AN EFFICIENT PRECONDITIONER FOR ELECTROMAGNETIC INTEGRAL EQUATIONS USING PRE-DEFINED WAVELET PACKET BASIS

Hai Deng* and Hao Ling**

*Department of Electrical Engineering
University of New Orleans
New Orleans, LA 70148

**Department of Electrical and Computer Engineering
The University of Texas at Austin
Austin, TX 78712-1084

ABSTRACT — An approximate-inverse preconditioner based on the pre-defined wavelet packet (PWP) basis is proposed for the fast iterative solution of electromagnetic integral equations. The PWP basis is designed to achieve a sparse representation of the moment matrix and the preconditioner is constructed by inverting the block-diagonal approximation of the PWP-based moment matrix and transforming the results into the space domain. Numerical results show that the PWP preconditioner is effective in accelerating the convergence rate of iterative solution to moment equations. It is also demonstrated that by properly designing the block-diagonal matrix and computing the matrix elements, the total computational complexity and memory costs for the preconditioner can be kept to O(NlogN).

Index Terms — Computational Electromagnetics, Preconditioning, Wavelet Packet Basis.

I. Introduction

Iterative algorithms are commonly used to solve large-scale moment equations resulting from electromagnetic integral equations. The computational cost of iterative solution is proportional to both the moment matrix-vector multiplication operation and

the number of iterations required for a convergent solution. The multilevel fast multipole method (MLFMM) has been developed to reduce the time complexity and memory of the dense matrix-vector multiplication operation from $O(N^2)$ to O(NlogN) [1-3]. However, the total solution time remains dependent on the number of iterations required to achieve an accurate solution. If the scatterer contains near-resonant structures such as deep cavities, the moment matrix is not well conditioned and the convergence rate of the iterative solution can become very slow [4, 5]. In these cases, a preconditioning matrix **[P]** is desired to accelerate the convergence rate. We consider a left-preconditioning system:

$$\mathbf{[P][Z]\,J = [P]\,E} \tag{1}$$

where **[Z]** is the moment matrix, **J** is the unknown induced current vector and **E** is the excitation vector. To achieve the best preconditioning, **[P]** should be as close to the inverse of **[Z]** as possible. Hence, **[P]** is called an approximate-inverse preconditioner. In this work, we set out to construct an approximate-inverse preconditioner **[P]** that satisfies the following conditions:

(a) **[P]** is an accurate approximation to $\mathbf{[Z]}^{-1}$ to be an effective preconditioner.

(b) The total computational complexity and memory requirement to construct the preconditioner are of *O*(NlogN).

(c) The total computational complexity and memory requirement to implement the preconditioning operation in (1) are of *O*(NlogN).

Conditions (b) and (c) are set to keep the complexity of the preconditioning on par with that of the MLFMM, making our preconditioner applicable for the MLFMM. The traditional preconditioning methods, such as incomplete LU factorization (ILU),

Frobenius-norm-based approximate inverse and polynomial preconditioners could be effective [6, 7]. But they are computationally too complicated to meet conditions (b) and (c). In [5], an approximate-inverse preconditioner was constructed by inverting a block-banded form of the original moment matrix. Low complexity was maintained by choosing a bandwidth that is independent of problem size.

Our approach to the problem is to derive an effective preconditioner meeting conditions (a)-(c) based on the wavelet packet basis. With the conventional subsectional basis, [**Z**] in (1) is dense, making it difficult to find an effective approximate-inverse preconditioner. However, if we can transform the moment equation to a new basis to make the transformed moment matrix sparse and diagonal dominant, it will be much easier to find an effective preconditioner. We have recently proposed the Pre-defined Wavelet Packet (PWP) basis for the efficient representation of moment matrices [8, 9]. The PWP basis was designed to match the oscillatory nature of the Green's kernel in the integral equation. Numerical results showed that the PWP-transformed moment matrices are strongly diagonal dominant, and have about O(NlogN) non-zero elements for large-scale problems. In [10], a preconditioner for the PWP-transformed moment matrix was constructed to accelerate the convergence of the transformed matrix equation. In this paper, we shall demonstrate that an effective approximate-inverse preconditioner in the space domain can be derived from the PWP basis with no more than O(NlogN) computational or memory cost. It is worthwhile to point out that there have been some recent works on using the conventional wavelet transform to precondition linear systems for iterative solutions [11-14]. However, the requirements for computational cost and memory are at least $O(N^2)$ to implement the wavelet transform and the preconditioning

operation. In this work, we overcome the $O(N^2)$ complexity and memory bottlenecks by computing the PWP preconditioner directly from the PWP basis functions [9].

This paper is organized as follows. In Section II, we give a brief review of the PWP basis and its representation of the moment matrices. In Section III, we describe the design and construction of our approximate-inverse preconditioner in the space domain from the sparse PWP-based moment matrix. We show that the total cost for the construction and preconditioning operation can be kept under $O(N\log N)$. Numerical results are presented in Section IV. Finally we draw some conclusions in Section V.

II. PWP Basis and Its Representation of Moment Equations

Wavelet packet basis is a set of orthonormal functions derived from the shift and dilation of a basic wavelet function, and can be considered as a generalization of the conventional wavelet basis [15]. From the point of view of function space decomposition, the wavelet packet basis space is generated from the decomposition of both the scaling function space and the corresponding wavelet function space. Let us assume that $\psi(x)$ is the wavelet packet basis function with the finest spatial resolution available for signal representation. Using the "two-scale equations," we can express the wavelet packet basis functions in the next scale as [16]:

$$\begin{aligned} \psi_0^1(n) &= \sum_k \psi(k) h(2n-k) \\ \psi_1^1(n) &= \sum_k \psi(k) g(2n-k) \end{aligned} \qquad (2)$$

where $\{h(k)\}$ and $\{g(k)\}$ are the impulse responses of two quadrature filters H (low-pass) and G (high-pass), respectively. The functions in the next scale become coarser in spatial resolution and finer in spectral resolution after the filtering and down-sampling in (2).

The same procedure can be applied recursively to the outputs of (2) into subsequent scales. Conversely, the decomposition results in (2) can also be used to reconstruct the original sequence by using another pair of quadrature filters P and Q, which are the mirror filters of H and G, respectively. This reconstruction procedure can be expressed as:

$$\psi(x) = \sum_k p(x-2k)\psi_0^1(k) + \sum_k q(x-2k)\psi_1^1(k) \qquad (3)$$

where {p(k)} and {q(k)} are the impulse responses of P (low-pass) and Q (high-pass), respectively. The functions become finer in spatial resolution and coarser in spectral resolution through filtering and up-sampling in (3).

A complete and orthogonal wavelet packet basis can be generated from a spectral decomposition tree that starts from an initial mother function $\psi(x)$ with the finest spatial resolution by using recursive two-channel filtering and down-sampling in (2). It can be shown that the decomposed functions at the outermost branches of the tree satisfy orthogonality and completeness for any decomposition trees, and thus constitute a wavelet packet basis set [17]. In this context, the conventional wavelet transform (CWT) basis can be considered as a special case of the wavelet packet basis when the decomposition tree grows along only the lowest frequency branch. However, we have shown in [18] that the structure of the CWT tree is not optimal for representing the moment matrix from electrodynamic integral equations. Instead, we have proposed a special wavelet packet tree for electrodynamic problems [8, 9,]. This class of wavelet packet bases, which we term the pre-defined wavelet packet (PWP) basis, has a spectral decomposition tree that zooms in along the free-space wave number k_0. The motivation for this tree structure is to ensure that the basis is well-matched to the oscillatory nature

of the Green's function kernel in the integral equation. Figs. 1(a) and 1(b) show respectively the conventional wavelet decomposition tree and the PWP decomposition tree for N=32. In the PWP tree, the center frequency of its deepest branch is as close as possible to k_0. Detailed discussion on the construction of the PWP basis can be found in [9].

Once the PWP basis is defined, it is straightforward to transform the original moment equation into the new basis representation as follows:

$$[\tilde{\mathbf{Z}}]\tilde{\mathbf{J}} = \tilde{\mathbf{E}} \tag{4}$$

where

$$[\tilde{\mathbf{Z}}] = [\mathbf{M}]^T[\mathbf{Z}][\mathbf{M}] \tag{5}$$

$$\tilde{\mathbf{J}} = [\mathbf{M}]^T\mathbf{J} \tag{6}$$

$$\tilde{\mathbf{E}} = [\mathbf{M}]^T\mathbf{E} \tag{7}$$

$[\mathbf{M}]^T$ denotes the transpose of $[\mathbf{M}]$, and is the PWP transformation matrix. It changes the original expansion/testing functions from the standard subsectional bases into the PWP bases. Note that $[\mathbf{M}]^T$ is equal to $[\mathbf{M}]^{-1}$ since $[\mathbf{M}]$ is an orthonormal transformation. $[\tilde{\mathbf{Z}}]$, $\tilde{\mathbf{J}}$, and $\tilde{\mathbf{E}}$ are the moment matrix, induced current, and excitation vector represented in the PWP basis, respectively. Our numerical results from [9] showed that the transformed moment matrix under the PWP basis is very sparse. In particular the number of above-threshold elements in the transformed moment matrix grows at a rate of $O(N^{1.3})$ for small-sized problems, and approaches $O(N\log N)$ for large-scale problems. Furthermore, the significant elements in $[\tilde{\mathbf{Z}}]$ are located mainly along the diagonal or near-diagonal positions. Unfortunately, the exact locations of the significant elements are difficult to predict. Consequently, the complexity of the algorithm in solving the complete moment equation is still hampered by an N^2 computational bottleneck, since

every element of the matrix must be computed to determine whether it is small enough to be discarded. However, for the proposed preconditioning application in this paper, we shall show in the next section that an effective approximate-inverse preconditioner can be constructed by computing only those elements within the diagonal blocks.

III. PWP-Based Approximate-Inverse Preconditioner in the Space Domain

We will first outline our approach to constructing the PWP-based preconditioner. Since the PWP transformed moment matrix $[\tilde{\mathbf{Z}}]$ is very sparse and diagonal dominant, we approximate $[\tilde{\mathbf{Z}}]$ by a block-diagonal matrix $[\tilde{\mathbf{Z}}_{bd}]$ that consists of the near-diagonal terms of $[\tilde{\mathbf{Z}}]$. The approximate-inverse preconditioner $[\mathbf{P}]$ defined in (1) is then constructed by inverting the block-diagonal matrix $[\tilde{\mathbf{Z}}_{bd}]$ and transforming the resulting matrix back to the space domain:

$$[\mathbf{P}] = [\mathbf{M}]\,[\tilde{\mathbf{Z}}_{bd}]^{-1}\,[\mathbf{M}]^{T} \tag{8}$$

Therefore, the preconditioned moment equation becomes:

$$[\mathbf{M}]\,[\tilde{\mathbf{Z}}_{bd}]^{-1}\,[\mathbf{M}]^{T}[\mathbf{Z}]\,\mathbf{J} = [\mathbf{M}]\,[\tilde{\mathbf{Z}}_{bd}]^{-1}\,[\mathbf{M}]^{T}\mathbf{E} \tag{9}$$

The inverse of the block diagonal matrix $[\tilde{\mathbf{Z}}_{bd}]$ is simply the inverse of its individual diagonal blocks, and the inverted matrix $[\tilde{\mathbf{Z}}_{bd}]^{-1}$ remains block diagonal. By properly choosing the block sizes of $[\tilde{\mathbf{Z}}_{bd}]$, we can limit the computational cost of the inversion while maintaining the effectiveness of the preconditioner.

The actual implementation of the preconditioner will now be considered. If we solve equation (9) using an iterative algorithm such as the conjugate gradient method, the complexity of each iteration is proportional to that of the product between the matrix $[\mathbf{M}]$, $[\tilde{\mathbf{Z}}_{bd}]^{-1}$, $[\mathbf{M}]^{T}$ or $[\mathbf{Z}]$ and a vector. The product $[\mathbf{Z}]$ and a vector can be implemented

using the MLFMM algorithm with O(NlogN) complexity and memory requirement. Because the PWP transformation matrix $[\mathbf{M}]^T$ has about O(NlogN) non-zero elements, the multiplication of $[\mathbf{M}]^T$ or $[\mathbf{M}]$ with a vector is also of O(NlogN) in complexity. Therefore, if we can limit both the number of non-zero elements in $[\tilde{\mathbf{Z}}_{bd}]^{-1}$ and the complexity of constructing $[\tilde{\mathbf{Z}}_{bd}]^{-1}$ to O(NlogN), the total cost per iteration in (9) will remain at O(NlogN).

Our design of the block-diagonal matrix $[\tilde{\mathbf{Z}}_{bd}]$ is shown in Fig. 2. The blocks are designed so as to capture the most significant elements in the PWP-transformed moment matrix $[\tilde{\mathbf{Z}}]$. The block-diagonal matrix consists of the following: (i) a block centered about the spectral frequency k_0 with block size M_1, (ii) a set of diagonal blocks in the remaining upper-left region with block size M_2, and (iii) a set of diagonal blocks in the lower-right region with block size M_3. The number of diagonal blocks with size M_2 is $[(N/2- M_1)/ M_2]$, and that with size M_3 is $[(N/2)/ M_3]$. The block from (i) is usually the densest part of $[\tilde{\mathbf{Z}}]$, since its elements correspond to the interactions between PWP bases with the longest spatial extent and spectral frequency close to k_0. They tend to have the strongest interaction with each other. The blocks from (iii), on the other hand, are nearly diagonal, since their elements correspond to the interactions between PWP bases with the highest spectral frequency and the shortest spatial extent. Therefore, we generally choose block sizes with $M_1 > M_2 > M_3$. Furthermore, as N is increased we keep the sizes M_2 and M_3 fixed, but let M_1 grow slightly with problem size at a rate of $N^{1/3}$ to capture even more of the dominant elements in $[\tilde{\mathbf{Z}}]$. This growth rate is chosen to ensure that the cost of inverting the block remains bounded by N, as the cost of the inversion is proportional to the cube of the matrix dimension. The inverse of $[\tilde{\mathbf{Z}}_{bd}]$ is equivalent to the inverse of

each of the blocks of $[\tilde{\mathbf{Z}}_{bd}]$ in Fig. 2. Therefore, under our construct, the total computational complexity to invert $[\tilde{\mathbf{Z}}_{bd}]$ is proportional to N and the resulting number of nonzero elements in $[\tilde{\mathbf{Z}}_{bd}]^{-1}$ is also proportional to N.

Next, we discuss the computation of the required elements in $[\tilde{\mathbf{Z}}_{bd}]$. Each element $\tilde{\mathbf{Z}}(m, n)$ of the matrix $[\tilde{\mathbf{Z}}]$ can be directly expressed as [9]:

$$\tilde{Z}(m,n) = \sum_i \sum_j \psi_m(i) G(i,j) \psi_n(j) \tag{10}$$

where G(i, j) is the free space Green's function, i and j represent the indices of the discretization grid in the space domain, and ψ_k is the k-th PWP basis function. It can be seen from (10) that the computational complexity for each matrix element is proportional to the product of the spatial supports of the two corresponding basis functions. The support of a PWP basis function is related to the depth of the branch in the PWP decomposition tree. Let us assume that the basis functions corresponding to branches in the first stage of the PWP decomposition tree have spatial support L (i.e., the order of the wavelet filter). The complexity for computing a diagonal (or near-diagonal) element is then L^2. The support of a PWP basis function doubles if it corresponds to the branches on the next deeper stage in the decomposition tree [9, 16]. Therefore, the spatial support of the basis functions generated from the tree branches at stage k is $2^{k-1}L$, and the complexity to compute an element from basis functions in the same stage is $(2^{k-1}L)^2$. Since the maximum possible depth of the wavelet decomposition tree is $K_{max}=\log_2 N$, the cost for computing an element using bases from this maximum depth would then be N^2. However, as we shall discuss in the next section, the best preconditioning performance is often achieved using a tree with depth much less than the maximum possible depth. Similar observation has also been reported in [11]. Therefore, if we impose that the

maximum depth index of the PWP decomposition trees is a small number K, the number of operations needed to compute an element in $[\tilde{\mathbf{Z}}_{bd}]$ will be between L^2 and $4^{K-1}L^2$. With $O(N)$ elements in $[\tilde{\mathbf{Z}}_{bd}]$, the total complexity to compute the matrix $[\tilde{\mathbf{Z}}_{bd}]$ is about $O(N)$ operations.

To summarize, we have designed a preconditioner based on the block-diagonal approximation of the PWP-transformed moment matrix. The steps to construct and carry out the preconditioning operation entail: (i) computing the elements in the diagonal blocks of $[\tilde{\mathbf{Z}}_{bd}]$ one term at a time using (10), (ii) inverting $[\tilde{\mathbf{Z}}_{bd}]$ one block at a time to arrive at its inverse $[\tilde{\mathbf{Z}}_{bd}]^{-1}$, and (iii) carrying out the preconditioning operation by a successive set of sparse matrix-vector multiplication operations in (9). It is shown that the computational complexity of the each of the three steps can be limited to within $O(N\log N)$ operations, thus making the proposed preconditioner compatible with the MLFMM in solving moment equations.

IV. Numerical Results

Two two-dimensional targets, an open-ended inlet and a bent structure shown in Fig. 3, are chosen to test our PWP preconditioner. With a large depth-to-opening ratio (l/m), the moment matrices from the scatterers are ill-conditioned, and the convergence rate is slow if an iterative solver is used to solve the systems. For the inlet structure, if the thickness parameter t is equal to zero, the electric field integral equation (EFIE) is use to construct the moment equation. Otherwise, the combined field integral equation (CFIE) is used. For the bent structure, EFIE is always used to find the solution. The discretization of the structure is chosen to be fixed at 0.1 wavelength while the electrical

size of the structure is varied. In all cases the incident plane wave is E-polarized and makes an angle of 45° with respect to the inlet opening.

Fig. 4 is the moment matrix $[\tilde{\mathbf{Z}}]$ represented by the PWP basis for the inlet structure with dimensions l:m:t=15:1:1 and N=256. It is shown in logarithmic scale without any thresholding. We find that the most significant elements in the transformed matrix match the patterns we chose for the PWP preconditioner in Fig. 2. The densest portion of the matrix is located in the upper left region, with the strongest elements near the k_0 spectral position. The wavelet filter used to generate the PWP basis functions is Daubechies filter with order 16 (with 7 vanishing moments).

We use both the conjugate-gradient squared (CGS) method and the biconjugate gradient stabilized (BiCGSTAB) method. Both of them are effective iterative solvers for linear equations with nonsymmetric coefficient matrix [19]. CGS is used in most of the cases in this work since it converges faster than BiCGSTAB. However, we use the BiCGSTAB to compare the detailed convergence rates of the different preconditioners, as the convergence behavior of the CGS is not very smooth. In the application of the iterative solvers, the initial current guess is $\mathbf{J}_0$=0, and the stopping criterion used is when the relative residual error $\|r_n\|/\|r_0\| \le 10^{-6}$, where $r_n = \mathbf{E}\text{-}[\mathbf{Z}]\mathbf{J}_n$ and $r_0 = \mathbf{E}$.

We first examine how the iteration number changes as the electrical size of the scatterer is increased in the following three cases:

Case 1: The scatterer is the inlet structure shown in Fig. 3(a) with t = 0 and l:m=15:1. The moment equation is formulated with the EFIE. For the PWP preconditioner, we choose M_2=32, M_3=1, and M_1 grows at a rate of $\sqrt[3]{N}$ starting from 32 at N=128.

Case 2: The scatterer is the inlet structure with l:m:t=15:1:1. The moment equation is formulated with the CFIE. The PWP preconditioner is constructed the same way as that in Case 1.

Case 3: The scatterer is the bent structure shown in Figure 3(b) with l:m=12:1. The EFIE is used, and the parameters for the PWP preconditioner are chosen as: M_2= M_3= 32, and M_1 grows at a rate of $\sqrt[3]{N}$ starting from 32 at N=128.

The iteration numbers required versus problem sizes are shown in Figs. 5(a)-(c) for Cases 1-3, respectively. We increase the problem size by proportionally increasing the electrical size of the scatterer while keeping the discretization interval fixed at 0.1 wavelength. The results for the moment equation without any preconditioning and that with the PWP preconditioner are plotted. For comparison, we also show the results from a simple block-diagonal preconditioner in the space domain. It is constructed by inverting the block-diagonal form of the original space-domain moment matrix. The block sizes are uniform and the total number of non-zero elements is kept the same as that used in the PWP preconditioner. We find that the iteration number grows very rapidly with the problem size if no preconditioning is applied. With the PWP preconditioners applied, the iteration numbers are significantly reduced and they increase much more slowly with problem size. Furthermore, the PWP preconditioner performs better than the equivalent space domain preconditioner. This is because the PWP preconditioner captures more of the energy in the original moment matrix. Note that the CFIE results shown in Fig. 5(b) have smaller iteration numbers than the results from the EFIE cases shown in Figs. 5(a) and 5(c). However, the effectiveness of the PWP preconditioner is still apparent. In Fig. 5(c), we also plot the results using the

conventional wavelet transform (CWT) basis instead of the PWP basis. The CWT preconditioner is constructed in exactly the same way as the PWP preconditioner, except the approximate matrix is formed from the elements of the CWT transformed moment matrix rather than the PWP transformed one. We observe that the PWP preconditioner outperforms the CWT preconditioner since the PWP basis can more efficiently represent the moment matrix. Although not shown, similar comparisons between the PWP and CWT preconditioners are also found for Cases 1 and 2.

Figs. 6(a)-(c) show the convergence behaviors for a fixed problem size (N=512) for Cases 1-3, respectively. The BiCGSTAB algorithm is used as the iterative solver. In each figure, the residual error is plotted as a function of the number of iterations for the moment equation without any preconditioning, with the space domain and/or the CWT preconditioner, and with the PWP preconditioner. We observe that, with the PWP preconditioning, the relative residue decreases the fastest. In addition, the convergence behaviors are more stable. Similar convergence behaviors are found for larger problem sizes.

Next, we investigate the effect of the depth index K in the wavelet tree on the resulting PWP preconditioner. For a scattering problem with a problem size of N, the maximum depth index for the PWP decomposition tree is ($\log_2 N$). However, this does not necessarily lead to the best preconditioning performance. Fig. 7 plots the required iteration number versus the depth index K used in constructing the PWP preconditioner for N=1024. The results show that the curves flatten considerably after K=5, implying that there is not much to be gained beyond this depth in the wavelet tree. The reason for this phenomenon is because although the maximum-depth PWP tree generates the

sparsest transformed moment matrix [9], the long PWP basis functions resulting from that tree shift some of the energy into the non-diagonal blocks, making the preconditioning results worse. For the problem sizes we have studied from 128 to 4096, the optimal PWP tree depths are usually between 3 and 6. Since the computational cost of constructing the preconditioner is proportional to the maximum depth of the PWP decomposition tree, we should not go beyond this depth when constructing the PWP preconditioner.

Finally, we examine the computational cost of the PWP preconditioner. Fig. 8 shows the CPU running time required to generate the PWP preconditioning matrix $[\tilde{\mathbf{Z}}_{bd}]$ for Case 1 versus problem size N. The direct element computation in equation (10) is carried out and the PWP tree depth K is increased slightly from 3 to 6 as the problem size is changed from 128 to 4096. Fig. 9 shows the CPU running time needed to implement the multiple matrix-vector products required for the carrying out the PWP preconditioning in (9). We exclude the time needed for the first moment matrix and vector product in (9), as that operation can be done via the MLFMM. We find that the CPU running time grows at rate close to O(NlogN) in the both cases. This is consistent with the estimates given in Section III and meets the objectives we have set forth for the preconditioner.

V. Conclusions

A preconditioner for the moment equation based on the pre-defined wavelet packet basis has been proposed in this paper. Due to the vanishing moments of wavelet basis functions, the PWP-based moment matrix is sparse and diagonally concentrated.

Consequently, an approximate-inverse preconditioner can be more easily designed and constructed than that based on the original space-domain moment matrix. The PWP preconditioner is constructed by inverting a block-diagonal form of the PWP-based moment matrix and transforming the resulting matrix back into the space domain. It has been shown that the complexity for the construction and preconditioning operation can be kept under O(NlogN) in both computational cost and memory requirement. Our numerical results showed that the iteration numbers for the PWP-preconditioned moment equations are significantly smaller and grow at a lower rate than those without preconditioning or preconditioned using a space-domain preconditioner. In addition, the PWP preconditioner also performed better than the equivalent preconditioner derived from the conventional wavelet basis. We should point out that in this paper the PWP algorithm is implemented only for two-dimensional problems. Its further extension to three-dimensional (3-D) problems is still under investigation, with the goal of combining the preconditioner with the 3-D MLFMM to obtain solutions of large-scale problems.

Finally, although we have chosen the block-diagonal matrix as the underlying structure of our approximate-inverse preconditioner, we have found that a block-banded matrix [5] or a thresheld transformed matrix [11, 20] gave better preconditioning results than the block-diagonal form. However, the inverses of those matrices are dense, resulting in $O(N^2)$ computational bottlenecks for implementing the matrix-vector product in the preconditioning step. A worthwhile topic is to find a more effective approximate matrix in the PWP basis domain than the block-diagonal one, while preserving the O(NlogN) total computational cost and memory requirement.

Acknowledgement

The authors thank Prof. Weng Chew for suggesting the idea of preconditioning moment equations using wavelet basis. This work is sponsored by Air Force MURI Center for Computational Electromagnetics under Contract No. AFOSR F49620-96-1-0025, and in part by the Office of Naval Research under Contract No. N00014-01-1-0234.

References

[1] R. Coifman, V. Rokhlin and S. Wandzura, "The fast multipole method for the wave equation: a pedestrian prescription," *IEEE Antennas Propagat. Mag.*, vol. 35, no. 3, pp. 7-12, June 1993.

[2] J. M. Song and W. C. Chew, "Fast multipole method solution using parametric geometry," *Microwave Opt. Tech. Lett.*, vol. 7, pp. 760-765, Nov. 1994.

[3] J. M. Song, C. C. Lu and W. C. Chew, "Multi-level fast-multipole algorithm for electromagnetic scattering for large complex objects," *IEEE Trans. Antennas Propagat.*, vol. 45, pp. 1488-1493, Oct. 1997.

[4] C. C. Lu and W. C. Chew, "A near-resonance decoupling approach (NRDA) for scattering solution of 3D near-resonant structures," *IEEE Trans. Antennas Propagat.*, vol. 45, pp. 808-811, Feb. 1997.

[5] C. H. Ahn., W. C. Chew, J. C. Zhao and E. Michielssen, "Approximate inverse preconditioner for near resonant scattering problems," Research Report, Univ. of Illinois, Apr. 1998

[6] R. Barrett, M. Berry, T. F. Chan, J. Demmel, J. Donato, J. Dongarra, V. Eijkhout, R. Pozo, C. Romine and H. van der Vorst, *Templates for the Solutions of Linear Systems: Building Blocks for Iterative Methods,* SIAM, Philadelphia, 1994.

[7] A. M. Bruaset, *A Survey of Preconditioned Iterative Methods*, John Wiley & Sons, New York, 1995.

[8] H. Deng and H. Ling, "Efficient representation of moment matrix using pre-defined wavelet packet basis," *Electronics Lett.*, vol. 34, pp. 176-177, Mar. 1998.

[9] H. Deng and H. Ling, "On a class of pre-defined wavelet packet basis for efficient representation of electromagnetic integral equations," *IEEE Trans. Antennas Propagat.*, vol. AP-47, pp. 1772-1779, Dec.. 1999.

[10] H. Deng and H. Ling, "Preconditioning of electromagnetic integral equations for iterative solvers using pre-defined wavelet packet basis," *Electronics Lett.*, vol. 35, pp. 1144-1146, July 1999.

[11] T. F. Chan, W. P. Tang and W. L. Wan, "Wavelet sparse approximate inverse preconditioners," *BIT*, vol. 37, pp. 644-660, Sept. 1997.

[12] F. Canning and J. Scholl, "Diagonal preconditioners for the EFIE using a wavelet basis," *IEEE Trans. Antennas Propagat.*, vol. 44, pp.1239-1246, Sept. 1996.

[13] W. L. Golik and D. S. Wang, "Fast wavelet packet algorithm for the combined field integral equation," in *Proc. 13th Annu. Rev. Progress in Applied Comput. Electromagnetics,* Monterey, CA, Mar. 1997.

[14] A. Cohen and R. Mason, "Wavelet methods for second order elliptic problems, preconditioning and adaptivity," preprint, Universit Pierre et Marie Curie, 1998.

[15] C. K. Chui, *An Introduction to Wavelets,* New York: Academic, 1992.

[16] I. Daubechies, *Ten Lectures on Wavelets,* CBMS-NSF Series Applied Math., SIAM, 1991.

[17] M. V. Wickerhauser, *Adapted Wavelet Analysis from Theory to Software*, Wellesley, MA: A. K. Peters, 1994.

[18] H. Deng and H. Ling, "Fast solution of electromagnetic integral equations using adaptive wavelet packet transform," *IEEE Trans. Antennas Propagat.*, vol. 47, pp. 674-682, Apr. 1999.

[19] R. Weiss, *Parameter-Free Iterative Linear Solvers,* Berlin: Akademie Verlag GmbH, 1996.

[20] M. J. Grote and T. Huckle, "Parallel preconditioning with sparse approximate inverses," *SIAM J. Sci. Comput.*, vol. 18, no.3, pp. 838-853, May 1997.

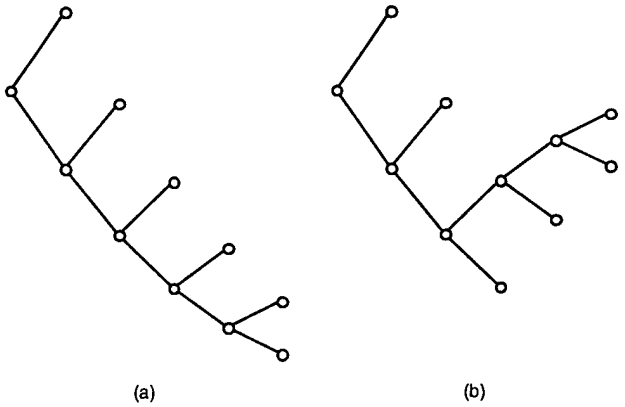

Figure 1. (a) Conventional wavelet decomposition tree;
(b) Pre-defined Wavelet Packet (PWP) decomposition tree.

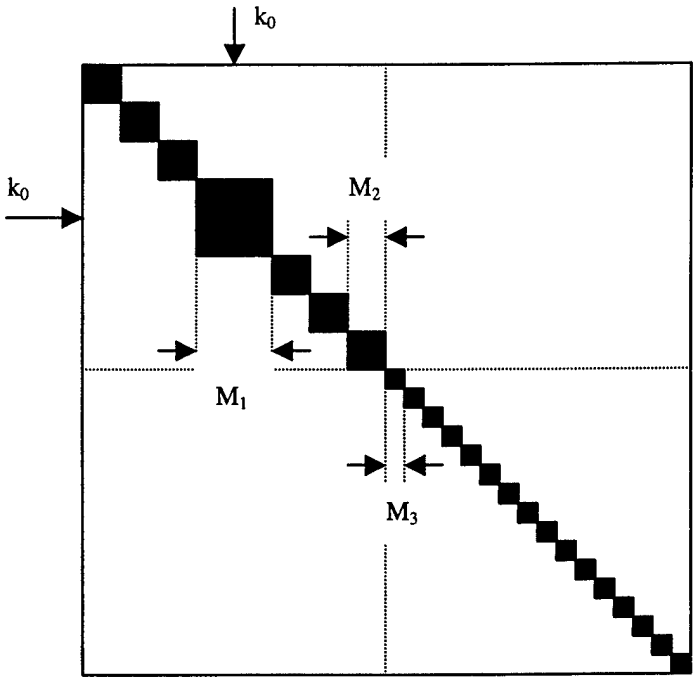

Figure 2. The pattern used to construct $[\tilde{\mathbf{Z}}_{bd}]$ from $[\tilde{\mathbf{Z}}]$.

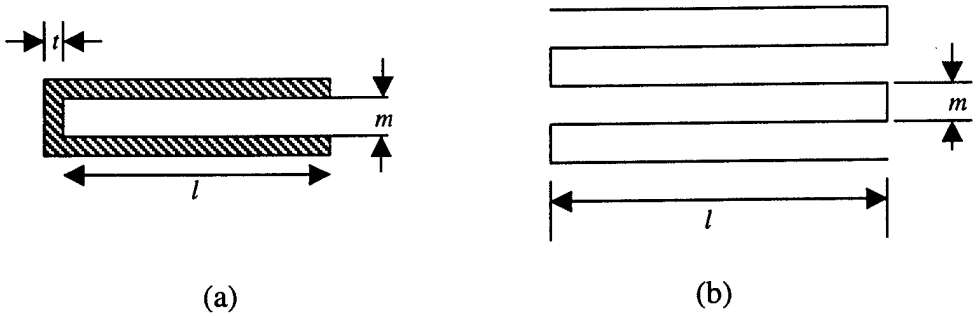

Figure 3. The test scatterers: (a) an open-ended inlet, and (b) a bent structure.

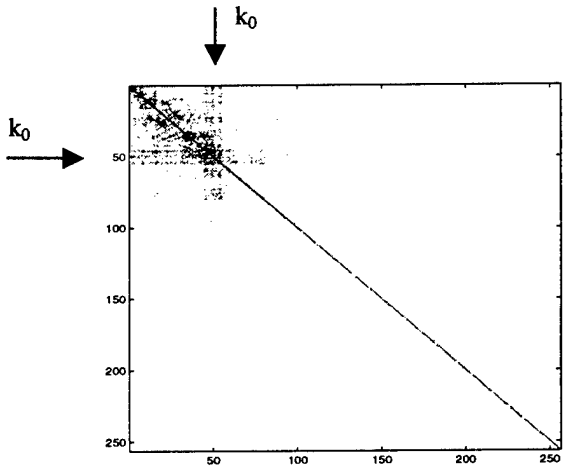

Figure 4. The moment matrix represented by PWP basis, $[\tilde{\mathbf{Z}}]$, for the inlet with N=256 (in logarithmic scale).

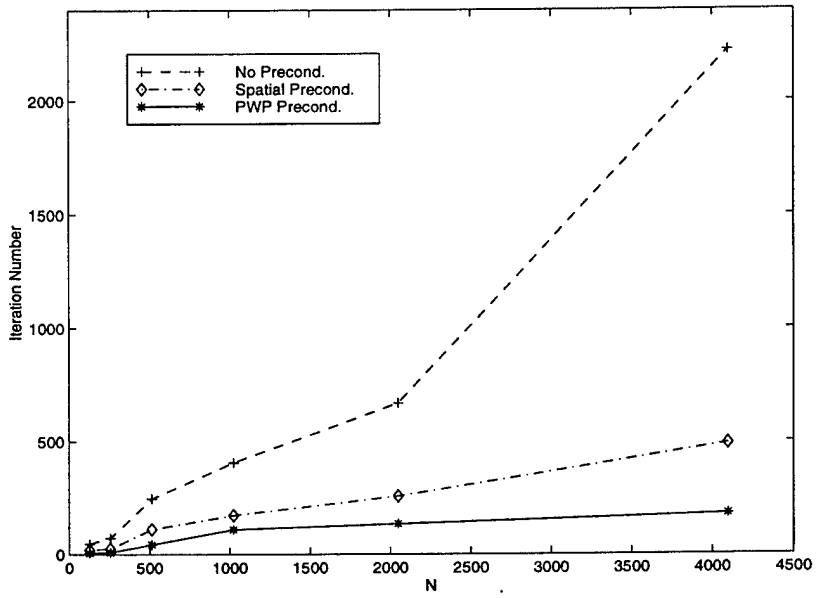
No Precond.
Spatial Precond.
PWP Precond.
Iteration Number
N
0
500
1000
1500
2000
2500
3000
3500
4000
4500

(a)

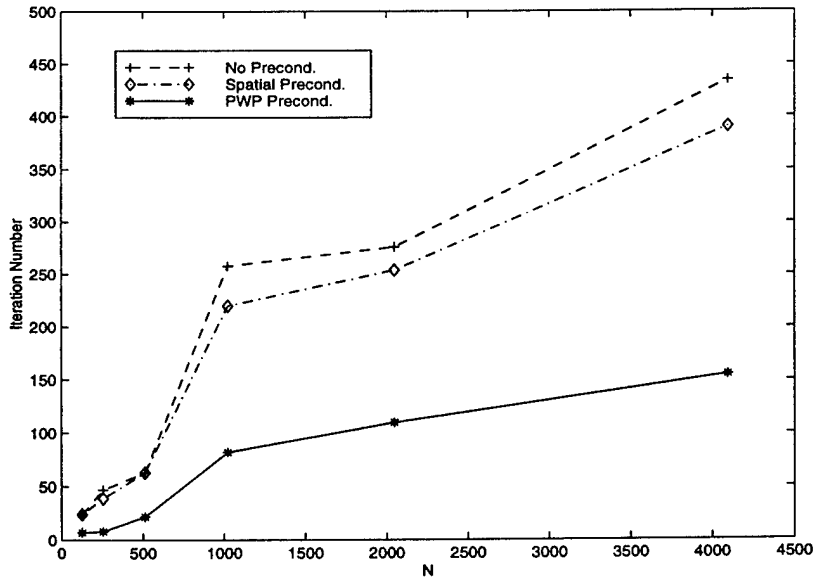
No Precond.
Spatial Precond.
PWP Precond.
Iteration Number
N
0
50
100
150
200
250
300
350
400
450
500
1000
1500
2000
2500
3000
3500
4000
4500

(b)

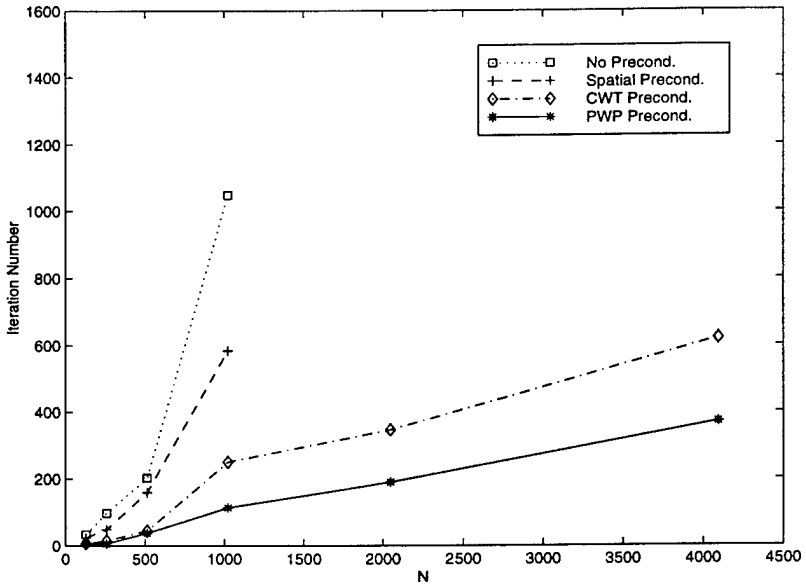

(c)

Figure 5. Iteration numbers vs. problem sizes for solving moment equations with different preconditioning methods for the scattering structures in (a) Case 1, (b) Case 2, and (c) Case 3. The problem sizes are increased by proportionally increasing the scatterer sizes.

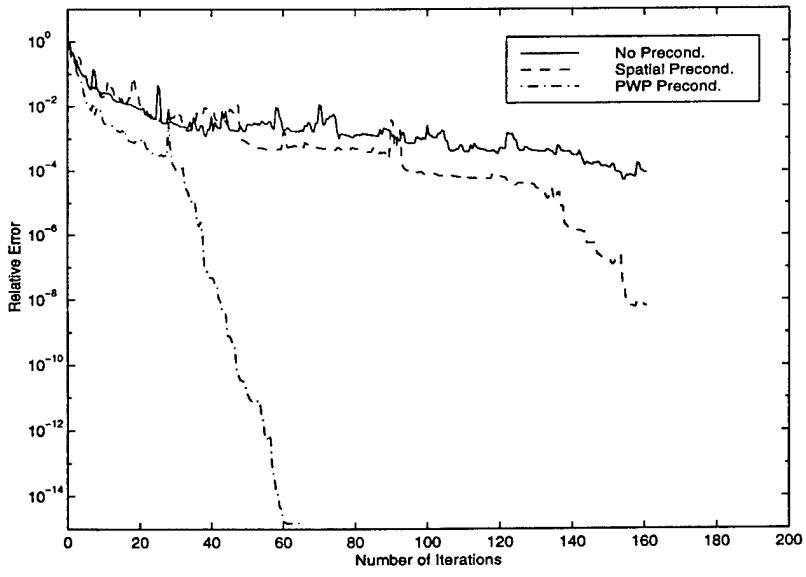

(a)

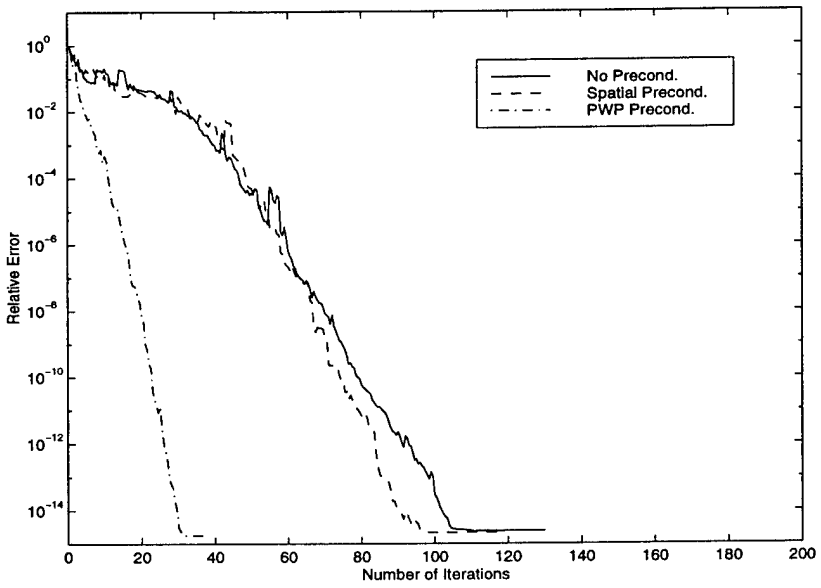

(b)

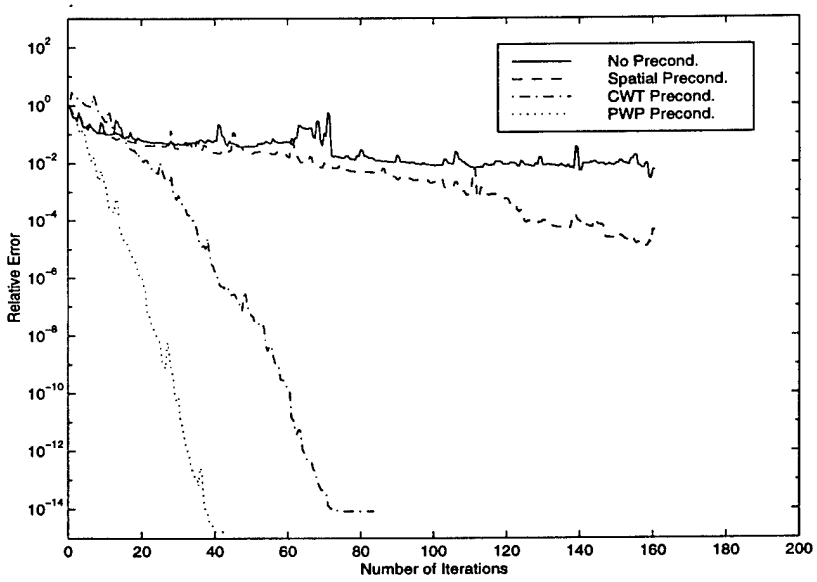

(c)

Figure 6. Convergence behaviors of the preconditioned systems versus iteration numbers for PWP and other preconditioning methods in (a) Case 1, (b) Case 2, and (c) Case 3 with N=512.

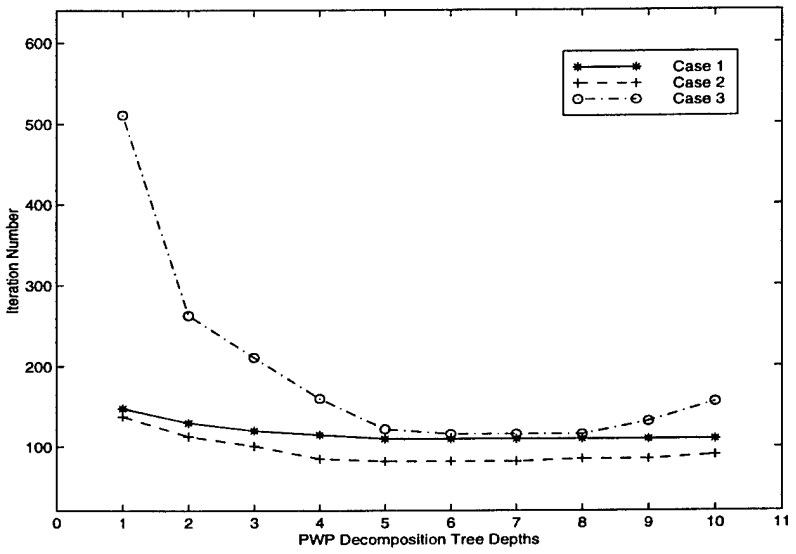

Figure 7. Effect of the PWP decomposition level on iteration number for Cases 1-3 using the PWP preconditioner with N=1024.

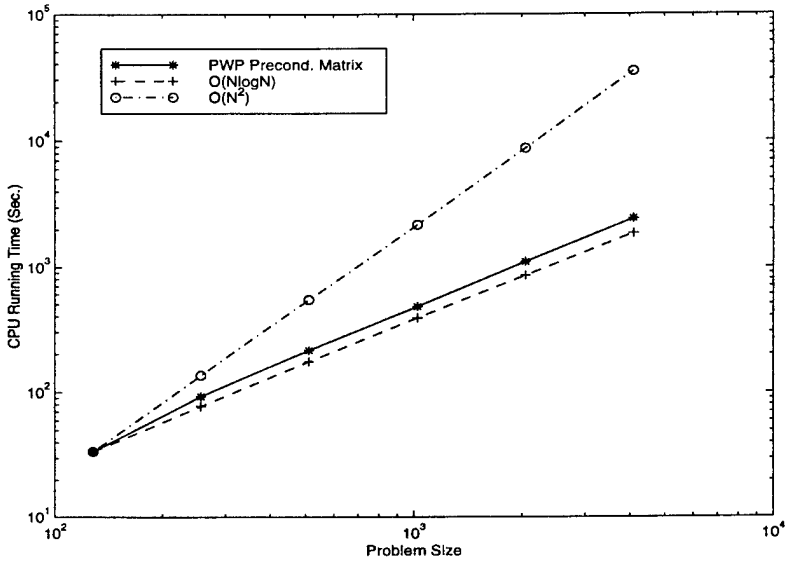

Figure 8. CPU running time vs. problem size for forming the PWP matrix $[\tilde{\mathbf{Z}}_{bd}]$ using (10) for Case 1.

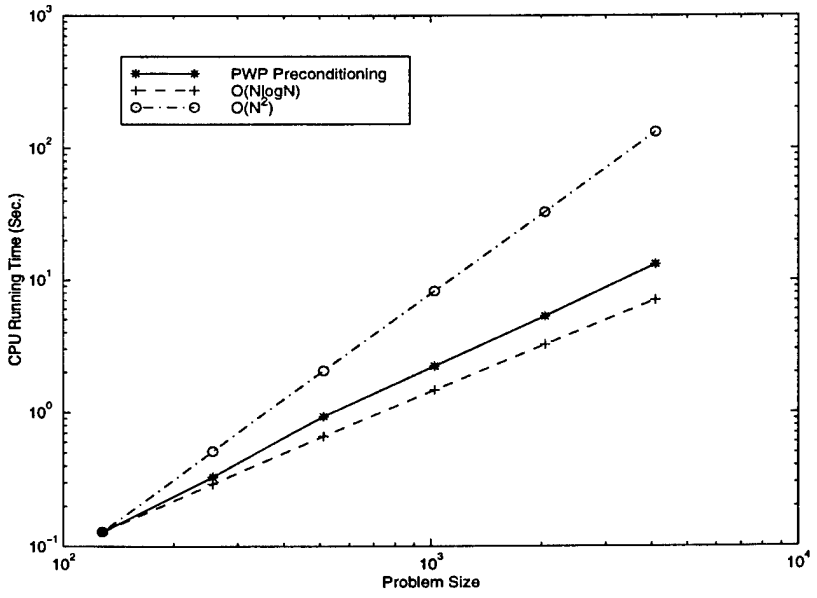

Figure 9. CPU running time vs. problem size for implementing multiple matrix-vector products in (9) for the PWP preconditioning in Case 1.

Paper [25]

Smart Antenna Array Calibration Procedure Including Amplitude and Phase Mismatch and Mutual Coupling Effects

Kapil R. Dandekar, Hao Ling, and Guanghan Xu
University of Texas at Austin, Dept. of Elec. And Comp. Eng.
Engineering Science Building 143
Austin, TX 78712-1084
Phone: 1-512-476-6952
E-mail: (dandekar,ling,xu)@ece.utexas.edu

ABSTRACT

This paper presents a procedure used to calibrate a smart antenna array to compensate for channel amplitude and phase mismatch as well as mutual coupling effects between antenna array elements. A theoretical basis for this calibration procedure in terms of the smart antenna mathematical model is given. Direction of Arrival (DOA) analysis of data collected using the Smart Antenna Testbed at the University of Texas at Austin is presented to illustrate the effectiveness of this calibration procedure and quantify the improvement in system performance. It is shown that amplitude and phase mismatch effects have a much stronger impact on overall system performance compared to mutual coupling between array elements.

I. INTRODUCTION

Smart antenna technology will be an integral component of third generation cellular communications systems. Fully realizing the potential of these systems requires effective array calibration. Array calibration is necessary to compensate for various non-ideal array effects including:

- Amplitude and phase mismatch between physical antenna element hardware
- Amplitude and phase mismatch between element cabling
- Mutual coupling effects
- Tower effects
- Imperfect knowledge of element locations

In the literature there are generally two kinds of calibration techniques. The first type of method uses signals from known directions transmitted on-site to the antenna array being calibrated and then analyzes the array output [1-3]. Conceptually, these techniques address each of the above issues. However, in an actual mobile environment, it is very difficult to appropriately place the calibration transmitter because of unpredictable multipath effects. The second type of method [4,5] injects an equal phase signal to all of the channels of the antenna array. While this does address the cabling mismatch issues, it does not address mutual coupling effects, antenna differences, tower effects, or uncertain sensor locations.

This paper motivates a procedure that is used to calibrate a smart antenna testbed and demonstrates the effectiveness of this method in field measurements. This procedure is an extension of the types of methods presented in [4,5] with additional consideration added for mutual coupling compensation and involves network analyzer measurements and computational electromagnetic (CEM) simulations. Further development of this method could also be used to consider antenna differences and tower effects, depending on the complexity of array model used.

The paper is organized as follows. Section II contains the mathematical model for antenna array output with and without calibration. Section III describes the method used to solve for the model parameters given in Section II. Section IV contains a description of the environment in which field measurements were taken. Section V contains experimental results illustrating the performance of the described calibration method and Section VI concludes the paper.

II. ARRAY MODEL

We first develop the theoretical M-antenna array model and describe how non-ideal effects can be modeled. The antenna array elements are theoretically located at (x_i, y_i), $1 \le i \le M$. A steering vector characterizes the relative phase response of each antenna array element to an incident signal with DOA

0-7803-5893-7/00/$10.00 © 2000 IEEE

θ from a single mobile user. Equation (1) represents the basic form of an ideal steering vector.

$$\vec{a}_U(\theta) = \begin{bmatrix} \exp(-jk(x_1\cos\theta + y_1\sin\theta)) \\ \exp(-jk(x_2\cos\theta + y_2\sin\theta)) \\ \exp(-jk(x_3\cos\theta + y_3\sin\theta)) \\ \bullet\bullet\bullet \\ \exp(-jk(x_M\cos\theta + y_M\sin\theta)) \end{bmatrix} \quad (1)$$

In the above equation, k is the wavenumber of the incident electromagnetic radiation that can be expressed as $2\pi/\lambda$. Note the implicit assumptions of this model do not take into account any of the non-ideal array effects given in Section I. Specifically, the equal gain of each of the channels shows that amplitude and phase mismatch between channels is not considered. Also, the model of the steering vector in Equation (1) does not include any terms indicating the retransmission of signal components from one array element to another (i.e. mutual coupling). Finally, the model assumes that the element locations (x_i, y_i) are known exactly. If the actual antenna element locations are perturbed by a significant electrical length, the steering vector can be adversely affected.

A distortion matrix, $C(\theta)$, is generally used to encapsulate all of these non-ideal effects. In the literature, this matrix is estimated from collected measurement data [3,6] and is applied to the equation of the ideal steering vector form of (1) to develop a "compensated" steering vector.

$$\vec{a}_C(\theta) = C(\theta)\vec{a}_U(\theta) \quad (2)$$

The distortion matrix is generally considered to be independent of angle. Thus, methods using this compensation technique do not correct for tower effects and generally assume the array elements to be very similar, if not identical.

Methods using a distortion matrix generally consider separately the issue of amplitude and phase mismatch between array element cabling. To take this into account, we apply the M-vector $\vec{g}$ that contains the complex values required to compensate for this mismatch and solve for the "real" steering vector $\vec{a}_R(\theta)$ (where the subscript "i" indicates the i^{th} vector component) which can be used in DOA analysis:

$$a_{R,i}(\theta) = g_i a_{C,i}(\theta) \quad (3)$$

In Section III, we describe the procedures used to solve for $\vec{g}$ and $\vec{a}_C(\theta)$ and thus determine an estimate for the actual array steering vector.

III. CALIBRATION PROCESS

A. Cable Measurements

Figure 1 shows a diagram illustrating how the vector $\vec{g}$ is determined. There are two sets of relative amplitude and phase information that make up this determination. The first set corresponds to the long cabling leading to the antenna array itself on the cellular tower (referred to as "array" cables in Figure 1). The second set corresponds to the combined effect of the cables used to connect the basestation to the array cables (referred to as "basestation" cables in Figure 1) and the varying impedance seen looking into the ports of the basestation hardware.

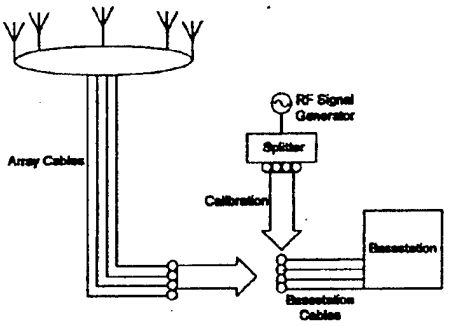

Figure 1 – Overview of Cable Calibration Process

It is relatively straightforward to determine the relative amplitude and phase response of the array cables using a network analyzer. We refer to this vector as $\vec{l}$ and it only needs to be determined once for each set of array cables. This vector contains the relative amplitude and phase response of each of the cables with respect to a given reference cable (that has a $1\angle 0°$ as its corresponding entry in the $\vec{l}$ vector).

It is slightly more difficult to determine the relative amplitude and phase response of the basestation cables and RF impedance looking into the basestation (referred to as the $\vec{s}$ vector) since this measurement must be made every time the basestation is powered up. Again, this measurement is made with respect to a reference channel. Using a power splitter with a known relative amplitude and phase response, $\vec{p}$, (determined via network analyzer) an RF signal

from a signal generator is injected into the basestation cables. The resulting data returned by the basestation normalized by the reference channel value are the elements of the $\vec{s}$ vector. $\vec{g}$ is then determined by:

$$g_i = \frac{l_i s_i}{p_i} \qquad (4)$$

The right hand side of Equation (4) contains the relative amplitude and phase mismatch of the array cables and basestation cables/hardware. The effect of the power splitter must be removed since the splitter was included in the measurement of the $\vec{s}$ vector but is absent from normal system operation.

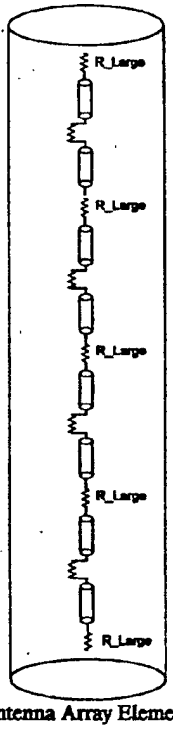

Figure 2 – Antenna Array Element Model

B. CEM Simulations

There are two different ways to solve for $\vec{a}_C(\theta)$. The first is to estimate the C matrix algorithmically in Equation (2) as is done in [3] and then use this estimate to determine $\vec{a}_C(\theta)$. An alternative method [7] uses CEM simulations [8] to determine $\vec{a}_C(\theta)$ directly. The CEM package used in this study is NEC (Numerical Electromagnetics Code), which was originally developed at the Lawrence Livermore Laboratory [9] to perform moment method analysis to model the interaction between electromagnetic fields and wire segments. A wire segment model of an arbitrary geometry antenna array can be specified in an input file to NEC. Figure 2 shows the model of a single antenna array element used in simulations. An array of these elements are placed according to array geometry, and incident signals are launched, one at a time, from all directions. The array output vector for each of these incident signals is $\vec{a}_C(\theta)$.

IV. EXPERIMENT SETUP

The array considered in this study is a uniform circular antenna array (UCA) operating at 1.8 GHz. Field measurements were made at the Pickle Research Campus at the University of Texas at Austin. To reduce multipath signal components, measurements were made in a field with buildings far off in the distance. An RF signal generator attached to a dipole antenna was used to represent a mobile user. Measurements were made with this mobile user at several different locations relative to the basestation. DOA analysis of the received data is made with the Multiple Signal Classification (MUSIC) algorithm [10].

V. RESULTS

A. Pre-Calibration Spatial Spectrum

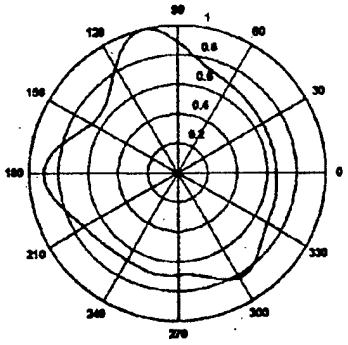

Figure 3 – MUSIC Spatial Spectrum – No Calibration

Figure 3 shows the MUSIC spatial spectrum due to a mobile user located at 80° relative to the basestation. As seen by the above plot, the lobes in the normalized spatial spectrum do not correspond at all to the signal of the desired mobile user. In fact, the lobes

in this spatial spectrum do not correspond to any known signal or multipath component, which is not surprising due to the lack of any kind of array calibration.

B. Amplitude and Phase Mismatch Compensation

Figure 4 shows the MUSIC spatial spectrum of Figure 3, with compensation added for array cables and basestation cables/hardware, as discussed in Section III.A. As this figure shows, the mobile user at 80° can now be resolved easily. However, again there is a lobe at 280° that does not correspond to any known signal component or multipath.

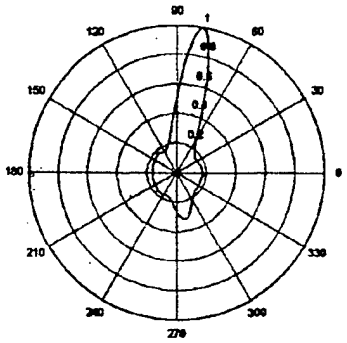

Figure 4 – MUSIC Spatial Spectrum – Cable Calibration

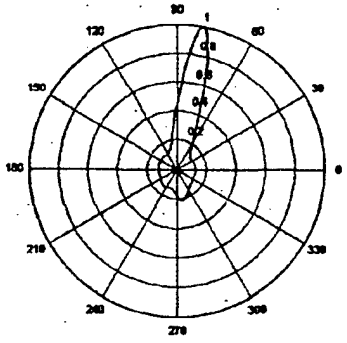

Figure 5 – MUSIC Spatial Spectrum – Full Array Calibration Applied

C. Mutual Coupling Compensation

Figure 5 displays the result of adding the mutual coupling compensation discussed in Section III.B. to the spectrum shown in Figure 4. Specifically, the results in this figure includes calibration for amplitude and phase mismatch due to array cables and basestation cables/hardware, as well as calibration including mutual coupling effects. While there is still an extraneous lobe in this Figure, it is not as large as the lobes in Figures 3 or 4, which could easily be counted as multipath signal components from different DOAs. In addition, comparison of Figure 4 and 5 shows a narrower peak in Figure 5 that corresponds to the DOA of the desired mobile user. This general result was observed in all tested cases.

VI. CONCLUSIONS

The results of this paper quantify the effects of a multi-step smart antenna calibration process. As shown by noting the relative improvement from Figures 3 and 4 and the improvement from Figures 4 and 5, it is clear that amplitude and phase mismatch effects in array cables and basestation cables/hardware are much more significant than mutual coupling effects. This is not to imply that mutual coupling calibration is not necessary since Figure 5 clearly shows that lobes that could have been mistaken for multipath signal energy were effectively reduced. In addition, mutual coupling calibration makes the peak in the spatial spectrum corresponding to the desired mobile user narrower.

The procedure presented in this paper is important because it does not require expensive and involved site-specific calibration. The network analyzer measurements can all be made relatively easily and the CEM simulations can be performed off-line using the free and well-accepted package NEC. The combination of these two steps allow for very effective array calibration.

ACKNOWLEDGEMENTS

This work is supported by the Texas Higher Education Coordinating Board under the Texas Advanced Technology Program and by the Office of Naval Research under contract no. N00014-98-1-0178.

REFERENCES

[1] Y. Chen, A. Chang, and H. Lee, "Array Calibration Methods for Sensor Position and Pointing Errors," *Microwave and Optical Technology Letters*, vol. 26, pp. 132-137, 2000.

[2] B. Kang, H. Subbaram, and B. Steinberg, "Improved Adaptive-Beamforming Target for Self-Calibrating a Distorted Phased Array," *IEEE Transactions on Antennas and Propagation*, vol. 38, pp. 186-194, 1990.

[3] C. See, "Sensor array calibration in the presence of mutual coupling and unknown sensor gains and phases," *Electronics Letters*, vol. 30, pp. 373-374, 1994.

[4] R. Ertel, Z. Hu, and J. Reed, "Antenna Array Hardware Amplitude and Phase Compensation Using Baseband Antenna Array Outputs," *1999 IEEE Vehicular Technology Conference Proceedings*, vol. 3, pp. 1759-1763, 1999.

[5] G. Tsoulos and M. Beach, "Calibration and Linearity issues for an Adaptive Antenna System," *1997 IEEE Vehicular Technology Conference Proceedings*, vol. 3, pp. 1597-1600, 1997.

[6] A. Lemma, E. Deprettere, and A. van der Veen, "Experimental Analysis of Antenna Coupling for High-Resolution DOA Estimation Algorithms," *1999 IEEE 2nd Workshop on Signal Processing Advances in Wireless Communications*, pp. 362-365, 1999.

[7] T. Su, K. Dandekar, and H. Ling, "Simulation of Mutual Coupling Effect in Circular Arrays for Direction Finding Applications," *Microwave and Optical Technology Letters*, vol. 26, pp. 331-336, 2000.

[8] K. Pasala and E. Friel, "Mutual Coupling Effects and Their Reduction in Wideband Direction of Arrival Estimation," *IEEE Transactions on Aerospace and Electronic Systems*, vol. 30, pp. 1116-1122.

[9] NEC-2 Manual, Lawrence Livermore National Laboratory, 1996.

[10] H. Krim and M. Viberg, "Two Decades of Array Signal Processing Research: The Parametric Approach," *IEEE Signal Processing Magazine*, pp. 67-94, 1996.

Design of Dual-Band Microstrip Antennas Using the Genetic Algorithm

H. Choo, and H. Ling
Department of Electrical and Computer Engineering
The University of Texas at Austin
Austin, TX 78712-1024 U.S.A
E-mail: hschoo@ece.utexas.edu

Abstract:

We report on the use of the genetic algorithm (GA) to design patch shapes of microstrip antennas for dual-band applications. We employ a full-wave electromagnetic solver to predict the performance of microstrip antennas with arbitrary patch shapes. Two-dimensional chromosome is used to encode each patch shape into a binary map. GA with two-point crossover and geometrical filtering is implemented to achieve efficient optimization. The GA-optimized designs are built on FR-4 substrate and measurement results show good agreement with the numerical prediction. The optimized patch design achieves good impedance match at both frequencies. The patch shape is further optimized to broaden the bandwidth at one of the frequencies. It is also shown that a frequency ratio between the two frequency bands ranging from 1.2 to 2 can be achieved using the GA design method.

Introduction:

With the growing demand of wireless applications, microstrip antennas that can operate in two or more frequency bands are in demand. Various dual-band methods for microstrip antennas have been proposed to date. For example, multi-layered structures, parasitic patches and shorting posts are some of the well-known techniques for achieving dual-band operation [1]. In this paper, we examine the use of genetic algorithms (GA) to design optimal shapes for microstrip antennas to achieve dual-band operation. The attractiveness of GA shape optimization is that dual-band performance can be achieved with little increase in overall volume or manufacturing cost.

The design of dual-band microstrip antennas using GA was first addressed by Johnson and Rahmat-Samii [2]. Air substrate was used in their study. In this work, we focus on FR-4 as the substrate material, since it is the most commonly used material in wireless devices. In our GA implementation, a two-point crossover scheme involving three chromosomes is used. Furthermore, geometrical filtering is applied to each chromosome to obtain a more realizable shape. The GA-optimized shapes for dual-band operation are presented. It is also shown that arbitrary frequency ratios between the two frequency bands ranging from 1.2 to 2 can be achieved through the GA design.

GA Optimization:

GA is implemented to optimize the microstrip patch shape in order to achieve dual-band operation. In our GA, we use a two-dimensional (2-D) chromosome to encode each patch shape into a binary map [3]. The metallic sub-patches are represented by ones and the no-metal areas are represented by zeros. Since it is more desirable to obtain optimized patch shapes that are well connected from the manufacturing point of view, a 2-D median filter is applied to the chromosomes to create a more realizable population at each generation of the GA.

To evaluate the performance of each patch shape, we use a full-wave periodic patch code adapted from a frequency selective surface code [4]. The formulation of the code is similar to that described in [5]. The electromagnetic analysis is carried out by using the electric-field integral equation (EFIE). The periodic Green's function for layered medium is the kernel of the integral equation. Rooftop basis functions are used to expand the unknown current on the metal patch and fast Fourier transform (FFT) is used to accelerate the computation of the matrix elements. To reduce the matrix fill-time, matrix element calculation is done only once and stored before the GA process. Because of the assumed periodicity in this patch code, we use a period that is greater than one wavelength to avoid coupling between the adjacent patches for single patch simulation.

The design goal is to produce good antenna radiation at two frequency bands by changing the patch shape. The low frequency is chosen at 1.9 GHz and the higher one is chosen at 2.85 GHz. To achieve dual-band design, an additive cost function is defined as

$$\text{Cost} = \frac{1}{N}\sum_{n=1}^{N} Pn \quad where \quad Pn = \begin{cases} S_{11}(dB) + 10\,dB & if\ S_{11}(dB) \geq -10\,dB \\ 0 & if\ S_{11}(dB) < -10\,dB \end{cases} \tag{1}$$

$$+ \quad \frac{1}{N}\sum_{n=1}^{N} \frac{1}{\sigma}\int_{s} |J|^2\, ds$$

The first part of the cost function accounts for the impedance mismatch and is defined as the average of those return loss (S_{11}) values that exceeds –10dB (i.e., VSWR=2:1) within the two frequency bands of interest. The second part of the cost function accounts for the total metal loss (dB) generated by the current flowing on the patch. The conductivity of aluminum (σ = 3.82e7 S/m) is used, as the microstrip in our measurements were built using aluminum tape.

Based on the cost function, the next generation is created by a reproduction process that involves crossover, mutation and 2-D median filtering. A two-point crossover scheme involving three chromosomes is used. The process selects three chromosomes as parents and divides each chromosome into three parts. Intermingling the three parent chromosomes then makes three child chromosomes. It is found that the two-point scheme exhibits a faster convergence behavior than the

one-point scheme. The GA process is iterated until the cost function converges to a minimum value.

Results:

Fig. 1(a) shows the GA-optimized microstrip shape for dual-band operation. A 72mm × 72mm square design area in which the metallic patch can reside is discretized into a 32 × 32 grid for the chromosome definition. The thickness of the FR-4 substrate (dielectric constant of 4.3) is 1.6 mm. In the GA-optimized shape, the dark pixels are metal and the white pixels have no metal. The white dot shows the position of the probe feed. Fig. 1(b) shows the predicted return loss (S_{11} in dB) of the resulting microstrip antenna. Good matches are exhibited by the return loss curve at the design frequencies of 1.9 GHz and 2.85 GHz. The bandwidths at the two design frequencies are about 4% and 1.4%, respectively.

Previously, we have used GA to achieve broadband operation for a single-band microstrip [6]. The resulting bandwidth on 1.6 mm FR-4 substrate is about 8%. Here, we try to increase the bandwidth of the dual-band microstrip antenna from the above design. The low frequency (1.9 GHz) is chosen to be our target for broadbanding, while the bandwidth of high frequency is kept the same. During the GA iterations, we gradually increase the frequency range centered at 1.9 GHz in our cost function definition until the broadband design is achieved. Fig. 2(a) shows a bandwidth-enhanced dual-band result. To experimentally verify the GA design, we have built and measured such a microstrip patch. Fig. 2(b) shows the measurement and simulation return loss for the shape in Fig. 2(a). Good agreement is observed between the measurement and simulation results (the square dots show the predicted values). Figs. 2(c) and (d) show the measured boresight radiations (S21 dB) for the two diagonally oriented polarizations. Also plotted in the insets are the predicted current distributions at three frequencies of interest. We note that near 1.9 GHz, there are two modes with orthogonal current directions at two closely spaced frequencies, leading to the broadening of the impedance bandwidth in Fig. 2(b). At 2.9 GHz, only a single mode exists.

In the above examples, the ratio between the two frequency bands is chosen to be 1:1.5. We next carry out the dual-band design steps using GA to achieve different frequency ratios between the low and the high frequency band. During the design, we keep the low frequency band fixed around 1.9 GHz, while varying the design frequency for the high band. Frequency ratios from 1:1.2 to 1:2 are attempted using GA. Figs. 3(a), (b) and (c) show the optimized shapes and the corresponding return loss versus frequency curves for the frequency ratios 1:1.2, 1:1.4 and 1:1.74, respectively. We find that it is possible to use the GA approach to cover the entire dual-band frequency ratio from 1:1.2 to 1:2.

Conclusions:

Optimized patch shapes for dual-band microstrip antennas on thin FR-4 substrate have been investigated using the genetic algorithm. The resulting microstrip designs show good operation

characteristics for dual frequencies. The bandwidth of the microstrip can be further broadened by optimization. This result has been verified by laboratory measurement. Finally, it has been shown that the frequency ratio between the two bands ranging from 1:1.2 to 1:2 can be achieved using the same GA methodology.

Acknowledgments:

This work is supported by the Office of Naval Research under Contract No. N00014-98-1-0178, the Air Force MURI Center for Computational Electromagnetics under Contract No. AFOSR F49620-96-1-0025, and the Texas Higher Education Coordinating Board under the Texas Advanced Technology Program.

References

[1] J. R. James, P. S. Hall, Handbook of Microstrip Antennas, vol. 1. London: Peter Peregrinus, 1989.

[2] J. M. Johnson and Y. Rahmat-Samii, "Genetic Algorithms and Method of Moments(GA/MOM) for the Design of Integrated Antennas," *IEEE Trans. Antennas Propagat.*, vol. 47, pp. 1606-1614, Oct. 1999.

[3] M. Villegas and O. Picon, "Creation of New Shapes for Resonant Microstrip Structures by Means of Genetic Algorithms," *Elec. Lett.*, vol. 33, pp. 1509-1510, Aug. 1997.

[4] L. C. Trintinalia, "Electromagnetic Scattering from Frequency Selective Surfaces," M.S. Thesis, Escola Politécnica da Univ. de São Paulo, Brazil, 1992.

[5] T. Cwik and R. Mittra, "Scattering from a Periodic Array of Free-Standing Arbitrarily Shaped Perfectly Conducting or Resistive Patches," *IEEE Trans. Antennas Propagat.*, vol. 35, pp.1226-1234, Nov. 1987.

[6] H. Choo, A. Hutani, L. C. Trintinalia and H. Ling, "Shape Optimization of Broadband Microstrip Antennas Using the Genetic Algorithm," accepted for publication in *Elect. Lett.*, Nov. 2000.

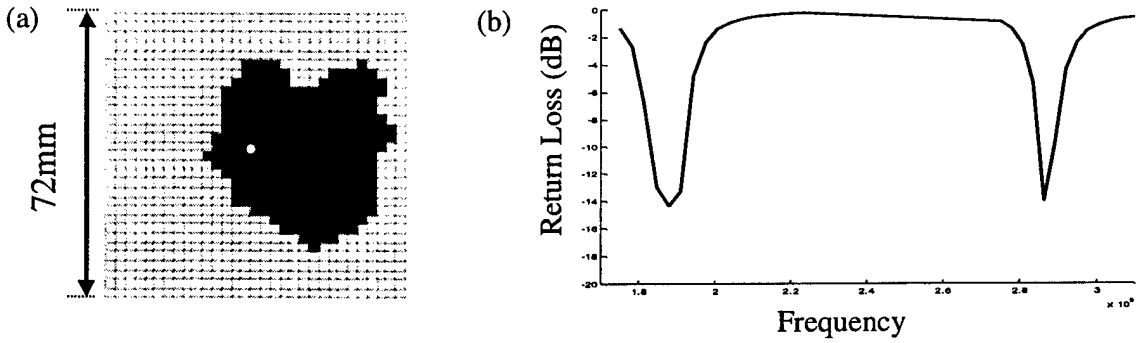

Fig. 1. GA optimized dual-band microstrip antenna (frequency ratio 1:1.5).

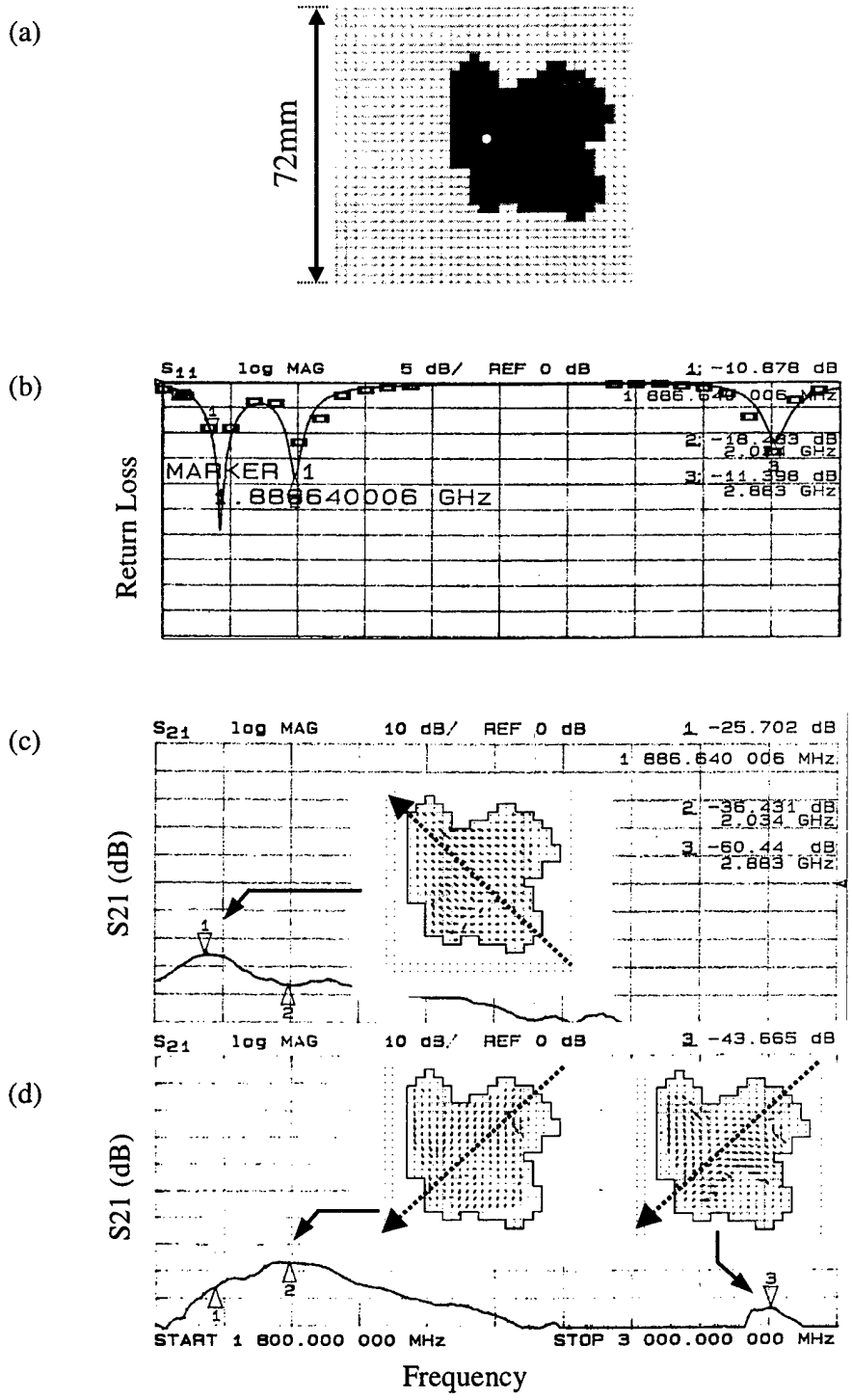

Fig. 2. Dual-band microstrip antenna design with enhanced bandwidth at the low band.

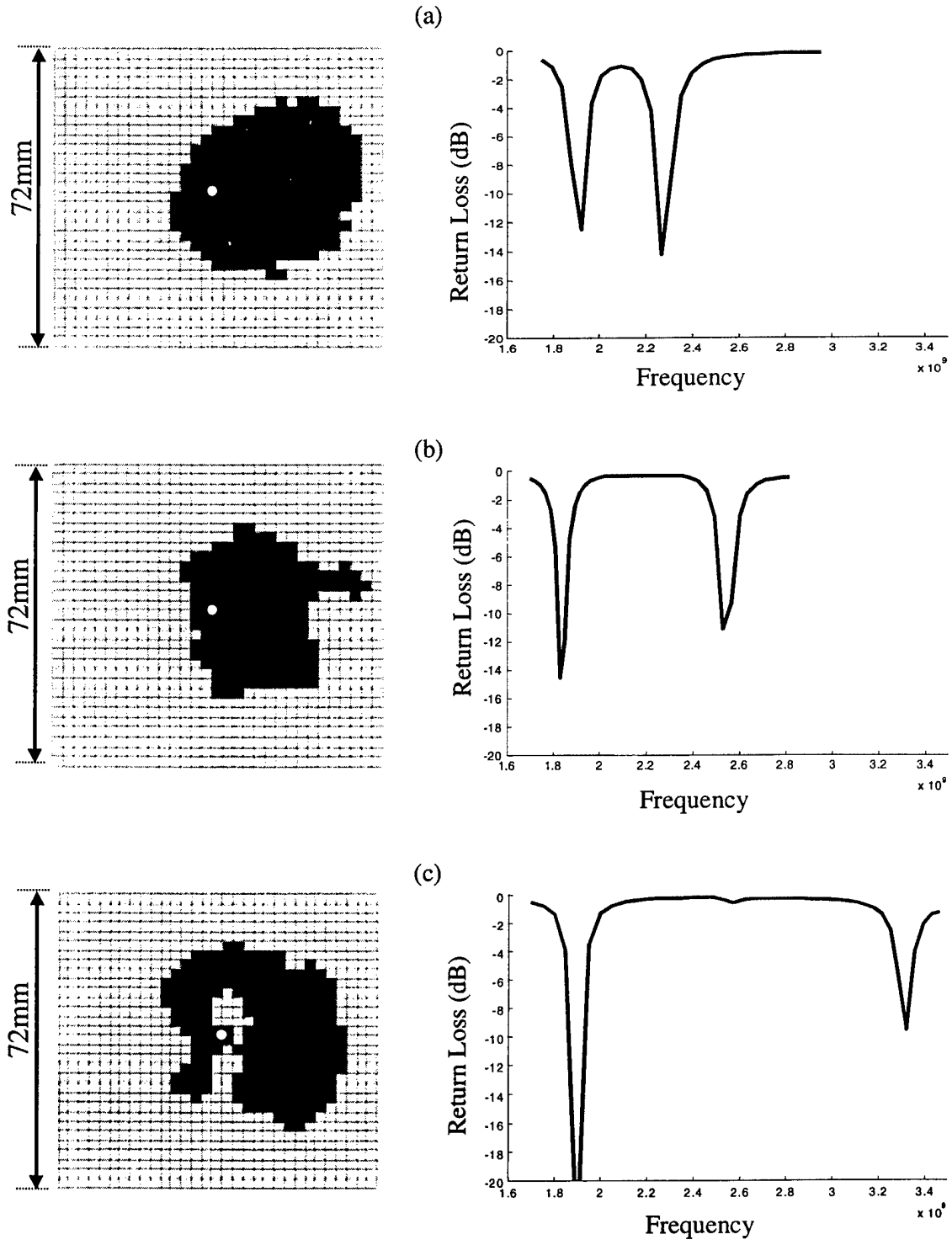

Fig. 3. GA-designs for dual-band frequency ratios of (a) 1:1.2 (b) 1:1.4 and (c) 1:1.74.

Design of Corrugated Absorbers for Oblique Incidence Using Genetic Algorithm

Hosung Choo* and Hao Ling
Department of Electrical Engineering
University of Texas at Austin
Austin, TX 78712 U.S.A

Charles S. Liang
Lockheed Martin Aeronautics Company
P.O. Box 748
Fort Worth, TX 76101 U.S.A

Introduction

Genetic algorithm (GA) has been applied to the design of multi-layered planar and cylindrical absorber structures [1]. Corrugated coatings with non-planar shape profile offer an additional degree of design freedom and have been analyzed in [2]. In this paper, we apply GA to design the optimal shape for a corrugated coating under oblique incidence (see Fig. 1). To predict the performance of each shape, we employ a full-wave electromagnetic solver. GA with two-point crossover and geometrical filtering is implemented to achieve effective optimization. The optimized designs for different polarizations are presented.

GA Optimization

GA is implemented to optimize the shape of a corrugated absorber under oblique incidence. The absorber consists of a single layer of lossy material. It has one-dimensional periodicity along the x-dimension and is invariant along the z-dimension (Fig. 1). The incidence wave direction is defined by θ_{el} and $\phi_{grating}$. The elevation angle θ_{el} is measured from grazing while $\phi_{grating}$ is the azimuth angle measured from the z-axis. To encode each possible absorber shape into a chromosome, the height of the coating at each point along the x-direction is represent as a binary string. To achieve more realizable shape, we apply a sliding window filter that operates like a low-pass spatial filter during each generation of the GA. In addition, we enforce symmetry constraint on the shape.

To evaluate the performance of each absorber shape, we use a full-wave electromagnetic simulation code based on the boundary-integral formulation [2]. The design goal is to choose the coating profile that gives rise to the best absorbing characteristics over the frequency band of interest. The design frequency band is chosen to be from 8 GHz to 18 GHz, and the maximum height of the grating is restricted to 8mm. Associated with this design goal, we define the cost function as:

0-7803-7070-8/01/$10.00 ©2001 IEEE

$$Cost = \frac{1}{N}\sum_{n=1}^{N} Pn \quad where \quad Pn = \begin{cases} \Gamma(dB) + 20dB & if\ \Gamma(dB) \geq -20dB \\ 0 & if\ \Gamma(dB) < -20dB \end{cases} \quad (1)$$

Based on the cost function, the next generation is created by a reproduction process that involves crossover, mutation and sliding window filtering. A two-point crossover scheme involving three chromosomes is used. The process selects three chromosomes as parents and divides each chromosome into three parts. Intermingling the three parent chromosomes then makes three child chromosomes. The reproduction process is iterated until the cost function converges to a minimum value.

Results

Standard magram is used for the coating material. We consider the case when the incident angles are set to θ_{inc}=30° and $\phi_{grating}$=0°. The bottom of the coating is backed by a conducting ground plane. The period of the profile is set to 2.032mm and is discretized into 32 points. The height of the groove at each point is described by a 6-bit number that ranges between 0 and 8mm (in 64 steps). First, we consider the case when only the VV reflection coefficient is used in the cost function definition. Fig. 2(a) shows the resulting GA-optimized shape, which closely resembles the triangular shape. Fig. 2(b) is plot of the simulated reflection coefficients (in dB) versus frequency for the optimized shape. We see that the reflection coefficient of the VV polarization nearly meets the -20 dB design goal over the entire frequency band from 8GHz to 18GHz. The HH polarization is not optimized and shows a much higher reflection coefficient. Next, we consider the reverse situation when only the HH reflection coefficient is used in the cost function. Fig. 3(a) shows the resulting GA-optimized shape. It is noted that the optimal shape of corrugation resembles a rectangular profile. Fig. 3(b) shows the simulated reflection coefficients (in dB) versus frequency for the optimized shape for both the VV and the HH polarization. The reflection coefficient of the HH polarization is less than -15 dB for nearly the entire frequency band of interest. In the third example, we optimize the shape by using the average of the reflection coefficients from the HH and VV polarizations in the cost function. The resulting shape is shown in Fig. 4(a). As we have seen from the last two examples, the design for the HH polarization is harder than that for the VV polarization. Therefore in this case, the cost is dominated by the HH consideration, and the resulting GA-optimized shape is not that different from the optimized shape for the HH-polarization shown in Fig. 3(a). As a final example, we impose an additional constraint such that the complementary air region has the same shape as the absorber. Presumably, this means we can make two usable pieces of absorber by cutting them from a single thick piece. The optimized shape and the reflection coefficient are presented in Figs. 5(a) and 5(b), respectively.

Conclusion

GA-optimized shapes for a corrugated absorber under oblique incidence have been presented for different incident polarizations. The designed absorber shape for the VV polarization closely resembles a triangular profile, while that for the HH polarization

resembles a rectangular profile. An optimized absorber profile with an additional complementary constraint to achieve a more efficient material usage is also reported.

Acknowledgments

This work is supported in part by the Office of Naval Research under Contract No. N00014-01-1-0234 and the Air Force MURI Center for Computational Electromagnetics under Contract No. AFOSR F49620-96-1-0025.

References

[1] E. Michielssen, J. M. Sajer, S. Ranjithan and R. Mittra, "Design of lightweight, broad-band microwave absorbers using genetic algorithm," *IEEE Trans. Microwave Theory Tech.*, vol. 41, pp. 1024-1031, June-July 1993.

[2] J. Moore, H. Ling and C.S. Liang, "The scattering and absorption characteristics of material-coated periodic grating under oblique incidence," *IEEE Trans. Antennas Propagat.*, vol. 41, pp. 1281-1288, Sept. 1993.

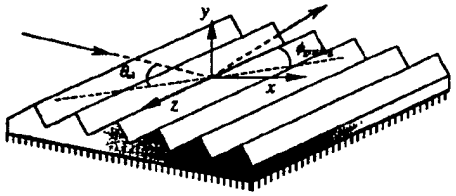

Fig. 1 Geometry of the corrugated absorber.

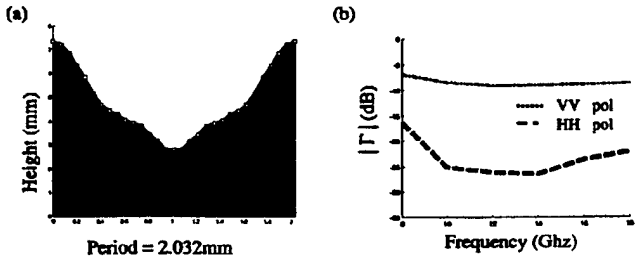

Fig. 2 (a) GA optimized shape for the VV pol. (b) Reflection coefficient (dB) versus frequency

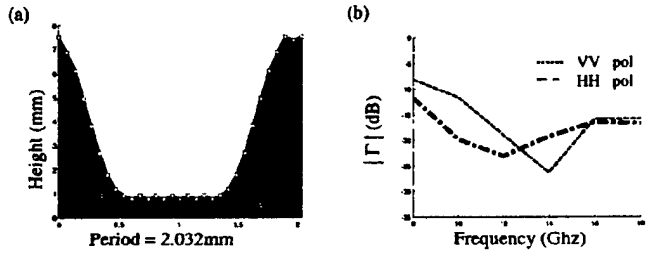

Fig. 3 (a) GA optimized shape for the HH pol. (b) Reflection coefficient (dB) versus frequency

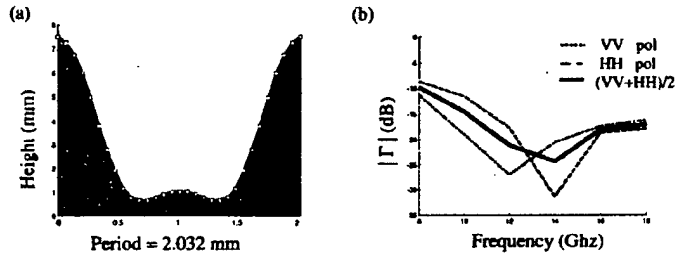

Fig. 4 (a) GA optimized shape for the average of VV and HH pol. (b) Reflection coefficient (dB) versus frequency

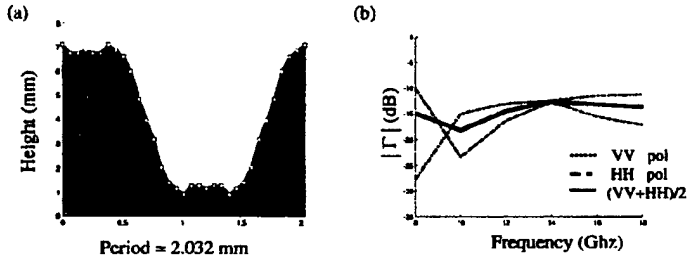

Fig. 5 (a) GA optimized shape with the complementary constraint. (b) Reflection coefficient (dB) versus frequency

The use of the genetic algorithm approach in the design of ultra-wideband antennas

Aaron Kerkhoff *, Robert Rogers *, Hao Ling **
* Applied Research Laboratories, University of Texas - Austin
telephone: (512) 835-3173; fax: (512) 835-3212; e-mail: kerkhoff@arlut.utexas.edu
telephone: (512) 835-3307; fax: (512) 835-3212; e-mail: rogers_b@arlut.utexas.edu
** Department of Electrical and Computer Engineering, University of Texas - Austin
telephone: (512) 471-1710; fax: (512) 471-1856; e-mail: ling@ece.utexas.edu

Abstract - The application of Genetic Algorithm (GA) optimization to the design of ultra -wideband antennas for use in multi-service wireless devices is described. The antennas explored in this study are monopoles with planar, fully - metal radiating elements. The key design constraints and criteria to be considered in the development of such antennas are discussed. Presented and discussed are results from an application of a GA optimizer to the design of bow - tie and reverse bow-tie monopole antennas.

I. INTRODUCTION

The trend in the wireless industry is towards enabling mobile end-terminal devices to achieve multi-service performance. To date this has included access to both analog and digital cellular bands between 0.8 - 0.9 GHz and 1.8 - 1.9 GHz. It will be necessary, however, to operate simultaneously at other bands such as 1.8 to 2.2 GHz for 3G services and 2.4 GHz to allow access to WLAN and technologies such as Bluetooth. Positioning information is also desirable requiring access to the GPS bands at 1.227 GHz and 1.575 GHz. These devices in the future may also implement some form of the emerging Impulse Ultra-Wideband (IUWB) radio for supplemental, short range communications and high-resolution ranging or positioning [1]. IUWB offers distinct advantages for reduced power consumption, design complexity, and size. This technology, which uses an impulse-based carrier, requires an ultra-wide instantaneous bandwidth on the order of 60% to 100%.

Clearly it desirable to design the smallest possible end-terminal to access all of these services simultaneously. The antenna imposes a limitation on the miniaturization that is achievable in such a device. Ideally, a single, physically small antenna is desired that can operate over all of the frequency bands listed above. This requires that the antenna function at each of the bands between 0.8 and 2.4 GHz as well as over the entire band associated with IUWB. Good impedance matching and high radiation efficiency must be achieved over this entire bandwidth in order to guarantee satisfactory signal reception and maintain low power operation. IUWB service also requires a linear phase response for efficient operation. These requirements impose severe restrictions on the types of antennas that may used for such a multi-service wireless device, especially when small size is of key concern.

There have been a wide variety of antennas proposed for multi-service wireless applications. For instance, a Planar Inverted F Antenna (PIFA) patch-type design capable of covering the 0.9, 1.8, and 2.4 GHz bands has been proposed [2]. While patch designs offer small and / or conformal solutions, they are all inherently band-limited. Monopole designs using frequency independent elements offer a number of wide operating bands [3]. Other frequency independent designs such as spirals offer "flat" instantaneous matching bandwidths as wide as 5:1 [4]. Frequency independent antennas, however, are inherently dispersive, which does not satisfy the phase linearity requirement of IUWB. Recent studies indicate that planar, fully-metal monopoles (PFMM) may offer very wide instantaneous bandwidths (as much as 12:1) with a relatively small size. As their operating principle is much like that of the traditional wire monopole, these elements should also demonstrate good phase linearity.

The most common PFMM antenna is the bow-tie (BT) which has long been known to possess broadband performance. The BT antenna is the planar form of the conical antenna for which a closed-form analysis is possible. Its performance can therefore be understood in terms of that of the cone. Also the performance of finite-sized BT antennas, both in terms of input impedance and radiation patterns, has been characterized experimentally in the literature [5]. From this data, it can be determined that there are two key parameters in the design of BT antennas, the element height, and the element flare angle. The height essentially determines the operating mode and the lower frequency limit of the antenna, while the flare angle controls the variation of the input impedance over frequency, the high frequency

0-7803-7189-5/01/$10.00 ©2001 IEEE

impedance value, as well as the resonance bandwidth. From this analysis, it can be seen that the design of BT antennas is rather straightforward. For this reason, BT antennas have been used successfully in many practical broad-band radio systems.

Other PFMM element shapes such as squares and circles have proposed for broadband operation [6]. These designs differ from the BT in that they must be raised above the ground plane by a fixed height in order to avoid shorting to it. Their performance has yet to be fully explored due to the lack of an analytical model, and the only recent emergence of experimental data. For these reasons, there exists no clear design methodology for such element shapes, and no means by which to optimize their performance.

Therefore, a study was proposed to evaluate these new shapes using the Genetic Algorithm (GA) approach. The GA was chosen due to its ability to optimize problems involving multiple design parameters as well as complex, and conflicting design criteria, and to converge to a nearly global solution in doing so. There has also been much success in recent years in applying the GA to antenna design [7]. In this study, the GA is used to determine the optimal dimensions of the selected element shape in order to fulfill the given bandwidth requirement. By repeating this procedure for increasing bandwidth requirements, it was hoped that a design methodology for the element would emerge and the absolute limits of its broadband performance could be determined.

II. APPROACH

The element chosen for initial study was the reverse bow-tie (RBT). This shape was chosen due to its similarity to the traditional BT, which would allow a direct comparison of the performance of identically sized elements. Figure 1 compares the two configurations. As can be seen, the element height, H, and flare angle, α, are design parameters for both elements, while the RBT has the additional parameter of feed height, h_f.

A GA optimization algorithm was written that operates on encoded combinations of these design parameters. Using a numerical electromagnetic simulation code, the response of individual antenna designs represented by these parameter combinations is determined. From this data, a cost function is defined which assesses the relative goodness of each design according to some pre-determined criteria. New designs are generated by mixing parameter information between different designs through the crossover operator, and randomly changing parameter information through the mutation operator. The performance is again evaluated for these new designs. This process is repeated until the original design goal is met.

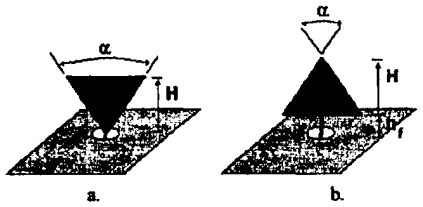

FIGURE 1. Monopole antenna elements under study.
a. bowtie
b. reverse bowtie

This same algorithm was applied to both the BT and RBT. To maintain consistency, the design parameters used for both designs were height, flare angle, and feed height even though the bow-tie ideally is not raised above the ground plane.

The Numerical Electromagnetics Code (NEC-2) was implemented as the electromagnetic simulator in the GA. The planar structures under study were therefore modeled using wire elements. Figure 2 shows an example of the model developed for the BT antenna. This model essentially consists of a best - fit square mesh to which additional segments are added along the outside to exactly fit the shape of the antenna. This was necessary in order to achieve the desired simulation accuracy,

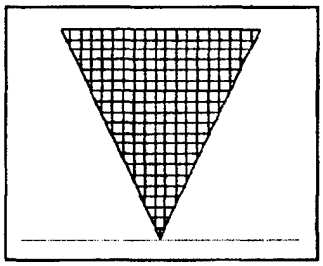

FIGURE 2. Wire mesh used to model the bow-tie.

especially near the feed. The antenna was modeled over an infinite ground plane and the excitation was applied across a segment of length h_f placed between the bottom of the antenna and the ground plane. A similar model was developed for the RBT by simply inverting the BT model. The convergence of these models was verified and a mesh density was chosen that was a compromise between accuracy and complexity (run-time).

For this study, only the input impedance matching of the antenna was optimized by the GA. NEC was used to calculate the input impedance at individual frequencies in the band under optimization. These results were used by the GA to calculate the corresponding VSWR values at each frequency. A cost was then assigned to each design by finding the maximum VSWR value in the frequency range. The GA sought to minimize this value. The GA ran until the condition MAX ($VSWR_i$) ≤ 2 was met or it was determined that the GA could not converge to a solution.

A steady-state GA with binary tournament selection was developed. A replacement rate of 50% and mutation rates between 2 - 4 % were used throughout. The population size used was 60.

III. RESULTS / DISCUSSION

To evaluate the broadband performance of each antenna type, the GA was run a number times with different bandwidth requirements. For each run, the bandwidth was centered about 1 GHz. For example, if a fractional bandwidth of 20% was desired, the GA would optimize from 900 MHz to 1100 MHz. It was found that a fixed mesh density of 0.75 cm could be used to accurately model antennas with widely varying heights and flare angles in this frequency range. It was also found that these antennas could be sufficiently characterized by taking 100 MHz steps between simulations. For the given example, this would imply that the GA would run NEC three times in order to evaluate a design. The overall dimensions of the antenna elements were nominally limited to 30 cm x 30 cm to keep GA run times low and because smaller antenna designs were desired. The maximum parameter values were also limited to H = 30cm, $\alpha = 120°$, $h_f = 0.8$cm. A 50Ω feed line was assumed throughout all simulations. Figures 3 and 4 give the results of GA runs with increasing fractional bandwidth requirements for the BT and RBT antennas, respectively.

For the given restrictions, the BT GA was unable to find a solution for fractional bandwidths greater than 20%, while the RBT GA found solutions for bandwidths of up to 80%. It is clear from these results that the RBT is able to achieve a significantly larger bandwidth than the BT with a dramatically smaller size. For instance, the BT design generated by the 40% bandwidth GA run requires over 5.6 times as much surface area as the RBT.

fractional bandwidth (%)	H (cm)	α (deg.)	hf (cm)	cost
20	13.33	95.3	0.461	1.90
30	14.25	91.0	0.416	2.34
40	14.25	92.2	0.439	2.60

FIGURE 3. Results of GA optimization on the bow-tie antenna.

fractional bandwidth (%)	H (cm)	α (deg.)	hf (cm)	cost
20	9.67	43.1	0.37	1.18
30	10.00	42.4	0.46	1.25
40	10.33	38.8	0.46	1.34
50	10.50	36.5	0.48	1.44
60	11.00	35.3	0.48	1.57
70	11.00	33.0	0.66	1.71
80	11.33	25.1	0.78	1.99

FIGURE 4. Results of GA optimization on the reverse bow-tie antenna.

As predicted by experimental data [5], even for lower bandwidth requirements, the BT requires a wide flare angle to match to the relatively low impedance of the 50Ω feed line. Just to achieve a 20% bandwidth requires nearly the maximum width allowed in the GA. Since no more width is available to try wider flare angles or taller heights, the BT is unable to achieve wider bandwidths.

The RBT is much more flexible in terms of the matching quality vs. bandwidth design trade-off. This is made more clear from an examination of the impedance plots, which are presented in Figure 5 for selected reverse bow-tie designs. For smaller bandwidth requirements, the GA selects wider flare angles, which leads to smaller resistance values within the optimization bandwidth. As can be seen in Figure 6 which shows the corresponding VSWR values, the antenna is very well matched at the center of the band. To achieve a wider bandwidth, the GA must select a narrower flare angle to raise the resistance. This results in a worse match at the center of the band, but a better match overall so that a wider bandwidth is achieved. It is interesting to note that the height only increases slightly for higher bandwidth requirements. This is despite the fact that the current path length has been shortened due to the narrower flare angle and the lower band-limit has been reduced. This implies that the RBT uses its full surface area efficiently to achieve broadband performance. It is also interesting to note that while the BT GA sought roughly the same feed height regardless of the bandwidth requirement, the value of this parameter for the

RBT steadily increased with increasing bandwidth. For the RBT, the feed height serves as a means by which to optimize the matching of the element to the feed line. It mostly affects the reactance of the antenna, scaling the reactance downwards (more capacitive) for shorter feed heights, and upwards (more inductive) for taller feed heights. For narrower flare angles, the smaller element width leads to a reduced inductance. Therefore the feed height must be raised in order to compensate for the reduced element inductance and achieve optimal impedance matching.

The RBT designs generated by the 30% and 70% bandwidth GAs run were both constructed out of thin sheet copper and measured over a ground plane of dimensions 48 cm x 48 cm. These results are also shown in Figure 6. The agreement between the measured and simulated response is good, especially across the optimization bandwidth.

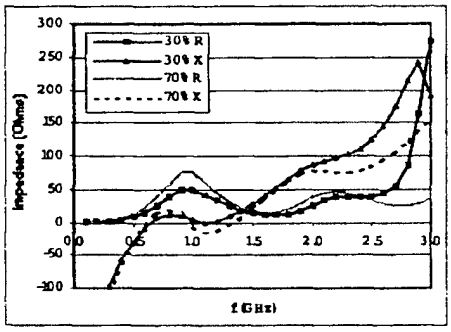

FIGURE 5. Simulated input impedance for the 30% and 70% bandwidth reverse bow-tie designs.

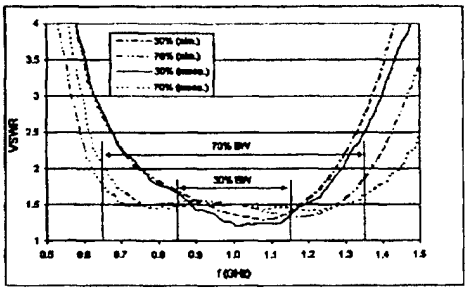

FIGURE 6. Measured vs simulated results for 30% and 70% bandwidth reverse bow-tie design.

IV. CONCLUSION

It has been demonstrated that the GA is an effective means of evaluating the broadband performance of PFMM antennas. It was shown that the RBT antenna can achieve a much wider impedance matching bandwidth than the BT with significantly reduced sizes. The results from the GA illustrate a design methodology for RBT antennas which allows a tradeoff between matching quality and bandwidth. This tradeoff can be achieved without significantly changing the overall size of the antenna. Experimental results confirmed the findings of the GA.

REFERENCES

[1] A. Petroff, P. Withington, "Time Modulated Ultra - Wideband (TM - UWB) Overview", from Time Domain Incorporated website: http://www.timedomain.com .

[2] P. Song, P.S. Hall, H. Ghafouri-Shiraz, D. Wake, "Triple-Band Planar Inverted F Antenna", *IEEE Electronics Letters*, vol. 36, pp. 112-114, January, 2000.

[3] C. Song, P. Hall, H. Ghafouri-Shiraz, D. Wake, "Multi - Circular Loop Monopole Antenna", *IEE Electronics Letters*, vol. 36, pp. 391-393, March, 2000.

[4] E. Gshwendtner, J. Parlebas, W. Wiesbeck, "Spiral Antenna with Frequency-Independent Coplanar Feed for Mobile Communication Systems", *IEEE International Symposium on Antennas and Propagation 1999*, pp. 560 -563.

[5] G.H. Brown, O.M. Woodward, "Experimentally determined radiation characteristics of conical and triangular antennas," *RCA Review*, pp. 425-452, 1952.

[6] N. Agrawall, G. Kumar, K. Ray, "Wide-Band Planar Monopole Antennas", *IEEE Trans. on Antennas and Propagation*, vol. 46, pp. 294 - 295, February, 1998.

[7] Y. Rahmat-Samii, E. Michielssen, *Electromagnetic Optimization by Genetic Algorithms*, New York: John Wiley & Sons, 1999.